Shock and Vibration Isolation Concepts through Use of Dynamic, Multi-Degree-of-Freedom Mechanical Systems

A Dissertation
Presented to
The Academic Faculty

by

Eric Christopher Smith

In Partial Fulfillment
of the Requirements for the Degree
Doctor of Philosophy in the
George W. Woodruff School of Mechanical Engineering

Georgia Institute of Technology
August 2016

Shock and Vibration Isolation Concepts through Use of Dynamic Multi-Degree-of-Freedom Mechanical Systems

Approved by:

Dr. Aldo Ferri, Advisor
School of Mechanical Engineering
Georgia Institute of Technology

Dr. Alper Erturk
School of Mechanical Engineering
Georgia Institute of Technology

Dr. Michael Leamy
School of Mechanical Engineering
Georgia Institute of Technology

Dr. Wayne Whiteman
School of Mechanical Engineering
Georgia Institute of Technology

Dr. Julian Rimoli
School of Aerospace Engineering
Georgia Institute of Technology

Date Approved: [July 25, 2016]

Dedicated to my loving wife Aleshia - whose smile always helped me find the strength I needed to continue, whose wisdom showed me the right paths to follow, whose love showed never ending support, and who would make funny faces at me every time I said something “stupid.”

ACKNOWLEDGEMENTS

I wish to thank my entire family - specifically my mother and farther, Diane and Richard Smith Jr. for their unending support and encouragement during this process. I would like to thank my advisor, Dr. Aldo Ferri, for his lengthy discussions and thought provoking guidance as we encountered numerous challenges and ideas while researching shock and vibration isolation. I would like to thank the members on my committee for their guidance and assistance. Finally, I would like to thank my many friends throughout the years, specifically: Eamonn, Ken, Lisa (“L”), Rose (“Groovie”), Ryan, Wayne, Phil, Patrick, Hengte, and Griffin, who were forced to suffer through the many highs and lows of research driven discussions.

TABLE OF CONTENTS

LIST OF TABLES

LIST OF FIGURES

SUMMARY

Shock and vibration isolation continues to be an area of great interest to structural designers and to mount manufacturers. When the input disturbance is single-frequency or narrow-band, several techniques are available to limit vibration; e.g., vibration absorbers, use of active or passive damping or structural redesign. However, when the input disturbance is transient in nature or broadband, these solution strategies are of limited effectiveness. In addition to shock/vibration isolation, mounts must fulfill a number of other equally important objectives: serve as a connection between parts, be as lightweight as possible, low cost, robust, and suitable to environmental conditions.

Isolation systems are often modeled as single-degree-of-freedom (SDOF) systems, from which a qualitative picture of the design principles and tradeoffs can be viewed. Such analyses reveal that linear, lightly damped mounts are ideal in reducing high frequency transmissibility. However, this solution is undesirable for several reasons. If the disturbance is not high frequency, but is either low-frequency or broad band, the presence of the lightly damped resonance destroys the isolation performance. Passive damping can help to control the resonant response, but this benefit comes at the expense of high-frequency isolation. Highly compliant mounts are also undesirable from a relative motion (stroke) standpoint for both static and dynamic cases.

The design space of isolation systems can be greatly expanded if one considers “dynamic” isolation systems. Passive, dynamic mounts can be thought of as multi-degree-of-freedom (MDOF) collections of springs, masses, and dampers. Such systems can be thought of as “mechanical filters” that attenuate and modify the shock disturbances before the disturbance reaches the isolated component. This thesis explores several different MDOF concepts for shock and vibration isolation; some of these MDOF systems are purely translational, while others contain translational and rotational motion. It is shown that these MDOF mount designs can be very effective in accomplishing simultaneous shock and vibration isolation objectives with relatively simple, practical designs. The performance is demonstrated using both numerical simulation as well as experimental validation studies.

CHAPTER 1.

INTRODUCTION

1.1 Overview

This dissertation is concerned with developing new isolation mounts for protection from harmonic and shock-like disturbances. The design of isolation mounts is of critical importance in the protection of structures and sensitive equipment from damage or failure. The number of different types of isolation mounts is matched only by the number of different types of disturbances that are of interest. “Vibration mounts” are intended for applications where the disturbances are of relatively low amplitude; often, the disturbances are harmonic or periodic in nature [1]. Some good examples are engine mounts, acoustic isolators, and mounts for machine tools and rotating equipment. “Shock mounts” are needed in those situations where the disturbances are relatively large amplitude, low-frequency and/or broadband in frequency content and relatively infrequent and of short duration. Examples of shock mounts include seismic foundations for buildings, shocks and struts in vehicular applications, and landing gears of airplanes and helicopters. A wide variety of different technologies and principles have been used for mounts [2]. A mount that is ideal for one application may be totally inadequate for another. In addition, it must be emphasized that isolation is but one of the functions that a mount must fulfill – it must also serve as a connection between parts so that they remain in close proximity to one another. Static load-bearing capability can also be important when they must support the weight of the system, for example, an automobile suspension. In many applications, especially vehicular and aerospace systems, the mount must be as lightweight as possible. Furthermore, they must be low cost, robust, and suitable to the temperature and environmental surroundings.

Isolation systems are often modeled as single-degree-of-freedom (SDOF) systems, from which a qualitative picture of the design principles and tradeoffs can be viewed [3]. Linear mounts are ideal in reducing high frequency transmissibility.

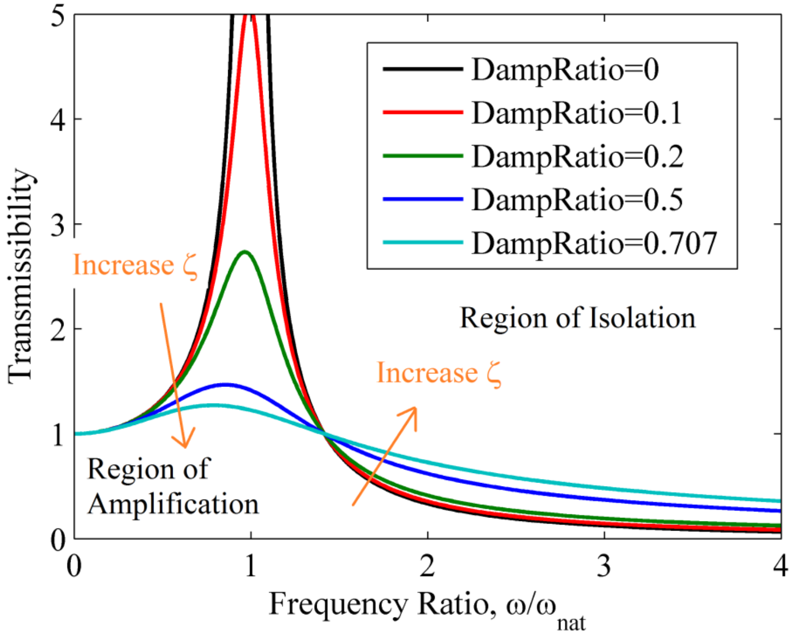

Figure 1.1: Transmissibility plot for single degree-of-freedom system; ω is the excitation frequency, ω_{nat} is the natural frequency, and ζ is the damping ratio.

Indeed, the theory depicted in Figure 1.1 predicts that the “best” isolator would have very low damping, and would be as compliant as possible so as to give the lowest natural frequency. However, this solution is unrealistic for several reasons. If the disturbance is not of high frequency, but is either low-frequency or broadband, the presence of the lightly damped resonance destroys the isolation performance. Passive damping can help to control the resonant response, but this benefit comes at the expensive of high-frequency isolation. Highly compliant mounts are also undesirable from a relative motion (stroke) standpoint for both static and dynamic cases. It is well known that the stroke and the isolation are inversely related. The stroke of the mount is constrained by geometry, size, weight, and functionality. To address these tradeoffs, many researchers have explored active, semi-active, and nonlinear isolation systems. Active or semi-active mount technology [4],[5], uses sensory signals to control the actuator forces applied by the mount. Although active and semi-active mounts have become fairly mature technology, the increased performance requires a power source and adds cost and complexity to the device. Another possibility is to use passive mounts with nonlinear stiffness and/or damping characteristics [6],[7].

An example of a nonlinear isolation system is the "zero-stiffness" or "quasi-zero stiffness" (QZS) [8], mount. Through a variety of nonlinear mechanisms, it is possible to design a compliant mount that supports a static load at the point of zero tangent stiffness [9]. Thus, the dynamic stiffness of the mount is low, even though the mount still possesses a load-bearing capacity. For this reason, these types of mounts are sometimes referred to as High Static Low Dynamic Stiffness (HSLDS). For small oscillations, the effectiveness of the HSLDS mount is attractive from the standpoint of isolation, since the isolation is theoretically perfect. But the stroke of the mount is large; in theory, the stroke would be equal to the applied base displacement. For transient loading, the performance of the HSLDS mount is more complicated [10]. For high amplitude shock loading, the nonlinear stiffness of the mount affects the performance. The HSLDS concept has some similarities with the zero-preload Hertzian chains discussed below.

1.2 Inputs

Mechanical vibrations and shocks are present in varying degrees in virtually all locations where equipment and people function. The adverse effect of these disturbances can range from negligible to catastrophic depending on the severity of the input disturbance and the sensitivity of the equipment. Vibration and shock come in a variety of forms and the type of the input can have a great influence on the response of the system. For example, a shock event can be modeled either by seismic disturbances, which can be caused by earthquakes, vehicular or foot traffic, or passing trains. Other forms of shock events are half sines, which can be the result of a "drop test"; triangular pulses, which can be simulated by a vehicle driving over a speed bump; or a complex combination of pulses, such as in an underwater explosion [11].

Another way of modeling a shock event is by an instantaneous change in a single parameter, also known as an impulsive load. The impulse can be modeled as a Dirac delta function for continuous-time systems. The short burst imparted by the Dirac delta function excites all frequency content, but can also be treated by the near-discontinuous effect that it has on system velocities [12].

Instead of short burst excitation, harmonic excitation is described as a continuous external sinusoidal force of a certain frequency applied to a system. Harmonic excitations can occur from motors, blowers or fans. In the case of harmonic excitation, a system excited at or near its resonance can have a profoundly large response when compared to the magnitude of the input. The region of larger output response when compared to input is called the region of amplification. However, excitation beyond the natural frequencies will result in a smaller amplitude response than the input and is termed the region of isolation.

In either case, the principle of isolation is the same. The purpose of a mount or isolator is to store, redirect, or dissipate incoming energy to afford a reduction of the disturbance traveling to equipment or a support structure.

1.3 Dynamic Isolation Systems

Passive isolation systems are often modeled as a “static” spring and damper, either or both of which may be nonlinear. However, the design space of isolation systems can be greatly expanded if one considers “dynamic” isolation systems. An example of a dynamic isolation system is the one-dimensional (1D) chain of springs and masses shown below in Figure 1.2. Due to the dynamic nature of these isolators, they are known to possess internal resonances, which can affect performance [13],[14]. However, it is also possible to shape the transmissibility characteristics through proper design. For example in [15] and [16], dynamic vibration absorbers are purposely embedded in the isolator. Note that this is in stark contrast to the case of vibration absorbers and energy sinks attached to the isolated mass as a free appendage [17]-[19]. Other researchers have viewed MDOF isolators as “mechanical filters” [20],[21]. The filter properties, dictated by the choice of the masses and stiffnesses, are chosen to create band-gaps within desired frequency ranges. In finite 1D chains, a particularly interesting approach is to use alternating masses that form repeating, periodic structures. These so-called “dimer chains” have very interesting properties [22]-[24].

A different isolation strategy involves using chains of masses connected with nonlinear compliance. Dario, et al. [25] used a 32 bead granular dimer chain system to

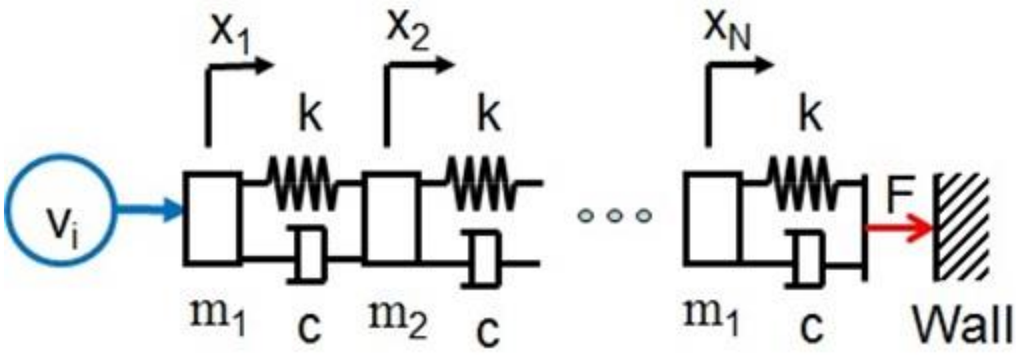

Figure 1.2: 1D Dynamic Mount.

experimentally and numerically determine the efficiency of shock-like pulse trapping and disintegration in composite dimer structures. Essentially, impulse disturbances applied at one end of the chain were attenuated and dispersed as the wave traversed the chain. The phenomenon was strongest when the beads were not pressed together; magnetically induced pre-compression tended to reduce the isolation effect. Jayaprakash, et al. [26] utilized granular dimer chains with no pre-compression and reported that for certain mass ratios the finite chains could severely limit shock transmission by redistributing energy of the propagating pulse to strongly nonlinear modes in the dimer chain and to traveling waves radiating energy to the far field. The favorable mass ratios were analyzed in terms of internal resonances associated with the lightweight masses interacting with the neighboring heavy masses. Potekin, et al. [27] validated the approximate and numerical results in [26] through experimentation on a 21 bead dimer system. The fact that certain mass ratios caused substantial reduction in the transmitted force might potentially lead to the development of practical isolation systems based on this phenomenon.

In lightly damped finite systems it was found that the disruption of propagating waves was compromised by reflections and interference [28],[29]. Due to the light damping nature found in the system, the late-arriving waves could sometimes give rise to large wall forces. It was also found that low amplitudes of wall force were often accompanied by larger displacements, consistent with the classic tradeoff between isolation and mount stroke.

Instead of utilizing purely translational motion as a means of reducing vibration, rotational motion has been considered in isolation schemes. Damped pendula have been used as a means of earthquake isolation by numerous authors [30], [31]. The structure supported by the friction pendulum system responds to the earthquake motions with small pendulum motions. In theory, the frictional damping in the pendulum systems absorbs the earthquake energy and dissipates it without causing harm to the isolated system. Friction pendulum systems are very efficient and cost effective due to their ability to alter the force response characteristics of the structure [32]. Simple pendulum systems have a small amplitude natural frequency that can be tuned to a specific disturbance frequency or resonant frequency. However, in rotating applications such as automobile engines, centrifugal pendulum absorbers have also been used with great success due to their ability to self-tune their natural frequency as rotation rate increases [33].

Rotational systems with no “inertial coupling” have no oscillation frequency and therefore couple to a wide spectrum of frequencies. Several researchers have used oscillators to investigate the phenomena of nonlinear targeted energy transfer (TET) as a means of reducing shock response [34]-[37]. It has been shown that resonance capture occurs when the end attachment has an essential nonlinearity; an essential nonlinearity is a nonlinearity with no linear component. The essential nonlinearity has been shown as a useful means of reducing vibration of the primary structure once energy transfer occurs.

In previous research [34]-[37], the nonlinear energy sink (NES) is attached to the end of the primary structure. The primary structure thus still experiences the shock event, but the response is attenuated faster. In other words, the goal of the aforementioned work is not necessarily to reduce the maximum or peak response, but to provide control of the free response. Finally the use of ball-bearings that are free to rotate in a circular track has been used in computer disk drive system to autobalance the high speed motion of disks [38].

1.4 Thesis Organization and Significant Results

This dissertation contributes several major results of importance in analyzing mounts from the standpoint of shock and vibration isolation. These results support design of state-of-the-art passive mount systems which utilize linear, nonlinear, purely translational, and mixed translational and rotational motion. The presented work makes use of theoretical, numerical, and experimental results. A summary of these results is as follows:

- Previous Hertzian chain work was investigated from the classic mount tradeoff standpoint and was shown that while certain mass ratios may result in a reduced transmitted wall force, this results in an increased first mass displacement. Furthermore, essentially cubic 1D chains were investigated and results showed similar behavior to the Hertzian chains. Both essentially nonlinear systems were compared to linear systems and it was shown that linear systems could outperform nonlinear systems for certain parameters.
- The generation of a nearly essentially cubic spring was performed through finite element analysis. The springs were created utilizing the Georgia Institute of

Technology's waterjet cutter. The nearly essentially cubic springs were then statically tested utilizing a compression/tension machine. Results indicate a high degree of nonlinear behavior. Then the aforementioned springs were then tested in both a shock and harmonic excitation environment and showcase a hardening cubic effect.

- The use of rotation in previously only translational chains showed that this extra degree of freedom can be used to reduce the transmitted wall force; however, it does not necessarily result in an increase in the first mass displacement. This result indicates the superiority of the new mount design. The improved isolation is achieved by the unique eigenstructure of the problem.
- The idea of small rotation in chains was further extended to include essentially nonlinear large oscillation internal rotation. In previously researched systems, as the length of a system increased, the wall force increased assuming the static stiffness and overall mount mass was held constant. However, in these systems the increased chains outperformed the smaller chains by removing harmful translational energy and dissipating it in non-harmful rotational motion. It was shown that increasing the chain length provided better results for both the first mass displacement and the transmitted wall force.
- The performance of the isolation concepts proposed in the thesis was optimized using a simulated annealing algorithm. The optimized systems revealed that significant improvements in the performance were possible by enlarging the space of the design parameters.

- The general design rules arrived at were: In the case of linear systems with constant mount mass and static stiffness, smaller is better for force isolation; for nonlinear systems that exploit mechanical turbulence or movement from translation to rotational motion, larger chains isolate force better. In the case of displacement isolation, longer chains performed better.
- Investigated the role of damping in chains. The dynamic mounts considered in this thesis rely on wave and modal interactions to manage the transient response characteristics and to mitigate transmitted forces. As such, the mounts do not rely upon damping to provide isolation performance. However, it is seen that modest levels of damping do not eliminate such behavior, and may even be beneficial up to a point.

1.5 Organization of the Work

Investigation of shock in purely translational systems containing linear and essentially nonlinear spring connections is investigated in Chapter 2. A theoretical upper bound on the linear chains is derived through modal decomposition. Numerical investigations show tradeoffs between the nonlinear and linear systems and indicate under certain conditions the linear systems can outperform the nonlinear systems. Chapter 3 undertakes the creation of a practical essentially nonlinear spring. The spring takes advantage of membrane forces within thin members and validates the predicted behavior using nonlinear finite element analysis. Several springs were fabricated and physically tested both statically and dynamically to verify that they worked as intended. Chapter 4 expands the mount design space to include small rotational motion and investigates the benefit of this extra degree-of-freedom. The investigation of large rotational motion is presented in Chapter 5. Chapter 6 uses the simulated annealing optimization algorithm to maximize the isolation performance of the aforementioned mount designs. Chapter 7 expands the knowledge of mount isolation by examining damping and half sine input shocks. Finally, Chapter 8 concludes with a summary and describes exciting areas of future opportunities for follow-up work in practical mount design.

CHAPTER 2.

PURELY TRANSLATIONAL CHAINS

2.1 Overview

This chapter documents the investigation of shock isolation in 1D chains. An overview of the system is given first, followed by a development of the governing equations of motion. Through numerical simulations, tradeoffs are examined between displacement and transmitted force. Parametric studies are conducted to examine how isolation performance changes with mass ratio, stiffness, and different chain lengths. Further details may be found in references [28] and [29].

2.2 Isolation System Model

Figure 1.2 shows the general layout of a one-dimensional dimer chain. The figure shows the masses as being interconnected with springs and dashpots; however, the damping in the systems under consideration is purposely kept very low. One reason for maintaining low damping levels is that linear (viscous) damping is known to be detrimental to high-frequency shock isolation [7]. It may be noted that other damping and loss models, for example structural and hysteretic damping, do not suggest as much degradation at high frequencies. Nonetheless, the damping is intentionally kept low in this study to isolate the filtering properties of the mass/spring chain. As was done in [26] and [27], the input to the system is taken to be a unit impulsive load applied to the first mass; mathematically, this amounts to an instantaneous change in the first mass' initial velocity. Thus, the impulse response of the system is the free response with all displacements and velocities equal to zero except for the first mass' initial velocity given by $\dot{x}_1(0) = v_i = \frac{1}{m_1}$. Since previous work has uncovered favorable force transmission isolation with dimer chains utilizing alternating masses, that pattern is also employed here. The mass ratio of adjacent masses is taken to be $\varepsilon = \frac{m_2}{m_1} = \frac{m_4}{m_3}$ ... Furthermore, the first and last masses are set equal, $m_1 = m_N$. It is assumed that the springs between the masses are all identical, whether they are linear, Hertzian, or cubic in nature. Even though the schematic in Figure 1.2 shows lumped masses connected by bi-directional springs, in actuality, the Hertzian case consists of spheres with uni-directional nonlinear springs. The system of equations is given as:

$$m_1\ddot{x}_1 = -c(\dot{x}_1 - \dot{x}_2) - k * f(x_1 - x_2)$$

$$m_i\ddot{x}_i = c(\dot{x}_{i-1} - \dot{x}_i) + k * f(x_{i-1} - x_i) - c(\dot{x}_i - \dot{x}_{i+1}) - k * f(x_i - x_{i+1}) \quad 1 < i < N$$

$$m_1\ddot{x}_N = c(\dot{x}_{N-1} - \dot{x}_N) + k * f(x_{N-1} - x_N) - c\dot{x}_N - k * f(x_N) \tag{2.1}$$

where *f* represents the associated spring law: linear, cubic, or Hertzian:

Linear: $$f(\Delta x) = (\Delta x) \tag{2.2}$$

Cubic: $$f(\Delta x) = (\Delta x)^3 \tag{2.3}$$

Hertzian: $$f(\Delta x) = \begin{cases} (\Delta x)^{\frac{3}{2}} & \Delta x \geq 0 \\ 0 & \Delta x \leq 0 \end{cases} \tag{2.4}$$

Note that, in the linear case, *k* is the actual spring stiffness; in the cubic and Hertzian cases, it is simply a scale factor that controls the strength of the nonlinear stiffness. As in [26], the Hertzian contact law assumes zero preload and is restricted to compressive forces only – no tensile forces.

One of the difficulties of comparing isolation performance of different mounts is that the performance is dependent on the overall mass and stiffness of the system. For example, as the mass goes up, the isolation capability usually improves. Thus, as ε and the number of masses change, it is important to keep the overall mass of the mount system constant:

$$M_{total} = \sum_{i=1}^{N} m_i \tag{2.5}$$

The performance objectives of critical interest are the wall force, F_w, and the displacement of the first mass, x_1.

Maintaining equal stiffness across all mounts is more complicated when the springs have essential nonlinearities as is the case here since the linearized stiffness is zero. To circumvent this problem, the mounts are designed such that a given static load produces a target value of displacement. In other words, a static load, f_1, applied to the first mass in the linear chain results in the same deflection, Δ_1, regardless of the number of masses/springs in the chain, N. In the case of linear springs, it is easily shown that effective static stiffness of the chain is simply $k_{eff} = \frac{f_1}{\Delta_1} = \frac{k}{N}$. To extend this concept to Hertzian and cubic springs, it is assumed that each of the N springs deflects by an identical amount, $\delta = \frac{\Delta_1}{N}$, and each spring bears the same load, f_1. Therefore,

$$kf(\delta) = f_1 \tag{2.6}$$

equation (2.6) can be used to determine the coefficient k in any of the spring laws in equations:(2.2), (2.3), or (2.4), so that each system has the same overall static stiffness as the linear chain. Obviously, this is an inexact method of normalizing the results since, for nonlinear stiffness relations, it depends strongly on the specified combination of f_1 and Δ_1. Nevertheless, it is one way of putting different isolators on a common footing.

It should be mentioned that adding a preload to the chain of masses in the Hertzian-contact case results in a non-zero linearized stiffness. But, while the preload removes the essential nonlinearity, it has also been shown to lessen the isolation effectiveness of the dimer chain [26]. It is for this reason that the preload in both the Hertzian and the cubic stiffness case is maintained at zero in this study. Thus, the isolation systems studied here are intended for lateral applications where the gravity loading acts perpendicular to the isolator chain, rather than the case where the mount must support the static weight of the mass in addition to providing isolation.

A baseline system was selected that consists of N=21 masses, 11 heavy and 10 light to match the case studied in [27]. For simplicity, the total mass of the mount was chosen to be M_{tot}=21 kg and the nominal excitation level was taken to be a unit-strength impulse. The baseline static stiffness between the masses was selected so that a load of f_1=1 Newton produced a static displacement of Δ_1=5 mm ($k_{eff} = \frac{f_1}{\Delta_1} = 200N/m$). All results presented below employ these baseline properties unless otherwise stated. For a linear system, the impulse response simply scales in amplitude with the impulse strength and scales in time with the overall stiffness and mass. But in the nonlinear case, results could differ as the static stiffness (as defined by choice of f_1 and Δ_1) is varied. The issue is explored below.

An impulsive disturbance that enters the chain at the first mass propagates down the chain and results in a time varying transient force at the wall on the right. If one plots the maximum or peak wall force versus the mass ratio, ε, a curve is generated as shown in Figure 2.1. As discussed in [26] and [27], there is a minimum in the transmitted force for a Hertzian system that occurs near ε=0.5. Also shown in Figure 2.1 is a similar result for a purely linear system with 21 masses. It is seen that the linear chain has a very different qualitative dependence on the mass ratio. Generally speaking, the wall force decreases as ε decreases. But it is also seen that the overall transmitted force is much lower than that of the Hertzian system. At ε=0.5, the cubic chain shows a similar dip to that of the Hertzian system, but it is much more accentuated. The cubic chain shows another dip near ε=0.125, which was observed in [26] for longer Hertzian chains. However, even with the significant dips in the transmitted wall force, the cubic spring system exhibits the largest overall wall force.

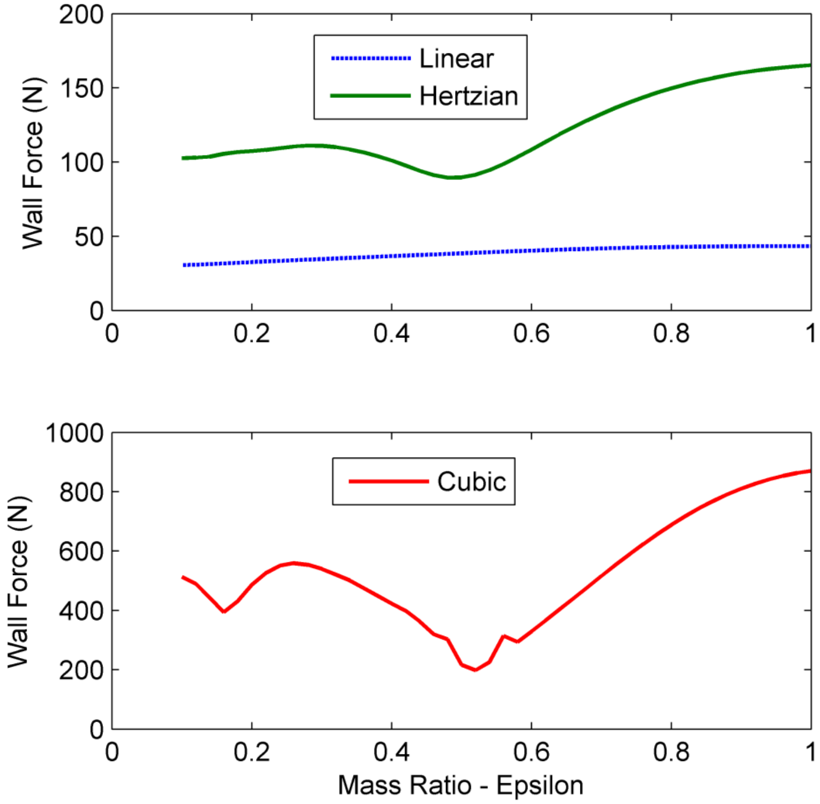

Figure 2.1: Wall Force (N) versus Mass Ratio; Hertzian, Cubic, and Linear Springs, N=21.

Before one can make a general conclusion about the relative merits of the linear, cubic, and Hertzian system, one must consider the other performance metric, namely the displacement of the first mass. It is well known that there is a fundamental tradeoff between the displacement (or "stroke") of the mount and the transmitted force/acceleration [7].

Figure 2.2 shows the maximum wall force versus the maximum displacement of the first mass as ε is varied in a chain of 21 masses. In a figure of this sort, favorable isolation performance is indicated by the proximity of the points to the origin – an ideal mount would have both low wall force and low displacement.

As stated previously, all the results shown in Figure 2.2 and Figure 2.3 use the same values for M_{tot} and k_{eff} and the damping, as characterized by the viscous damping coefficient, c, was purposely chosen to be very low in all cases. It is seen that the linear isolator has much lower force, but at the expense of higher displacement. Figure 2.3 shows a similar set of results, but includes the effect of the number of masses, N. Note that the cubic results are not shown in Figure 2.3 due to the magnitude of the force. One observation from this figure is that the wall force tends to increase with the chain length, N, while the displacement of the first mass decrease. The short chains with N=5 seem to result in a good balance between wall force and stroke.

2.3 Theoretical Linear Expectations

One of the problematic aspects of assessing isolator performance is the use of the "maximum" quantities such as maximum wall force and maximum displacement. In lightly damped systems, such as the ones under consideration here, the time at which such maxima occur is governed by a complex transient process. As an example, Figure 2.4 shows the displacement of the first mass and the wall force resulting from a unit impulse applied to the first mass of a N=21 mass linear chain with ε=0.7. Over a short

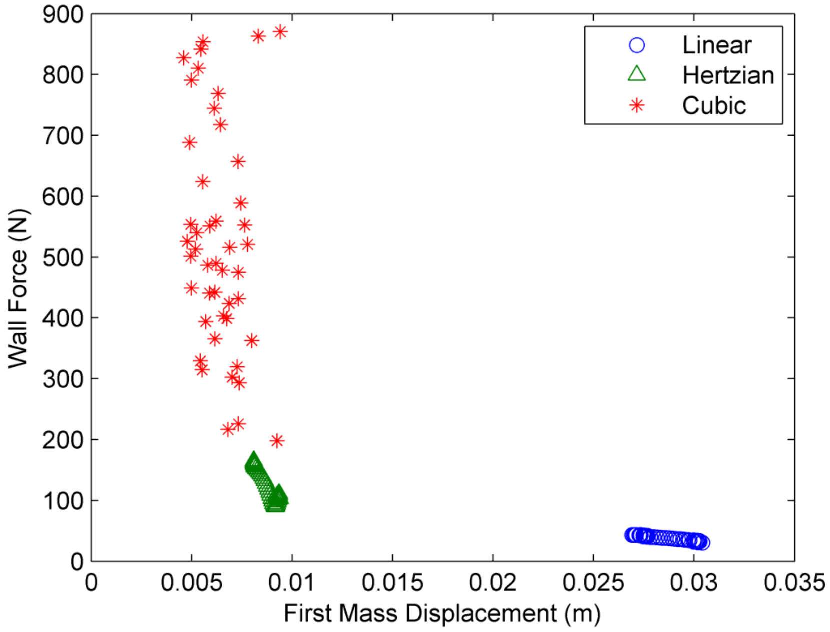

Figure 2.2: 21 Mass Hertzian, Cubic, and Linear System Comparison; various values of mass ratio, *ε*.

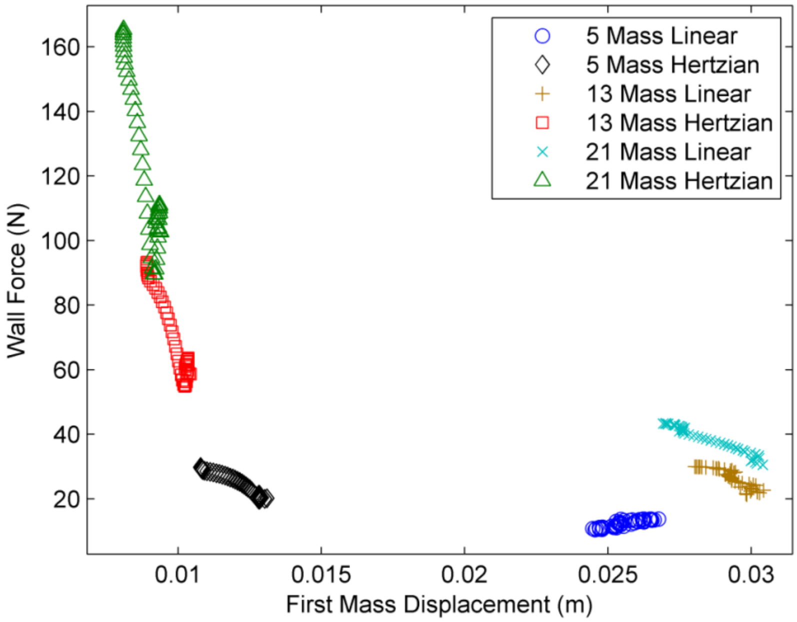

Figure 2.3: Wall Force versus First Mass Displacement comparison of linear and Hertzian spring interactions for various chain lengths, *N*, and mass ratios, *ε*.

time interval, the times at which maxima occur are easily determined. However, as shown in Figure 2.5, the situation is much more complex if one considers a long time span. Also shown in Figure 2.5 is the transfer function from the force, F_1, to the first mass displacement. In a similar way, Figure 2.5 shows that the complicated nature of determining the maximum wall force over a long time duration. The maximum value occurs at a time when the contributions from all the modes are in phase. One might hypothesize that, given non-commensurate natural frequencies that eventually all of the modal contributions will add in phase. In practice, this favorable condition may occur only after damping (even a small amount) has attenuated the response.

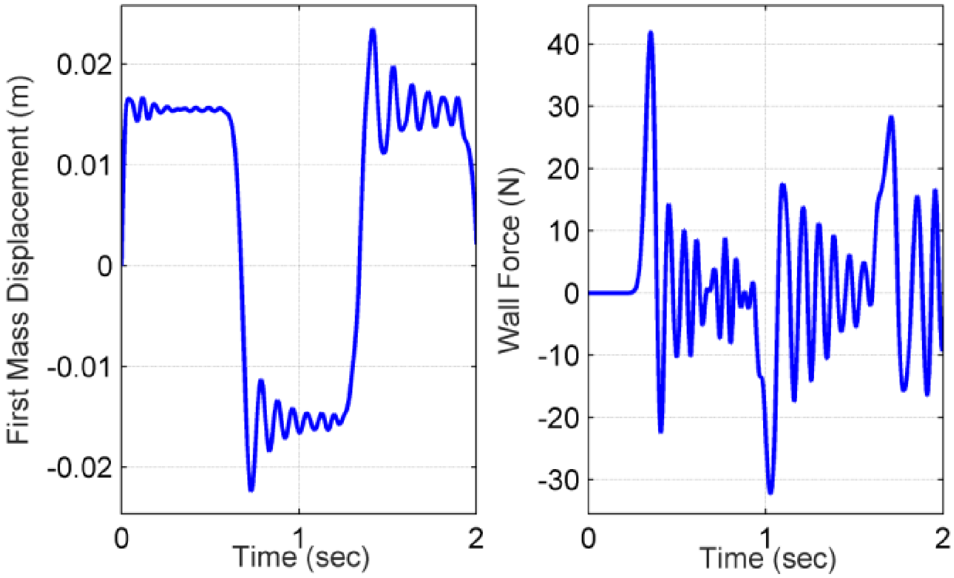

Figure 2.4: Impulse response of a linear chain with N=21 1 and ε=0.7.

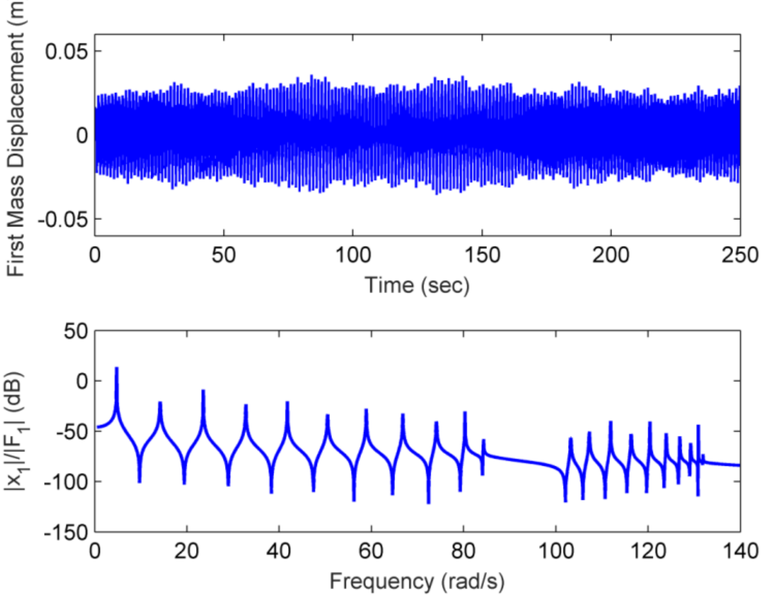

(a)

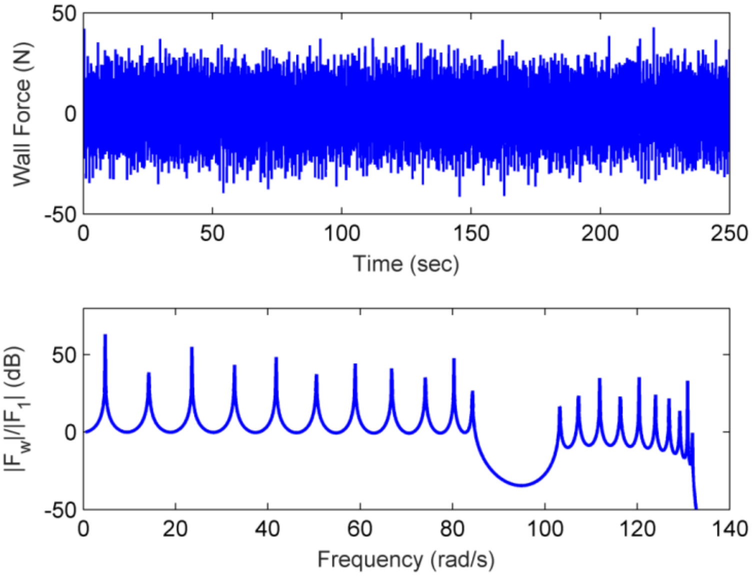

(b)

Figure 2.5: Impulse response and transfer functions for a linear chain with *N*=21 and ε=0.7. (a) displacement, and (b) wall force.

Consider an *N*-DOF linear, damped, system of equations with the first mass excited by means of a Dirac delta function:

$$[M]\{\ddot{x}\} + [C]\{\dot{x}\} + [K]\{x\} = \{e_1\}\delta(t) \tag{2.7}$$

where $\{e_1\}$ is the first Cartesian basis vector. The damping model employed in this study is a so called proportional damping model [39]:

$$[C] = \alpha[M] + \beta[K] \tag{2.8}$$

Physically, the part of the damping matrix, [C], that is proportional to the stiffness matrix, [K], corresponds to the case where each spring is accompanied by a parallel dashpot. Whereas the part of the damping matrix, [C], that is proportional to the mass matrix, [M], corresponds to the dampers going from each mass to the ground. Since the systems under consideration here do not have these types of connections, α is set equal to zero.

It is well-known that a damping matrix of the form equation (2.8) is sufficient (though not necessary) for the undamped vibration modes to uncouple the system of equations through use of the following coordinate transformation:

$$\{x\} = [\Phi]\{\eta\} \tag{2.9}$$

The columns of [Φ] are the mass-normalized, undamped normal modes. Due to mass-normalization, we have:

$$[\Phi]^T[M][\Phi] = [I] \text{ and } [\Phi]^T[K][\Phi] = [\omega_n^2] \tag{2.10}$$

where [I] is the N-dimensional identity matrix and $[\omega_n^2]$ is a diagonal matrix of the squares of the natural frequencies of the system. Because [C] is proportional to [K], [Φ] also diagonalizes [C]:

$$[\Phi]^T[C][\Phi] = \beta[\omega_n^2] = [2\zeta_n\omega_n] \tag{2.11}$$

where $[2\zeta_n\omega_n]$ is a diagonal matrix involving modal damping ratios and natural frequencies. In the case of modal damping, the values for $[\zeta_n]$ can be specified. In the case of proportional damping the ratios are seen to increase with the mode number, n, according to the linear trend:

$$\zeta_n = \frac{\beta\omega_n}{2} \tag{2.12}$$

Thus, an unfortunate artifact of this damping model is that the higher modes have higher damping than the lower modes. Substitution of equation (2.9) into equation (2.7) yields the familiar uncoupled equations in terms of the normal coordinates, η_j:

$$\ddot{\eta} + 2\zeta_j\omega_j\dot{\eta}_j + \omega_j^2\eta_j = \Phi_{1,j}\delta(t) \tag{2.13}$$

where $\Phi_{1,j}$ is the first element of the jth mass-normalized eigenvector. The underdamped time response of equation (2.13) is given by:

$$\eta_j(t) = \frac{\Phi_{1,j}}{\omega_{d,j}} exp\left(-\zeta_j\omega_j t\right)\sin\left(\omega_{d,j}t\right) \tag{2.14}$$

where $\omega_{d,j} = \omega_j\sqrt{1-\zeta_j^2}$ is the damped natural frequency of the jth mode. The wall force can be constructed from the normal coordinates using a modal sum:

$$F_w(t) = k\left(\sum_{j=1}^{N}\Phi_{N,j}\eta_j(t)\right) = k\left(\sum_{j=1}^{N}\frac{\Phi_{1,j}\Phi_{N,j}}{\omega_{d,j}} exp\left(-\zeta_j\omega_j t\right)\sin\left(\omega_{d,j}t\right)\right) \tag{2.15}$$

Note that the term in parentheses in equation (2.15) is the displacement of the mass closest to the wall; i.e., the Nth mass. For the undamped system, an upper bound for equation (2.15) can be found by assuming that there exists a time t_{max} such that $\sin\left(\omega_{d,j}t_{max}\right) = \pm 1$ for all j: $1 \le j \le N$. Specifically, we need for $\sin\left(\omega_{d,j}t_{max}\right) = +1$ for every mode having $\Phi_{1,j}\Phi_{N,j} > 0$ and for $\sin\left(\omega_{d,j}t_{max}\right) = -1$ for every mode having $\Phi_{1,j}\Phi_{N,j} < 0$. We conjecture that over an unbounded time span, it is always possible to find a time such that this fortuitous situation occurs. Thus, for zero damping, an upper bound for the wall force is:

$$F_{max} = F_w(t_{max}) = k\left(\sum_{j=1}^{N} \Phi_{N,j}\eta_j(t)\right) = \sum_{j=1}^{N} \frac{k|\Phi_{1,j}||\Phi_{N,j}|}{\omega_j} \tag{2.16}$$

The upper bound can be quite conservative at times. Figure 2.6 shows a comparison of the maximum wall force vs the upper bound for a range of mass ratios in a dimer chain of length N=9. Simulation results for two different values of β are shown. For β=1x10^{-9}, the modal damping ratios are less than 5x10^{-8} for all values of ε; for β=1x10^{-3}, the modal damping ratios are less than 5x10^{-2}. The simulated wall force is computed by taking the maximum absolute value of equation (2.15) over the range of 0<t<1000 s. For low damping, it is seen that the actual maximum wall force is not a smooth curve; this is because small changes to ε cause slight changes to the natural frequencies, ω_n, which can result in large changes to the time at which the mode contributions add constructively. As β increases, the simulated maximum wall force curve becomes much smoother, but the upper bound becomes more conservative. It was also found from simulations using longer chains (not shown), that the upper bound grew more conservative; this was due to the decreased probability of all modes contributing in phase over the finite time duration investigated. An initial study using cubic-stiffness springs showed similar, complicated behavior and trends for the wall force and for the maximum value of the displacement of the first mass. No attempt was made to find an analytical upper bound for the cubic or Hertzian spring case.

2.4 Explanation by Propagation by Energy

The efficacy of the dimer chain as an isolator depends critically on the way that energy propagates down the chain. In a finite-length chain, the influence of wave reflection and attenuation influence the maximum force transmitted to the wall. A very

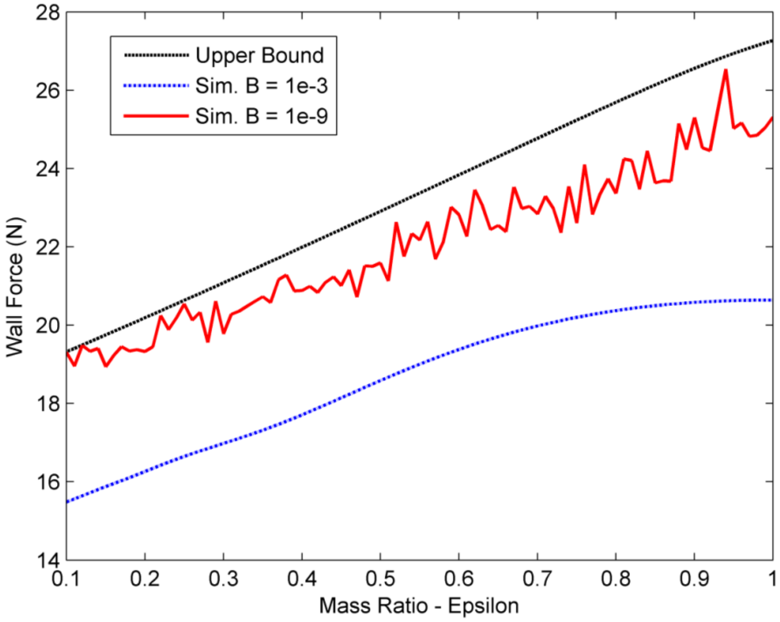

Figure 2.6: Wall force versus mass ratio for a *N*=9 mass system; comparison of simulation results with upper bound.

simple but effective way of showing this is through “energy plots. ”For a finite-length, lumped mass system, this is somewhat heuristic analysis because kinetic energy must be “lumped” at each mass location, and potential energy must be lumped at the location of each spring. This is similar to the contour plot presented by Hussein et al.[23], which showed displacement vs the spatial and temporal axes.

Figure 2.7 shows the propagation of energy in an *N*=9 mass linear chain with ε=1.0. The plot shows the energy as a function of space and time. The numbers along the abscissa roughly correspond to the location of each mass and are where the kinetic energy is centered; the location between each mass correspond to the spring location where the potential energy is centered. For this uniform chain with equal masses, it is seen that the energy neatly propagates along the length of the chain for the first passage of the wave and partially through the first reflection. The concentration and intensity of the energy as the wave hits the wall is consistent with the high wall forces seen in Figure 2.1 when ε =1.0. After the first reflection, the energy is seen to scatter and to diffuse among the masses/springs. This situation can be contrasted with that shown in Figure 2.8, which shows the same 9-mass linear chain but for a mass ratio of ε =0.1. In this case, the wave backscatters almost immediately, resulting in a diffusion of energy amongst many masses/springs before the first time that the wave impinges on the wall. This is consistent with the much lower wall forces displayed in Figure 2.1 for small ε. It should be added that, due to the very low damping used in these simulations, the total energy of the system does not attenuate appreciably; instead, the energy is simply redistributed from a highly concentrated to a more diffuse state as ε is decreased.

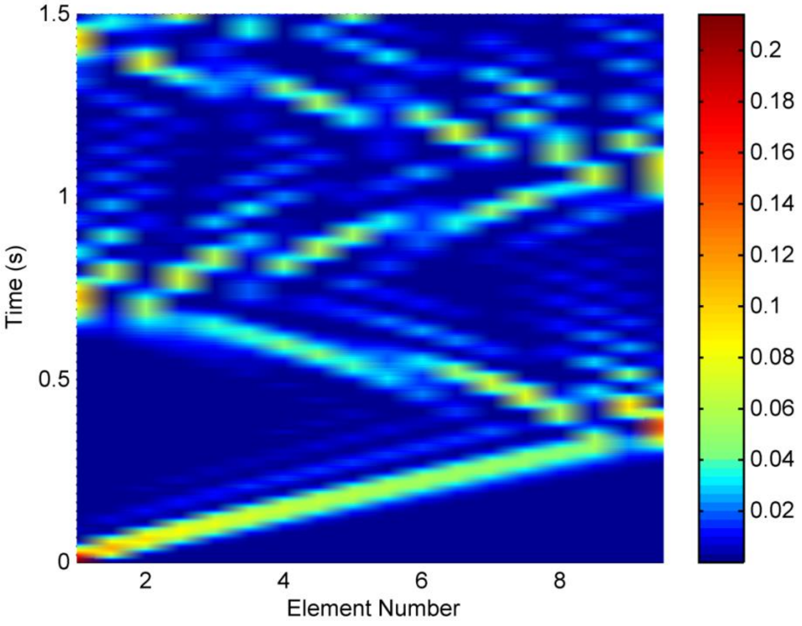

Figure 2.7: Energy Evolution for linear system with mass ratio ε=1.0, N=9, M_{tot}=21kg, Δ_1=5mm for a static load of 1 Newton.

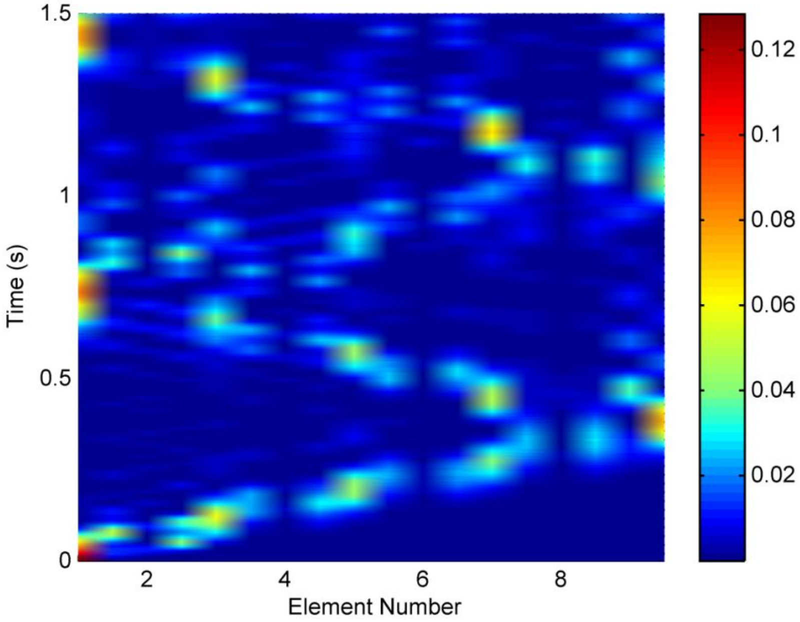

Figure 2.8: Energy Evolution for linear system with mass ratio ε=0.1, N=9, M_{tot}=21kg, Δ_1=5mm for a static load of 1 Newton.

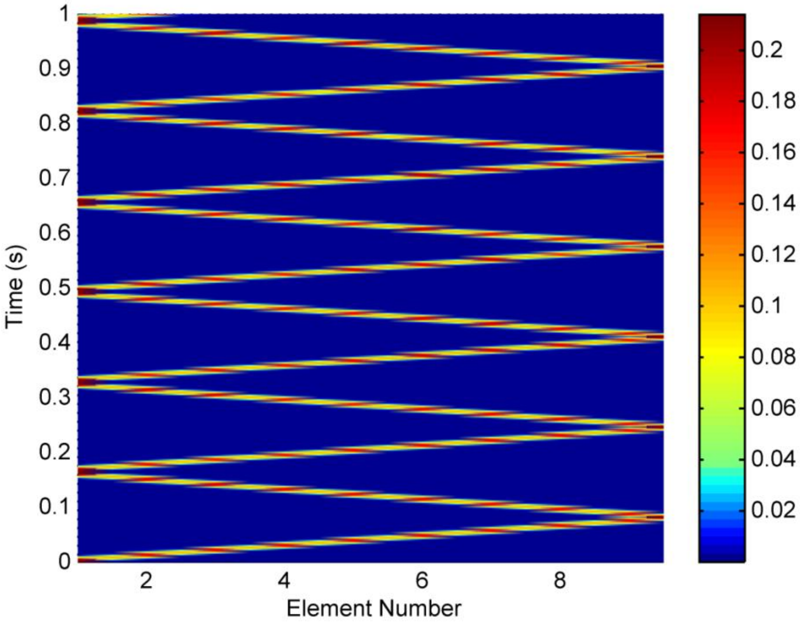

Figure 2.9: Energy Evolution for nonlinear system with mass ratio ε=1.0, N=9, M_{tot}=21kg, Δ_1=5mm for a static load of 1 Newton.

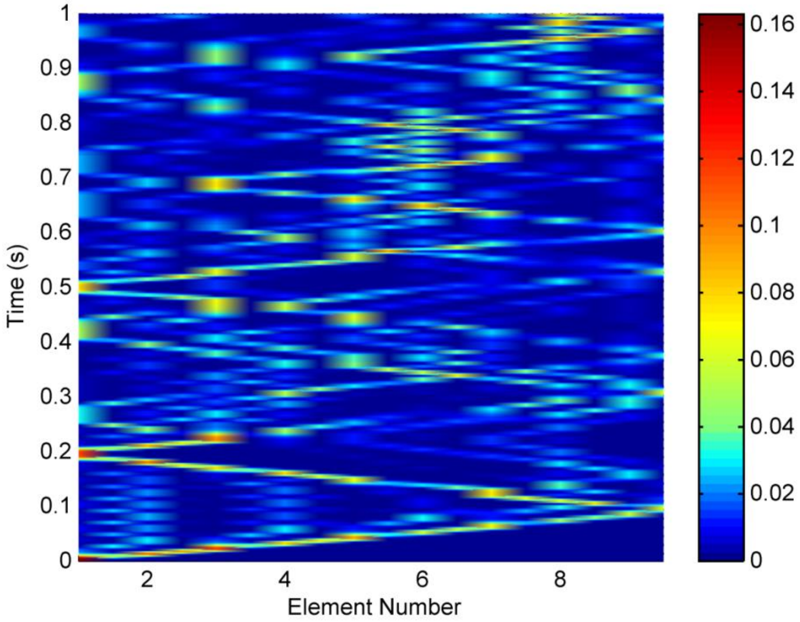

Figure 2.10: Energy Evolution for nonlinear system with mass ratio ε=0.465, N=9, M_{tot}=21kg, Δ_1=5mm for a static load of 1 Newton.

For a nonlinear system, the situation is quite different. Figure 2.9 shows the energy propagation through an N=9 mass chain with cubic spring stiffness. For the case of a perfectly-tuned chain with equal masses (ε =1), the energy stays together over many transmission/reflection waves. This corresponds to an anti-resonance situation as discussed in [24]. For the case of ε =0.465 shown in Figure 2.10, a resonance situation exists, and the energy transmission is seen to be greatly disrupted. Essentially, the small masses are left to oscillate at a higher frequency, keeping some energy trapped in the lighter masses. The situation depicted in Figure 2.9 and Figure 2.10 may be contrasted with the case of Hertzian contact. Because the Hertzian springs are uni-directional, the first mass in the chain becomes detached when the disturbance wave propagates back to the excitation location. This process repeats each time that the wave returns to the free end, and thus the masses are “shed” one by one as time goes on. Obviously, this situation would not be practical in a physical isolation system; hence the energy plots for the Hertzian case are not shown here.

The energy propagation plots are very useful in explaining how changes to ε affect the performance of the dimer chains. To a large extent, the physical basis of the linear chain and the nonlinear chain are different. The linear chain seems to benefit from a high impedance mismatch between masses, whereas the nonlinear chains show high performance in situations of resonance. However, what is more important from the standpoint of isolator performance is the tradeoff between the wall force and the relative displacement for a given input type and amplitude. This tradeoff is more fully studied in the next section.

2.5 Comparison of Isolator Performance

The results above show the difficulty in comparing isolators. Figure 2.2 and Figure 2.3 show that the Hertzian isolator produces higher wall forces than the linear isolator of equal mass and equal static stiffness. However, the linear isolator achieves this improved isolation at the expense of higher displacement.

For the Hertzian chain, an interesting tradeoff is evident if one considers the dimer chains of different length. Figure 2.11 shows the wall force as a function of ε for chains of different lengths. For the same cases displayed in Figure 2.11, Figure 2.12 shows the maximum displacement of the first mass. For these two figures, the overall mass and static stiffness is kept constant as N and ε are varied. It is seen that the resonance situation that leads to favorable wave attenuation does not emerge until the chain attains a sufficient length. This fact was previously uncovered in [25] and [26].

However, when one keeps the overall mass equal and the overall static stiffness equal, it is seen that the attenuation associated with increasing chain length is actually associated with higher wall forces. Indeed, as the difference between the maximum wall force and the “local minimum” wall force near $\varepsilon=0.5$ grows larger, so does the absolute level of the wall force. This tends to negate any benefit achieved by the nonlinear dimer chain. However, as seen in Figure 2.12, as the wall force increases with N, the maximum displacement of the first mass decreases. This trend was also observed in dimer chains with cubic stiffness; however, the results are far less “clean” and not shown. Simulation results, not shown, were conducted for N values as large as 221. The trend towards higher wall force as N increases is attributable to the fact that as the masses reduce in size, the inter-mass spring stiffness must increase in order to keep the overall static stiffness, k_{eff}, the same. In the limit of a continuum, the wall force actually becomes unbounded, but that result is an artifact of the non-physical nature of an ideal, impulsive excitation.

As stated above, however, the “static stiffness” of a nonlinear isolator is somewhat ambiguous. To really compare the different types of isolators, one must consider a range of stiffnesses, a range of mass ratios, and a range of chain lengths. Figure 2.13 shows one such comparison of wall force versus first-mass displacement as the stiffness parameter k is varied. (Note that changing the “overall static stiffness” amounts to a change in the parameter k in equation (2.1). The result in Figure 2.13 is produced by parametrically varying the parameter k, keeping all other system properties constant. As stated before, good isolation is indicated by the proximity of the points to the origin, assuming that force and displacement (stroke) are equally weighted.

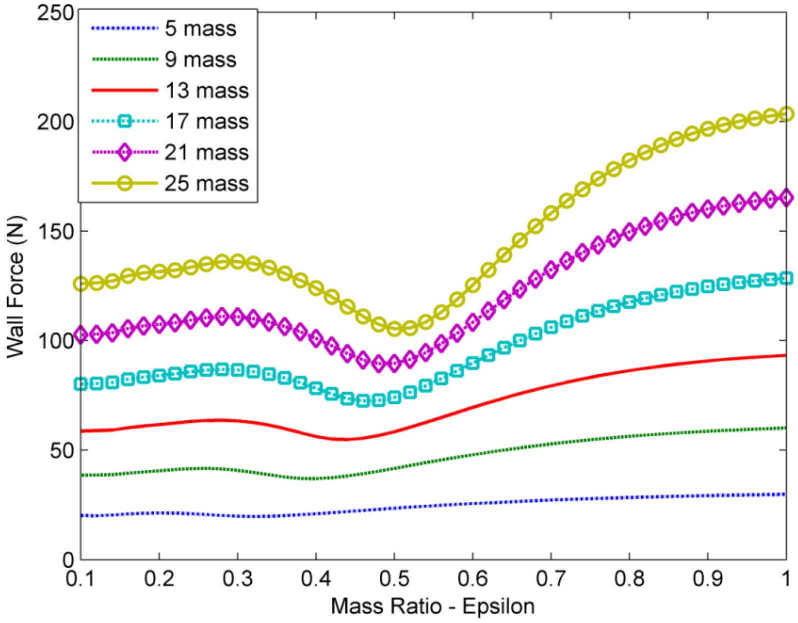

Figure 2.11: Wall force versus mass ratio for varying Hertzian chains; M_{tot}=21kg, Δ_1=5mm for a static load of 1 Newton.

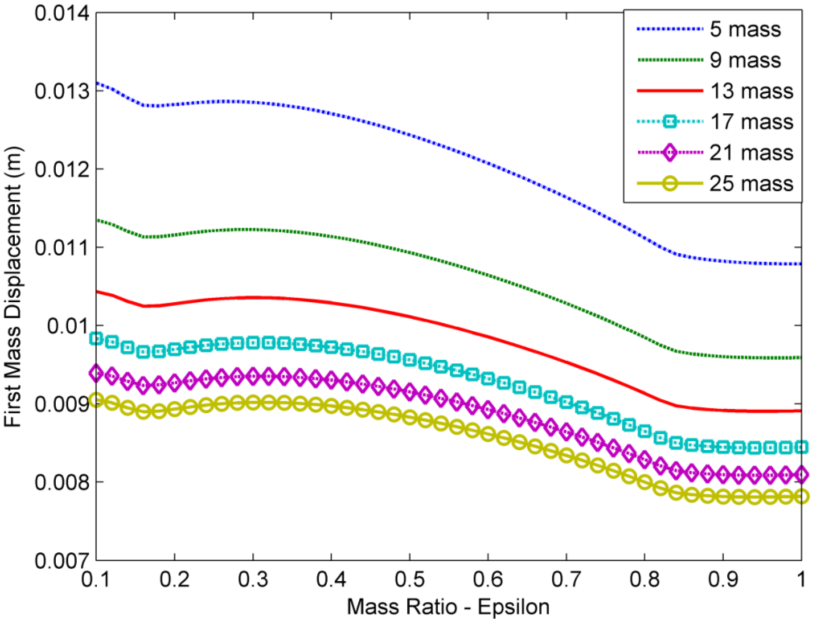

Figure 2.12: First mass displacement versus mass ratio for varying Hertzian chains; M_{tot}=21kg, Δ_1=5mm for a static load of 1 Newton.

The triangles correspond to a chain of 21 masses interconnected with zero-preload Hertzian springs. The mass ratio is ε=0.5 and the overall mass of the isolator is 21kg. As the stiffness parameter k of the Hertzian spring (see equation (2.4)) is increased, the displacement decreases while the wall force increases in a classic tradeoff curve. The Hertzian contact case is compared to a 9-mass linear chain having a total mass of 21kg and a mass ratio of ε=0.3. As the linear spring stiffness is varied, another tradeoff curve is produced. It is seen that, in this case, the linear mount has better isolation performance. The physics behind the isolation performance of the Hertzian spring system are fairly complicated. In [26] and [27], the favorable performance in the vicinity of ε=0.5 are tied to internal resonances in the chain. In the linear case, the isolation performance seems much simpler to understand. The performance of linear spring/mass isolation chains has been discussed in references [21] and [22].

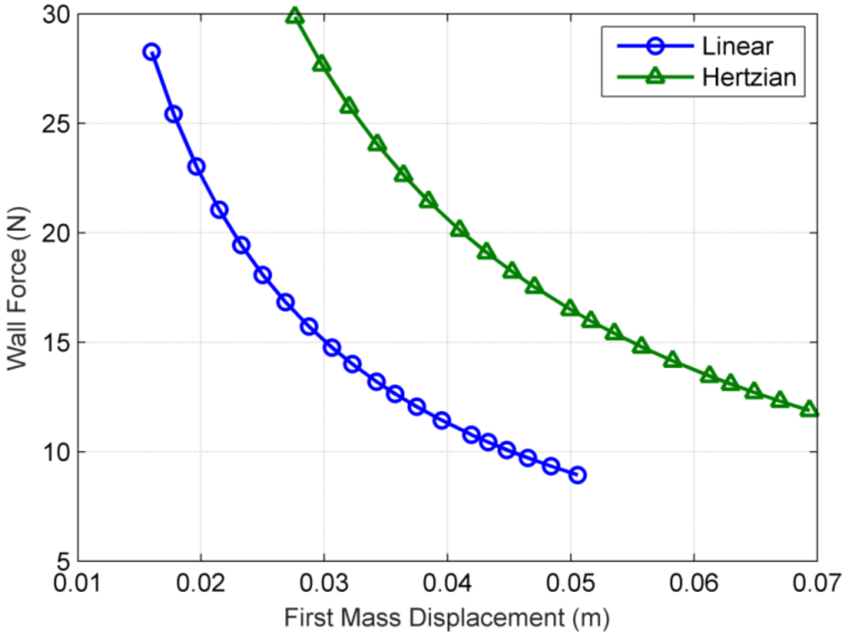

Figure 2.13: Max wall force versus the maximum displacement of mass 1. Hertzian chain of 21 masses, ε=0.5; Linear chain of 9 masses, ε=0.3. Varying stiffness.

Figure 2.14 and Figure 2.15 show similar tradeoff curves for the Hertzian and linear cases, respectively. In these figures, total isolator mass and overall static stiffness are held constant while the number of masses is increased. Various values of ε are examined. In the linear case, there is a clear trend of better performance as N is decreased. However, the result for the Hertzian case is quite different. This is an indication of the fact that the isolation of the Hertzian contact case generally favors longer chain lengths [26].

Parametric studies were also conducted on chains having cubic-stiffness springs and the results were found to be similar in nature to those of the Hertzian case. The major difference is that the times at which the global maximum of the wall force or first-mass displacement occurs can change abruptly as a physical parameter such as ε is slightly varied. This causes parametric curves for cubic-spring chains to appear more irregular than those for the Hertzian case. But while the curves for the cubic-stiffness case are less smooth, the qualitative trends are very similar to those shown above for the Hertzian case.

2.6 Conclusion

In this chapter, we have compared different isolation mounts based on 1:1 dimer chains. One system used chains interconnected with zero-preload Hertzian contact springs. The performance of the Hertzian system was contrasted with that of a fully linear chain and a fully cubic chain. The design space was restricted in several important ways. Most notably, the overall mass of the isolation chains was held constant as the mass ratio was varied. An effort was also made to hold the overall static stiffness of the three systems equal; though, maintaining a constant static stiffness is far more problematic

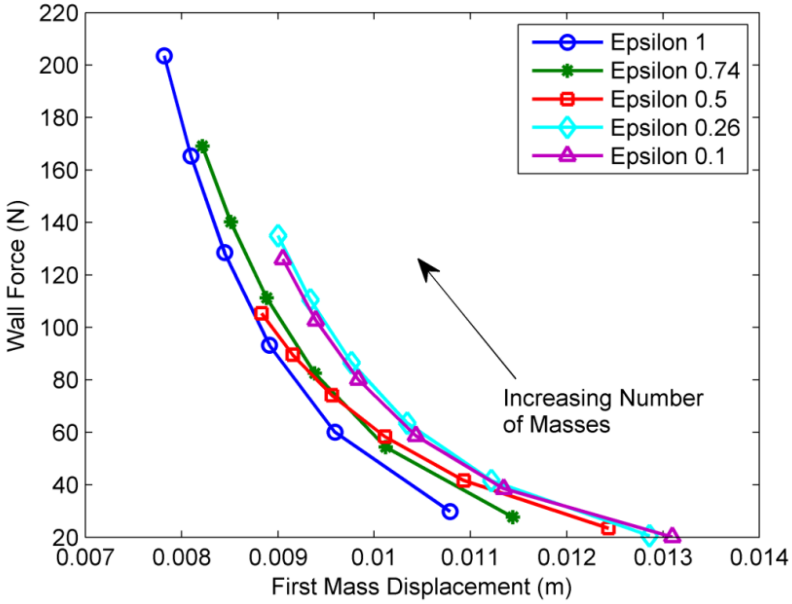

Figure 2.14: Max wall force versus maximum displacement of mass 1. Hertzian contact with zero pre-load. Various values of ε and chain length, N. M_{tot}=21kg, Δ_1=5mm for a static load of 1 Newton.

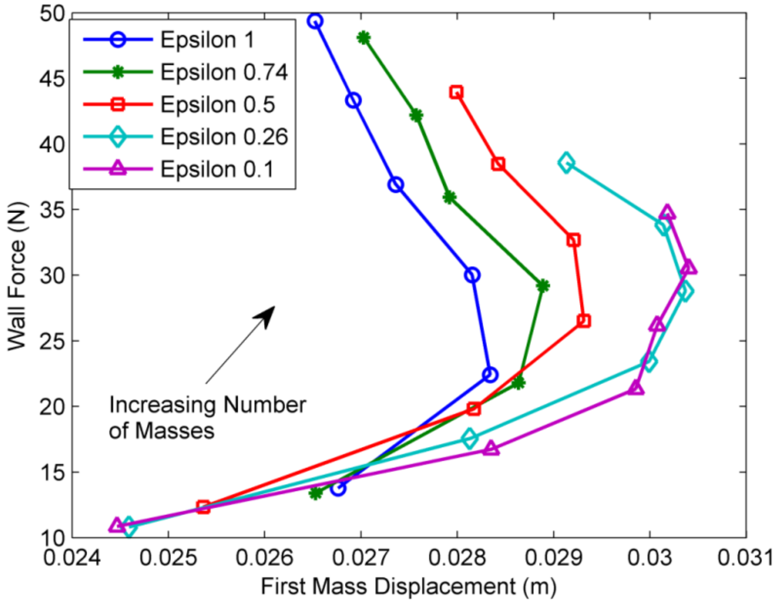

Figure 2.15: Max wall force versus maximum displacement of mass 1. Linear spring case. Various values of ε and chain length, N. M_{tot}=21kg, Δ_1=5mm for a static load of 1 Newton.

due to the nonlinear characteristics of the Hertzian and cubic springs. The system's excitation was in the form of an initial velocity on the first mass (impulsive force) and the performance criteria were displacement of the first mass and transmitted wall force at the end of the chain. For simplicity, the wall in this study was immovable, but in an actual system the chain would connect to an object or structure being isolated.

The chain possessing Hertzian spring contact is known to transmit minimum force at certain mass ratios. However, when the tradeoff is considered between the transmitted force and displacement (stroke), the performance was far more difficult to assess. In particular, the performance of the Hertzian chain was outperformed by smaller length linear chains.

The interesting minimum in the transmitted force of the Hertzian and cubic chain seems to present an opportunity for the creation of practical mount isolation systems. The next chapter explores the fabrication of a cubic spring design.

CHAPTER 3.

REALIZATATION AND TESTING OF A NONLINEAR SPRING

3.1 Overview

The results of Chapter 2 showed the potential performance advantage of dimer chains with essentially nonlinear springs. The question remains as to whether such types of springs can be practically realized apart from Hertzian contact. The ability of the interconnections to act in compression and tension is necessary for the mount to be practical, which rules out Hertzian contact. Thus, this chapter documents the design, creation, and experimental validation of an essentially nonlinear cubic spring. The design process involves starting with a simpler system and evolving that idea into an easily fabricated spring. The nonlinear characteristic of the spring design is validated through the finite element process. Afterwards the spring is created out of 6061 Aluminum and statically tested to further verify the nonlinear behavior. Finally, the spring is experimentally investigated in a two degree-of-freedom system undergoing harmonic excitation and in a six mass shock excitation.

3.2 Finite Element Analysis

Nonlinear springs are a class of compliant mechanisms having a nonlinear relationship in the load-displacement function. Currently there exists a limited selection of nonlinear springs, for example conical springs, barrel springs and springs with variable pitch along their length. In the aforementioned case the nonlinear contribution to the force is usually small until deflections become large. The study of dynamics and vibrations in systems of springs exhibiting small nonlinear behavior in the force-displacement relationship generally makes use of a governing equation of the form:

$$F(\delta) = k_1\delta + \varphi k_2 \delta^{\sigma} \tag{3.1}$$

where $\sigma \neq 1$, and $\varphi \ll 1$ [40]-[42]. The behavior of dynamic systems containing spring functions of this form can be analyzed through use of the method of multiple scales [43]. However, in the case of an essentially nonlinear spring (k_1=0 in equation (3.1)), the perturbation expansion, even for small φ, does not hold. Systems exhibiting essential nonlinearities are primarily investigated in the targeted energy transfer (TET) community [44].

One way of creating an essentially cubic nonlinear stiffness is through the transverse deflection of a wire fixed at each end, shown in Figure 3.1 (a).

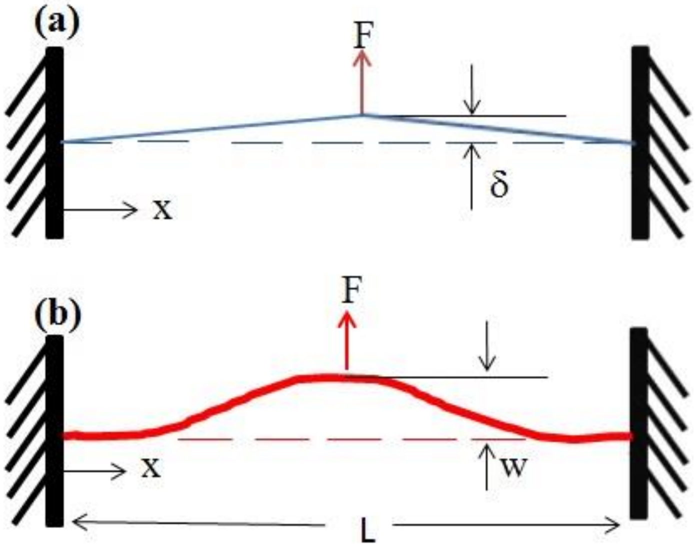

Figure 3.1: (a) Fixed-fixed string, (b) clamped-clamped beam.

A Taylor series expansion about the equilibrium position leads to the force-displacement relation [45]:

$$F(\delta) = \frac{EA}{l^3}\delta^3 + O(\delta^5) \tag{3.2}$$

where E is the modulus of elasticity, A is the area, l is the length of the wire and δ is the transverse deflection of the wire. For small displacements with respect to the span, l, of the wire, equation (3.2) may be simplified to:

$$F(\delta) = k\delta^3; k = \frac{EA}{l^3} \tag{3.3}$$

This approach can be utilized to realize an essential cubic stiffness nonlinearity. A more general treatment of force-displacement loads can be found in reference [46]. However, to create a chain (as previously studied above) of such elements would involve the difficulty of attaching numerous clamped wires. Furthermore, the clamped locations have to be rigid and would require a configuration that attaches the clamped section to a rigid, stationary location, which may be difficult to realize in the case of an isolation mount. To circumvent these shortcomings a new spring design is proposed and is shown in Figure 3.2.

The thin (1.52mm) but lengthy (228.6mm) cross members behave similar to a wire or string. The thick (12.70mm) side members are designed to act as a rigid clamp that induces the membrane forces which result in the nonlinear behavior. Finally, the attachment locations on the top and bottom (7.62mm wide) will allow for assembly into a chain - similar to how current linear springs available in the market assemble. To determine if the current configuration will result in a highly nonlinear spring, a Rayleigh-Ritz method for large-amplitude vibration is investigated, similar to the work in [47].

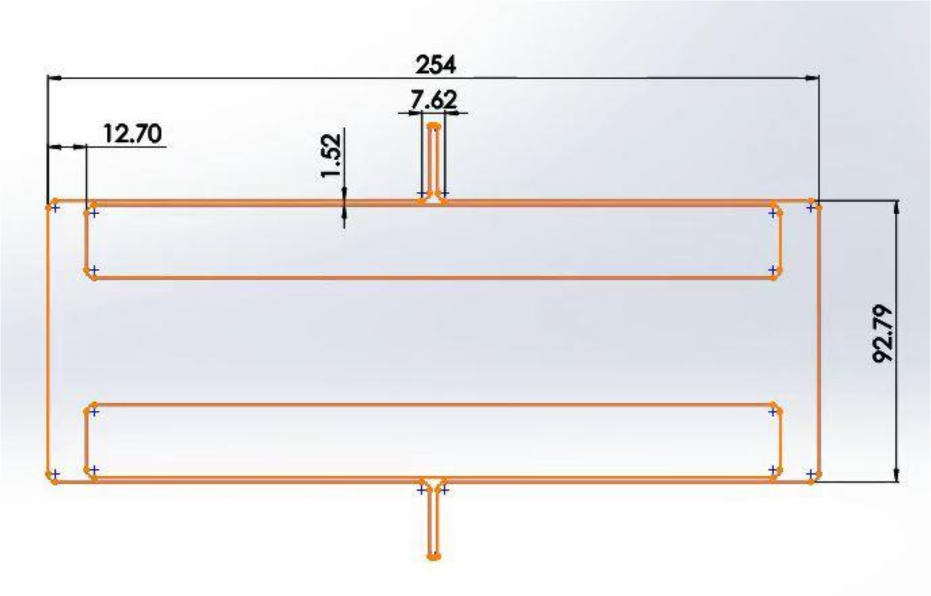

Figure 3.2: SolidWorks drawing of the essentially nonlinear spring with important dimensions shown in mm.

The strain energy and kinetic energy for a beam can be written as:

$$U = \frac{1}{2}\int_0^L \left[EA\left(u_x^2 + u_x w_x^2 + \frac{1}{4}w_x^4\right) + EIw_{xx}^2\right]dx \tag{3.4}$$

$$T = \frac{1}{2}\int_0^L m\dot{w}^2 dx \tag{3.5}$$

where *U* is the strain energy, *T* is the kinetic energy, *E* is the modulus of elasticity, *A* is the cross sectional area of the beam, *I* is the cross sectional area moment of inertia, *m* is the mass of the beam per unit length, *u* is the axial deflection, *w* is the transverse deflection, *x* is the spatial coordinate of the beam measured from the left most fixed end location, $()_x$ is differentiation with respect to x and $\dot{()}$ is differentiation with respect to time. An approximate solution is sought, based on approximating the axial and transverse displacement fields using admissible functions. The admissible functions must satisfy the kinematic boundary conditions for the clamped-clamped beam. For transverse deflection, the following admissible function is selected, shown in Figure 3.1 (b):

$$w = w_o(t)\left(1 - \cos\left(\frac{2\pi x}{L}\right)\right) \tag{3.6}$$

where w_o is the midspan deflection in the transverse direction at any instant in time. Equation (3.6) is substituted into equations (3.4) and (3.5) and the equation of motion is found using Lagrange's equation:

$$\frac{d}{dt}\frac{\partial L}{\partial \dot{q}_j} - \frac{\partial L}{\partial q_j} = 0 \tag{3.7}$$

where L is the Lagrangian (*L*=*T*-*U*). Equations (3.4) to (3.7) yield the single-degree-of-freedom equation of motion:

$$M\ddot{w}_o + \frac{16\pi^4 EI}{3L^4} w_o + \frac{2\pi^4 EA}{L^4} w_o^3 = 0 \tag{3.8}$$

where the system's linear stiffness coefficient is represented by the term in front of w_o and the system's cubic stiffness coefficient is represented by the term in front of the w_0^3 and *M* is given by the equation:

$$M = \int_0^L \left(1 - \cos\left(\frac{2\pi x}{L}\right)\right)^2 \rho A \, dx = \frac{3\rho A L}{2} \tag{3.9}$$

An important observation gained from this approximate analysis is that the degree to which this system will act as an essentially nonlinear spring depends on the ratio of the cross-sectional area moment to the cross-sectional area, *I*/*A*. If *I* << *A*, then the beam members in the spring will closely approximate the behavior of an essentially-nonlinear spring. In the case of the part shown in Figure 3.2, cut from a 1/16-inch thick plate of 6061 Aluminum with E=68.9 GPa, the linear term is: 6.1e^{3} N/m and the cubic term is: 1.18e^{10} N/m^{3}, showcasing the highly nonlinear behavior of the spring design.

The aforementioned analysis assumes that the supports for the cross members were perfectly clamped and utilized a one-term Rayleigh-Ritz approximation to determine the equations of motion for the transverse deflection of the beam. To further verify the nonlinear behavior of the proposed spring design, a static structural finite element analysis (FEA) was performed in ANSYS and is shown in Figure 3.3. In order to replicate the fixturing conditions of the experiment (described below), a fixed support (no displacement, no rotation in any direction) was applied to a set of nodes near the bottom of the spring element. While the base of the spring was restrained, various deflections were imposed on the vertical beam at the top of the structure. The displacements were gradually applied through multiple steps with ANSYS verifying convergence of the displacement and force before proceeding to the next displacement increment. The reaction force at the nodal constraint was output and used to generate the force-displacement relationship, which is shown in Figure 3.4.

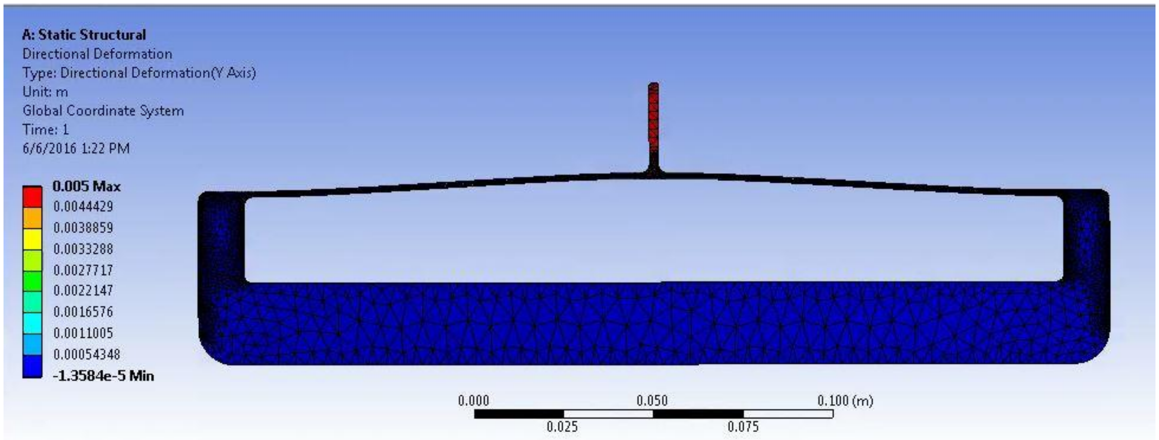

Figure 3.3: Static structural FEA of the essential nonlinear spring design, with applied displacement of 5mm.

From Figure 3.4 we can see the highly nonlinear behavior of the spring resulting from deflections in the 2 to 5 mm range and beyond. For smaller deflections, the spring may behave in a more linear region as indicated by the cubic fit, which was computed using a least squares fit in MATLAB and forcing the curve through the origin. To investigate the amount of nonlinearity further, the total force in the spring is compared by the percent of the force coming from linear, quadratic and cubic subcomponents.

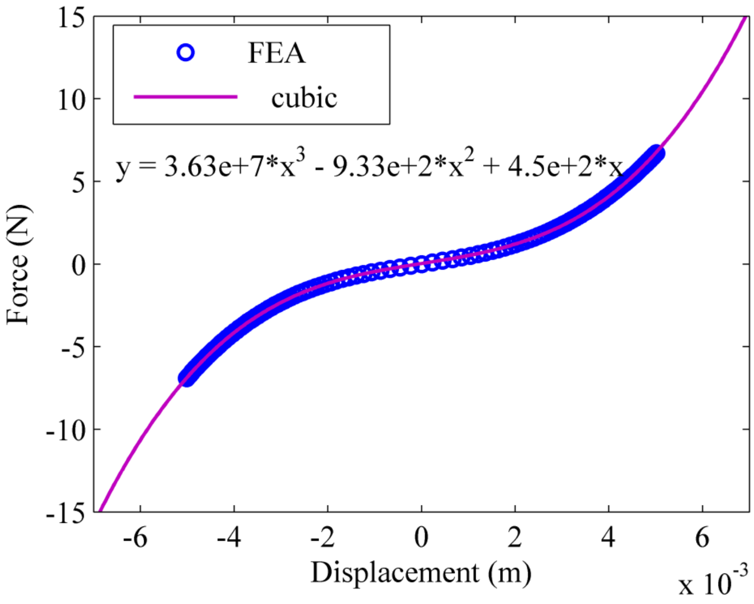

Figure 3.4: Cubic fit of the FEA simulation data.

As seen in Figure 3.5, for deflections of 5mm or more, the cubic component of the force is at least 70% of the total force, which implies that the spring begins to look more and more like a pure cubic spring as the deflection increases.

Ideally for the entire range the cubic contribution to the force would be 100%; however, this is practically impossible to realize even in the case of a clamped wire. For example, a clamped boundary condition will exhibit slipping of the wire in any experimental investigation.

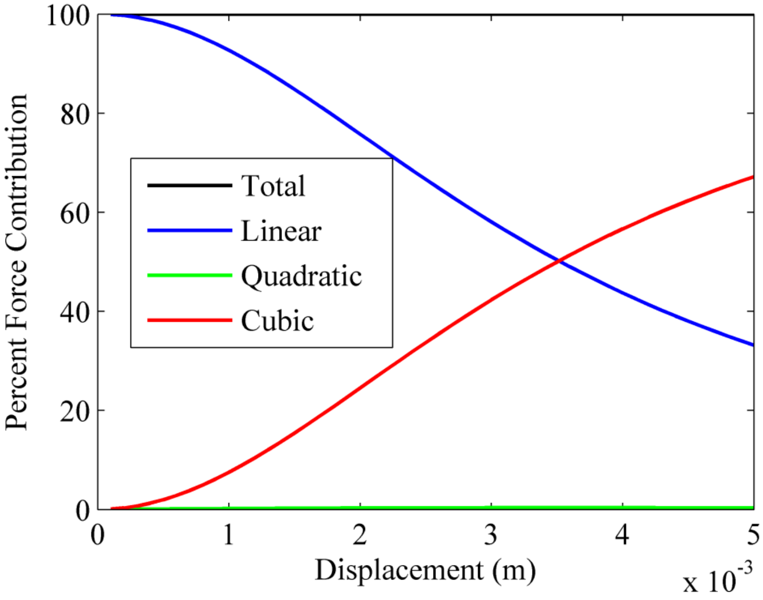

Figure 3.5: The total force due to the nonlinear spring from the subcomponents.

3.3 Static Experimental Analysis

The cubic springs were cut from 1/16inch 6061 Aluminum utilizing the Maxiem 1515 waterjet cutter. To verify the results of the FEA, the cubic spring was experimentally tested on an Instron 5848 screw-driven load train operated in displacement control with a 100N Instron load cell number 2530-427. Unfortunately, the test was conducted on half the spring (cut about symmetry axis) due to the limitations of the testing device; however, the tested spring can be viewed as one element of a series combination of identical nonlinear springs.

Figure 3.6 shows the experimental data fitted with a cubic polynomial via a least squares analysis in MATLAB. Again, it is shown that the system exhibits a strong nonlinear behavior. Since only half the spring was tested, two springs would need to be in series to match the original spring design as shown in Figure 3.2. To determine how nonlinear springs behave in series we investigate a purely cubic spring. Similar to the analysis for a linear spring, we write the formulas for the forces in each spring and for a total combined spring:

$$F_1(x_1) = kx_1^3$$

$$F_2(x_2) = kx_2^3$$

$$F_{total}(x) = k_{eq}(x_1 + x_2)^3 \tag{3.10}$$

where k_{eq} is the equivalent spring. Since the force in each spring is equal, (F_1=F_2=F_{total}), it can be shown that x_1=x_2.Plugging in the aforementioned results into the total force equation from (3.10):

$$F_{total} = k_{eq}(2x_1)^3 \tag{3.11}$$

The force in each spring is equal, therefore we can set the result of F_{total} equal to F_1, which results in the determination of the equivalent stiffness:

$$k_{eq} = \frac{k}{8} \tag{3.12}$$

Similar analysis can be performed for the quadratic and linear part of the fit equation. Ultimately this leads to the result that the spring’s force-displacement relationship is:

$$f(x) = 4.54 * 10^6x^3 - 2.33 * 10^2x^2 + 2.25 * 10^2x \tag{3.13}$$

As shown in Figure 3.4 and Figure 3.6 the FEA and the static experimental test indicate that the spring exhibits a high degree of cubic behavior in the range of deflections shown. However, there is still a significant linear component. The comparison between the experimental and finite element analysis force-displacement relationship is shown in Figure 3.7. As shown in the figure, the finite element analysis provides excellent prediction of the force-displacement curve for the experimental result.

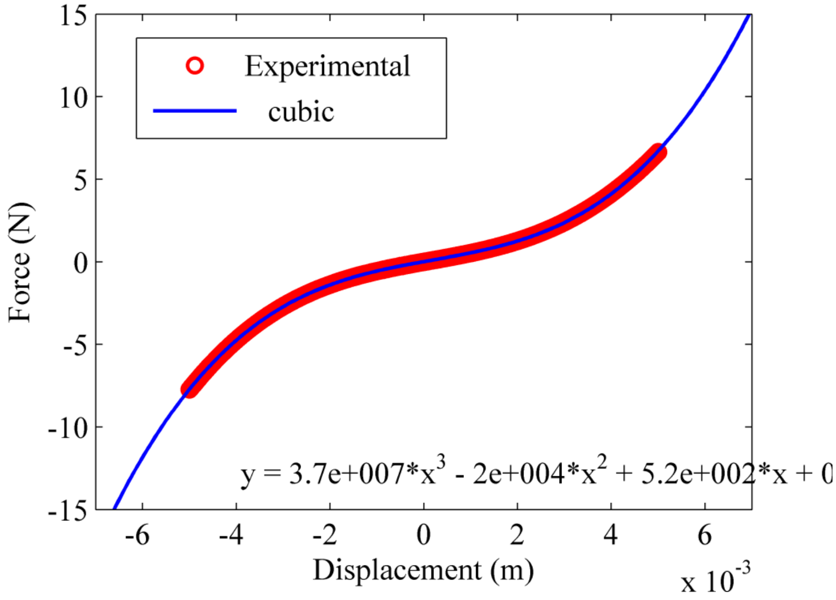

Figure 3.6: Cubic fit of the experimental test for half the cubic spring.

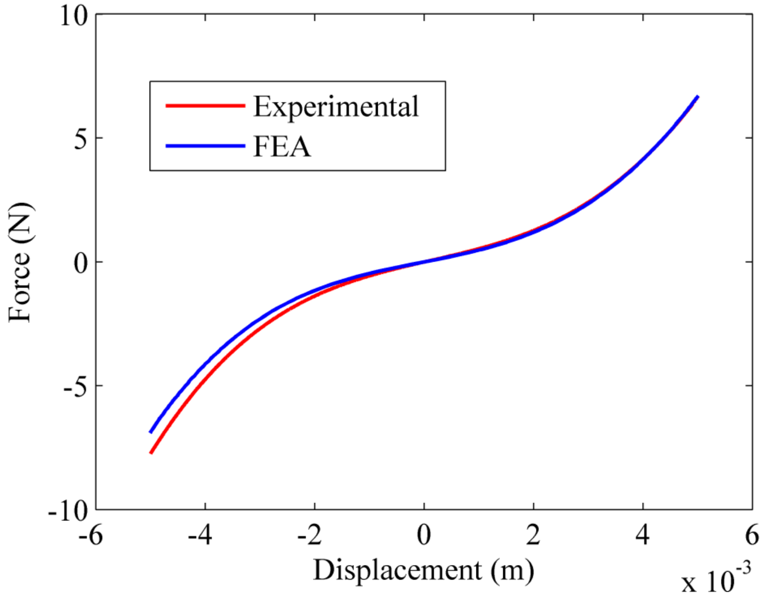

Figure 3.7: Comparison of the experimental and finite element analysis for the nonlinear spring design.

One of the issues with investigating only half of the spring is how the boundary conditions change from half spring to full spring design, which is not accounted for via the springs in series relationship discussion shown earlier. In the experimental test rig setup, Figure 3.8, the upper clamp represents the location that the displacement was applied, while the lower clamp represents the fixed boundary condition and where the force was measured. Unfortunately, due to equipment limitations the whole spring could not be tested.

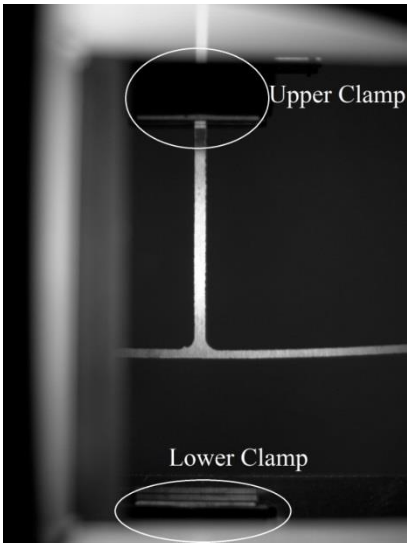

Figure 3.8: Experimental test setup showing the boundary clamping conditions.

The experimental and FEA results confirm that the developed spring design is very close to an essentially-nonlinear spring, but there is still a linear spring component that would be difficult to eliminate entirely. A simple set of simulations was conducted to determine the effect of the linear portion of the spring function on the isolation performance of the mount. The system chosen for the numerical investigation consisted of 9 masses, N=9, and a total mass of 21kg with impulsive excitation such that displacement differences between masses were around 5mm (v_i=0.45*1/m_1).

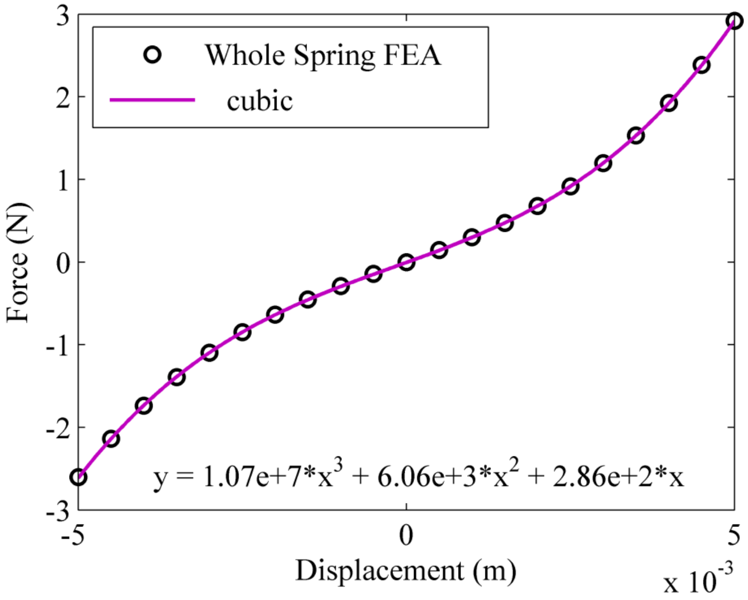

Figure 3.9: Finite element analysis on the whole spring design.

The linear and cubic portions of the spring force were obtained from the full spring finite element analysis (Figure 3.9). Figure 3.10 shows the transmitted wall force as a function of mass ratio, ε. The red curve shows the wall force obtained using just the cubic portion of the spring law; the black curve shows the wall force obtained using the full curve-fit relation (including linear and quadratic terms). It is seen that the transmitted force generated using the full curve fit displays a minimum around the same value of ε as observed for the purely cubic spring. This is very reassuring; suggesting that the fabricated spring can be used in experimental studies, and would be able to exhibit the resonance conditions captured in experiments based on Hertzian contact. It is interesting to note that the wall-force curve generated using the full curve fit has lower transmitted force than the purely cubic case for lower values of mass ratio. Comparing the maximum (ε =1) to the minimum for each curve, for the cubic chain's minimum is approximately 56% smaller at ε =0.46, whereas the finite element analysis curve-fit result is 41% smaller at its minimum of ε =0.4. While a direct comparison between the isolation levels is hard to accomplish due to the differing stiffness terms, Chapter 2 explains the trend towards somewhat better performance for small ε when compared to the performance of the system with the pure cubic spring.

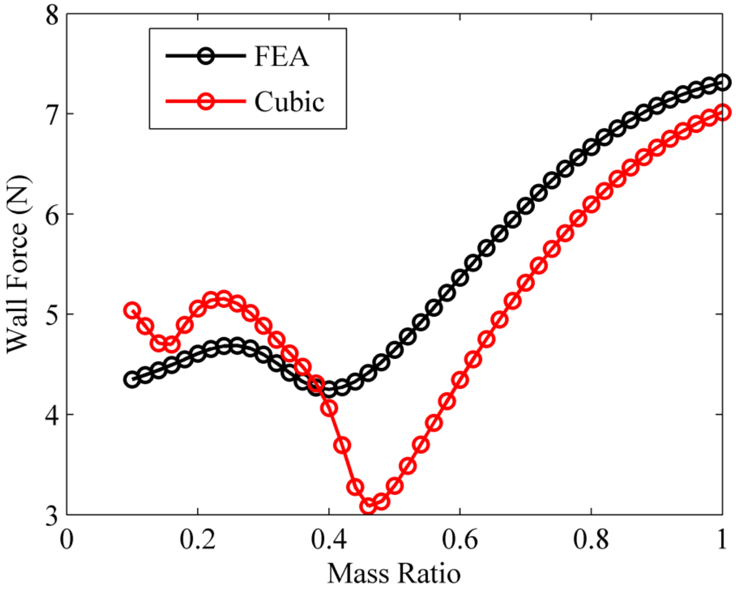

Figure 3.10: Comparison of FEA and cubic spring for N=9, M_{tot}=21kg and spring stiffness derived from half fit spring.

Another way of assessing the relative influence of the spring's linear portion to its cubic portion is to perform a parametric study varying the strength of the impulse load. Figure 3.11 shows the wall force as a function of both mass ratio and impulse strength. It can be seen that the low strength impulse largely keeps the system in its linear range, giving rise to a relatively smooth curves that do not display the 1:1 resonance dip. As the strength of the impulse increases, the dip at a mass ratio of ε =0.44 becomes more pronounced. The 1:2 resonance at ε =0.16 also becomes more noticeable at very high impulse strengths.

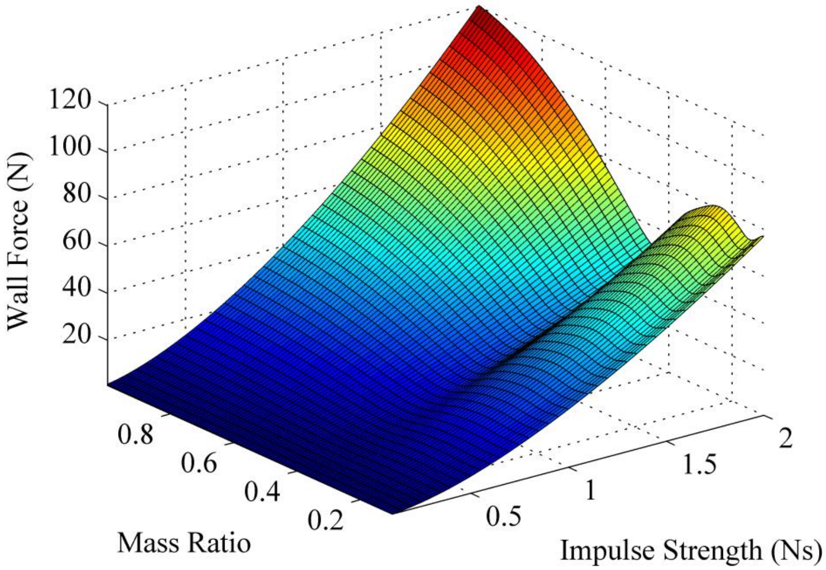

Figure 3.11: Wall force as a function of mass ratio and impulse strength for FEA fit.

3.4 Harmonic Experimental Analysis

Passive vibration absorbers, also known as dynamic vibration absorbers or tuned mass dampers, are among the most widely used classical vibration absorbers. An effective vibration absorber extracts energy from the primary structure. Therefore, an investigation into the practicality of using the aforementioned nonlinear spring as part of a nonlinear vibration absorber is analytically and experimentally investigated via a sinusoidal forcing sweep.

The experimental setup consists of an electrodynamic shaker, amplifier, two laser Doppler velocimeters (LDVs) and custom written LabVIEW National Instruments code using National Instruments hardware. A photograph of the experimental setup is shown below in Figure 3.12. The power amplifier used was a Brüel and Kjær type 2718, the electrodynamic shaker was a Brüel and Kjær vibration exciter type 4809, the LDVs were Polytec PDV-100 Portable Digital Vibrometers, the harmonic signal was generated through a NI9264 analog output, and signals from the PDVs were sent back to the computer through NI9234 analog inputs.

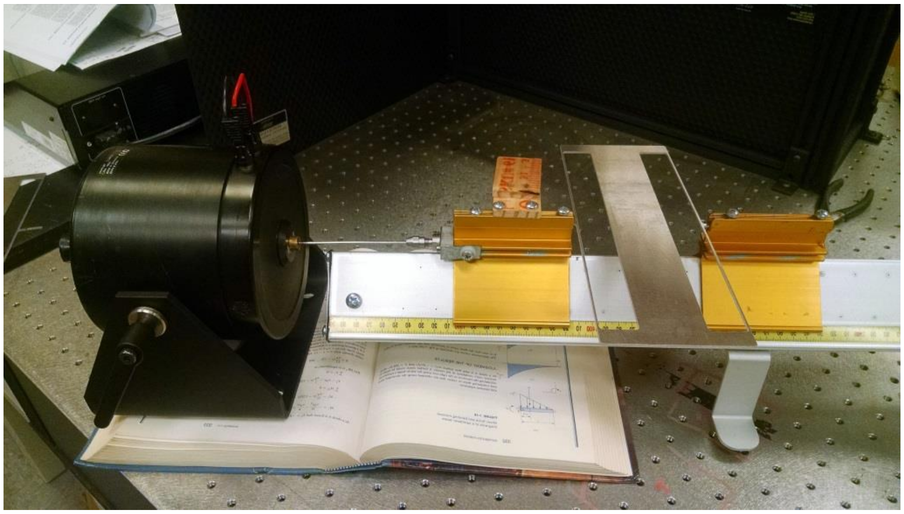

Figure 3.12: Experimental setup for the harmonic excitation of the nonlinear spring.

One of the difficulties in matching theoretical and experimental results for harmonic excitation is that the theory assumes a constant force amplitude over some frequency range. But during experiments, it is common to conduct sine sweeps with constant input voltage amplitude. Since an electrodynamic shaker delivers a force proportional to the *current* applied to its voice coil, the force amplitude may or may not be constant depending on the impedance of the electric circuit. In order to make sure that the current, and hence the applied force amplitude, were relatively constant over the frequency range of interest, the current applied to the shaker was monitored via a port on the backside of the Brüel and Kjær type 2718 power amplifier, which was connected to an oscilloscope. Through observation of the current applied to the shaker, it was found that the current amplitude was nearly independent of frequency which gives some confidence that the qualitative features of the experiment matched the conditions of the numerical simulations. Ultimately this resulted in a fixed magnitude applied force during the forward experimental sine sweep. A robust treatment of electrodynamic shakers is given by Lang and Snyder [48]. It should be added that a force transducer could also be used to monitor the applied force amplitude, but such a sensor was not available during testing.

The electrodynamic shaker can be treated as a single degree of freedom linear system, which yields the system shown in Figure 3.13. The system properties are:

Table 3.1: System properties for experimental harmonic excitation of two degree-of-freedom nonlinear spring.

m_1	0.2167 kg
m_2	0.1567 kg
K_{linear}	$1.2e^4$ N/m
$f(x)$	Figure 3.9
c_1	14.1 Ns/m
c_2	$1e^{-6}$ Ns/m

where m_1 is the combination of the moving mass element in the electrodynamic shaker (60g), the gold sliding mass (130g), one third of the mass of the nonlinear spring (16.67g), and 10g for the ruler pieces and screws. The second mass, m_2, is the same as the first mass, m_1, without the 60g from the moving mass element of the electrodynamic shaker. The linear stiffness component is derived from the shaker equipment manual and the nonlinear "stiffness" term is based on the curve fit in Figure 3.9. The damping parameter, c_1, was found by plucking the shaker and computing the result via log decrement.

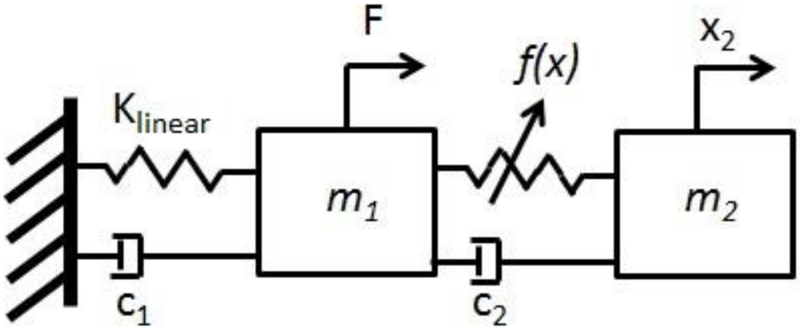

Figure 3.13: Schematic of experimental apparatus for harmonic excitation of nonlinear spring.

The equations of motion for the system described in Figure 3.13 are:

$$m_1\ddot{x}_1 = -K_{linear}x_1 - c_1\dot{x}_1 - f(x_1 - x_2) - c_2(\dot{x}_1 - \dot{x}_2) + F$$

$$m_2\ddot{x}_2 = f(x_1 - x_2) + c_2(\dot{x}_1 - \dot{x}_2) \qquad (3.14)$$

where $f(\Delta x)$ represent the nonlinear force displacement relationship from Figure 3.9 and the system properties are from Table 3.1. An underlying assumption is that the stiffness of the stinger is large, thus the stiffness internal to the electrodynamic shaker is what dictates the relationship (springs in series). Furthermore, some of the electrodynamic behavior of the shaker has been simplified, such as the back electromotive force, or back EMF.

Equation (3.14) was investigated with an analytical approximation known as the harmonic balance method [43]. The harmonic balance method has previously been applied to linear and nonlinear systems to approximate the steady-state response to periodic excitation. Unlike time integration techniques, such as Matlab's ode45, the harmonic balance technique does not involve the transient response. In nonlinear systems, the exact solution is generally composed of an infinite set of frequencies. However, in practice the amplitude of the higher harmonic will be substantially lower than that of the fundamental frequency. Hence, it is justifiable to include only a finite number of harmonics in the analysis. Due to the nature of the nonlinearity in question, a third-order harmonic balance solution was chosen of the form:

$$x_{r,approx} = a_{r,o} + \sum_{n=1}^{3} a_{r,n} \sin(n\omega t) + b_{r,n} \cos(n\omega t); r = 1,2 \qquad (3.15)$$

where $x_{r,approx}$ is the approximation to the displacement of mass r, which consists of the fundamental excitation frequency and the second and third harmonics. The accuracy of the harmonic balance method has been investigated by Ferri and Leamy [49]. Convergence studies were conducted that included higher harmonics (fourth harmonic and higher) which resulted in no improvement in the results.

Figure 3.14 shows the result for the velocity amplitude of the second mass obtained from a slow forward frequency sweep of the driving frequency comparing the harmonic balance method and the experimental results. Both the experiment and the harmonic balance method predict a large jump in the response of the second mass as the frequency is swept. There is excellent qualitative agreement between the two results, but there is a slight difference in the frequency at which the maximum occurs. This is most likely due to the aforementioned assumptions made in the modeling process. Attempts to reconcile the two resonance frequencies, such as slightly adjusting the shaker mass and stiffness, did not show significant improvement.

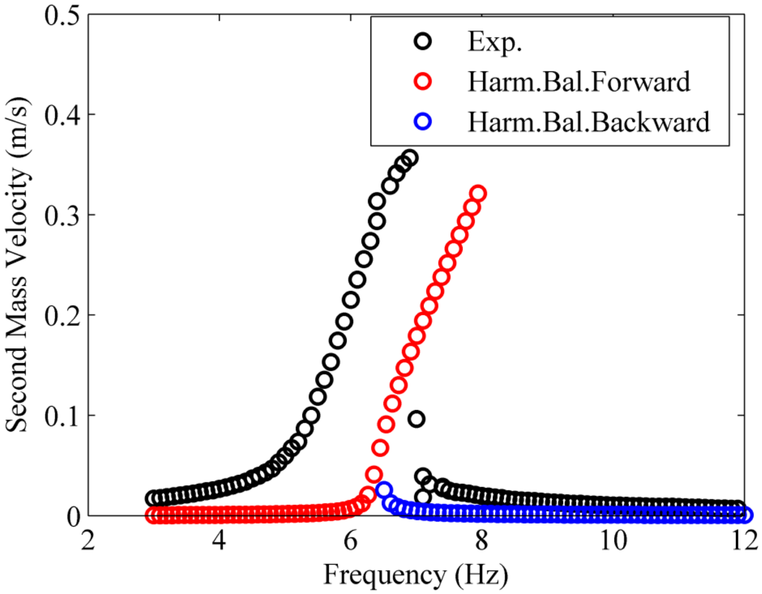

Figure 3.14: Comparison of harmonic balance and experimental results for two degree-of-freedom system.

3.5 Shock Experimentation

The shock experiment was performed on a 6 mass system with essentially cubic springs between them. A final 7th mass was clamped down, allowing it to be treated as the “wall” in the isolation system. Similar hardware to what was mentioned before was utilized; however, instead of LDVs measuring the response of the masses to the excitation, ICP accelerometers (PCB model number 352C65) were used to investigate the response of each mass and an ICP force transducer (PCB model number 208C02) was used to monitor the “wall” force. The experimental setup is shown in Figure 3.15.

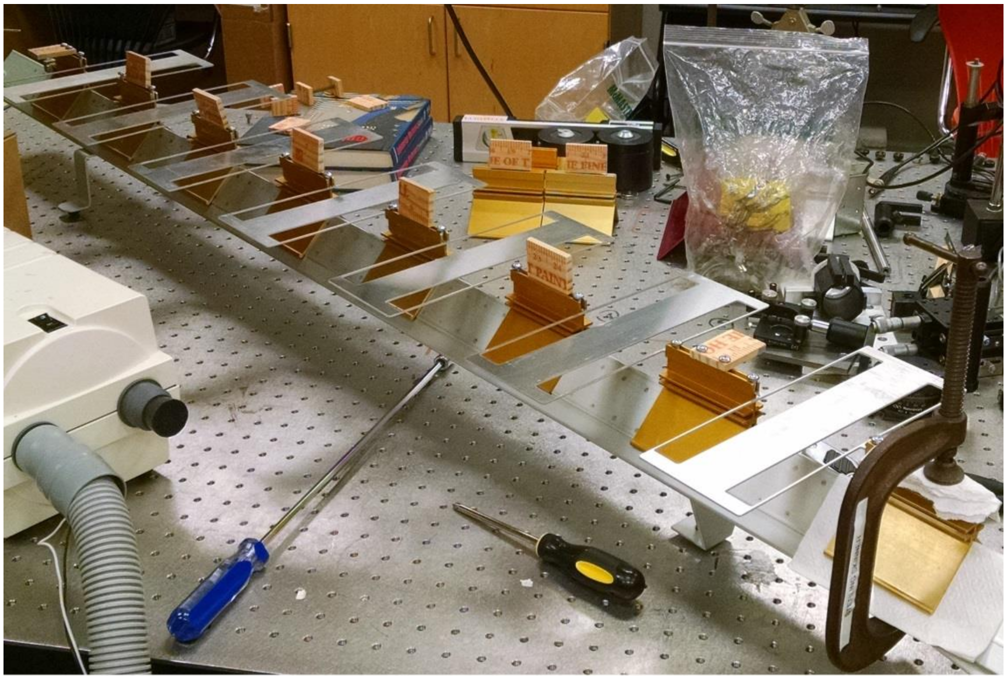

Figure 3.15: Experimental shock system setup with seven masses and essentially nonlinear springs.

One of the difficulties in the shock excitation of the experimental setup was the lack of ability to provide a pure impulsive load, such as that used in the theoretical and numerical studies presented in Chapter 2. An attempt to produce such an excitation is shown below in Figure 3.16. A light tap, via a hammer, was applied to the first mass, which resulted in an approximate instantaneous change in the first mass' velocity. However, the lack of energy supplied into the system during this short burst, does not significantly move the secondary mass in the chain.

The most likely reasons for the lack of disturbance propagation is that the energy is dissipated by the damping to ground provided by the air track and that the small movement of the first mass may have moved in a rotational or side to side motion along the air track. It is also possible that a small amount of spring flexure occurred out of the translational plane of the spring. Consequently, the impulsive loading via a hammer strike

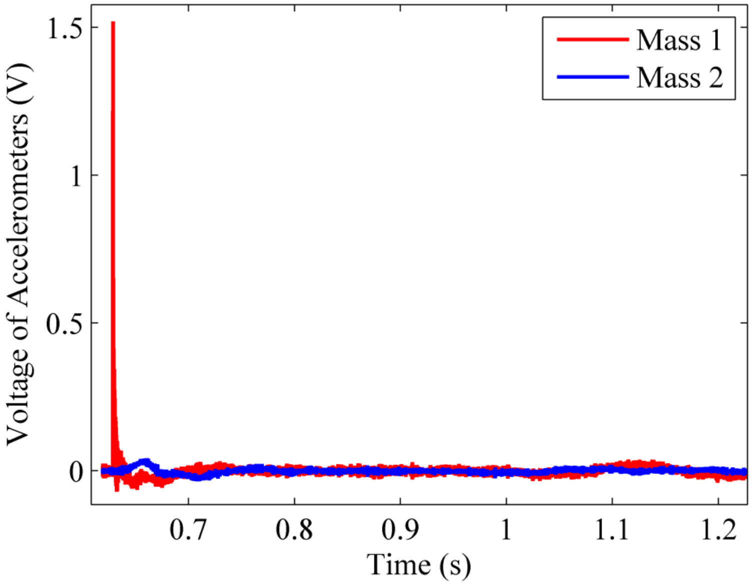

Figure 3.16: An impulsive load applied to the first mass that does not transmit to the second mass.

was not successful. Instead, a short duration “push” was applied to the first mass. In the numerical simulations below, this short duration pulse was still modeled as an instantaneous change in the velocity of the first mass. (The effect of using a more-realistic half sine input is considered in Chapter 7)The velocity chosen was adjusted such that the force transmission between the experimental and numerical simulation data matched. Finally, test data was shifted such that the first peak force transmissions aligned.

The data was sampled at 51.2 kHz, which was chosen to maximize the ability to capture sudden changes in the system response as the wall force underwent changes. The raw data was filtered via a moving-average filter of twenty samples (0.39 ms), which was used to smooth the data without distorting the measurements. Mathematically a moving average filter is a type of convolution, thus it can be viewed as a low-pass digital filter of the form:

$$y_{filter} = \frac{1}{20} * \begin{bmatrix} x(n) + x(n-1) + x(n-2) + \cdots \\ +x(n-18) + x(n-19) \end{bmatrix}, n = 20 \tag{3.16}$$

The raw and filtered experimental force data are shown in Figure 3.17, which shows that the moving average filter does a good job improving the signal to noise ratio.

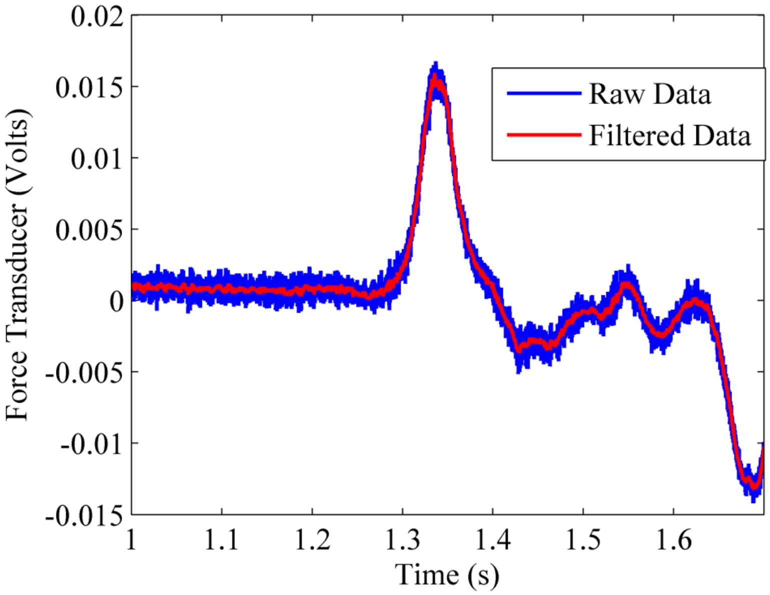

Figure 3.17: Twenty term moving average filter applied to raw force transducer data.

While every effort was made to keep the total mass of the isolation chain constant, experimental limitations made this very difficult to accomplish. Therefore, two different shock excitation experiments were conducted. In Case 1, the golden masses shown in Figure 3.15 were used to represent masses m_1, m_2, …m_6. In Case 2, playdough has been added to the even-numbered golden masses, m_2, m_4, m_6, which resulted in a mass ratio of around $\varepsilon = 0.45$; i.e., the theoretically predicted condition of the 1:1 resonance. Experimental results were compared to numerical simulations. The numerical simulations assumed only a small amount of damping to ground, which is induced due to the golden masses sliding over an air track. Case 1, where all the masses are equal, is shown in Figure 3.18 and Case 2 is shown in Figure 3.19 where the mass ratio is 0.45. Due to the adjustments in the first mass velocity, we see a strong correlation in the magnitude of the first peaks. The fact that the curves have a similar shape is interesting because the experimental system utilized a “push” input, whereas the numerical simulation used an instantaneous change in the velocity of the first mass. However, as time evolves, it is shown that the numerical simulation begins to predict peak values before they occur in the experiment. It is suspected this is a consequence of the spring mass, the minor tension or compression applied during spring attachment to the masses, and manufacturing differences in the springs.

3.6 Conclusion

The creation of an essentially nonlinear spring was explored in this chapter. Similar to the idea of an un-tensioned fixed-fixed string, the design was based on resisting transverse forces primarily through the action of membrane forces. The resulting design utilized very thin members to approximate the behavior of a string, but in a way that was easily fabricated out of a single sheet of aluminum.

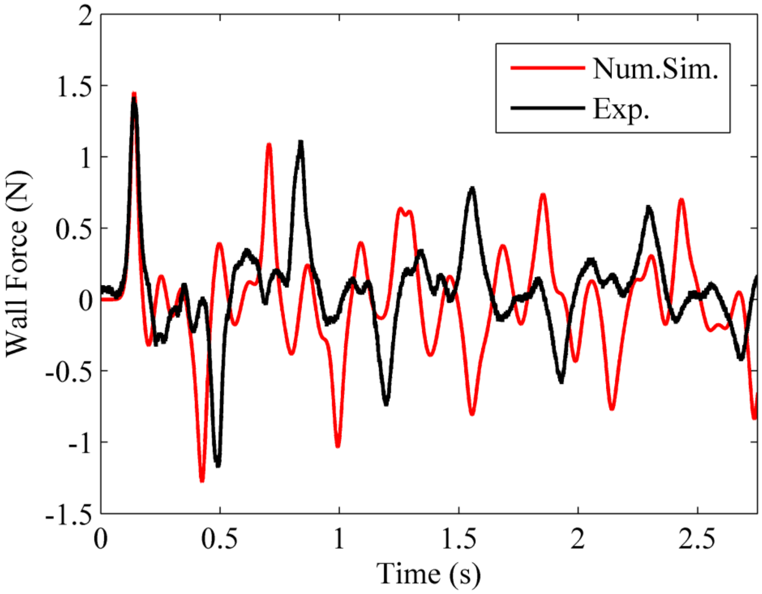

Figure 3.18: Wall force versus time for experimental and numerical simulation of a shock event in a 6 mass system a mass ratio of 1.

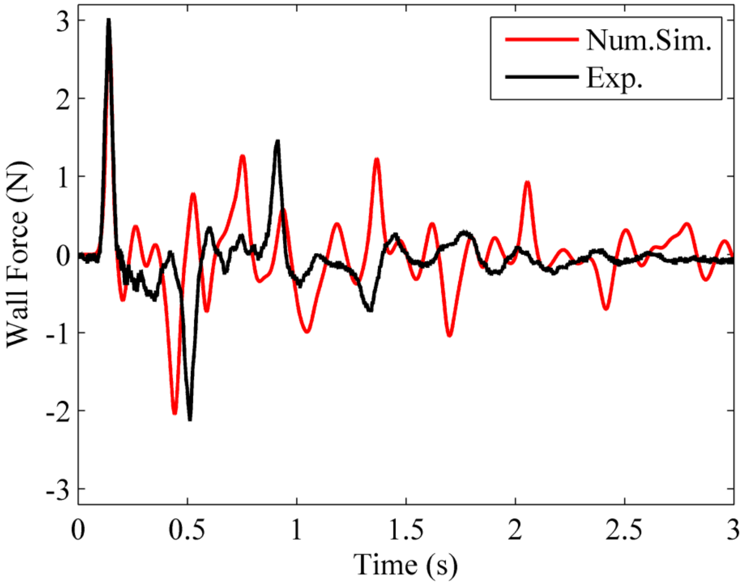

Figure 3.19: Wall force versus time for experimental and numerical simulation of a shock event in a 6 mass system with a mass ratio of 0.45.

It was found through a Rayleigh-Ritz approximation that a clamped-clamped beam with a transverse deflection at midspan would yield the desired nonlinear behavior. The relationship governing the coefficient of the linear and nonlinear spring term was primarily dictated by the thickness of the beam. As the beam thickness decreased, the force-displacement relationship would become more nonlinear. The verification of this nonlinear behavior was performed via finite element analysis using ANSYS and found to compare extremely well to the results from static experiments. While the spring still exhibited some linear component, its behavior was found to be noticeably nonlinear for deflections between 2 mm and 5 mm; at least 70% of the spring force was cubic in nature for deflections of 5 mm and higher.

The nonlinear spring was then tested via a sinusoidal frequency sweep, similar to a nonlinear vibration absorber. It was shown that the experimental response was closely predicted by a harmonic balance method applied to the equations of motion. The small difference in the resonant frequency could be attributed to the assumptions in simplifying the shaker dynamics down to a SDOF system and the redistribution of the spring's mass into the adjacent lumped masses.

Unfortunately, an attempt to experimentally validate the shock response of the nonlinear dimer chain was only partially successful. For a six mass chain, two different values of mass ratio were investigated – $\varepsilon=1$ and $\varepsilon=0.45$. However, since the smaller mass ratio was achieved through *addition of mass* to alternating masses, the total mass of the two isolation chains was not equal. It was shown that the experimental results for the wall force correlated well with the numerical simulations. The biggest observed difference was that the secondary force peaks that corresponded to reflected waves arrived somewhat later in time in the experiment when compared to the simulation. It is speculated that this might be due to minor differences in the spring's shape when manufactured and/or due to the amount of pre-tension or pre-compression in the springs that occurred when attaching them to the adjacent masses. Experience gained in designing and conducting these experiments is essential in being able to suggest new experiments for future work.

CHAPTER 4.

ISOLATION MOUNTS BASED ON CHAINS OF MASSES WITH SMALL ROTATIONS

4.1 Overview

This chapter extends the work performed in Chapter 2 by introducing small rotational motion into the chain of masses previously considered. Because the masses are only allowed to rotate through small angles, the governing equations are linear. The basic concept is to convert some of the harmful translational motion into non-harmful rotational movement. The chapter begins with a description of the system and the derivation of the linear equations of motion. Similar to the analysis of the linear chains in Chapter 2, upper bounds on the transmitted force are obtained using a modal superposition approach. Through numerical simulation, the behavior and performance of the isolation system are studied as the stiffness, mass ratios, and mass moments of inertia are varied. Tradeoffs between the transmitted wall force and the first mass displacement are studied. Additional details and results may be found in [50].

4.2 Isolation System Model

Figure 4.1 shows the system under consideration, consisting of an initial mass followed by N-1 2DOF masses. The first mass is present for two reasons. First, it provides a convenient “attachment point” for the application of the initial impulsive load. Second, when it is attached away from the centerline of the system, it acts to break up the symmetry of the system. This symmetry breaking phenomena prevents the system from having purely translational and purely rotational modes. Depending on the location or offset of the attachment mass, h_{off}, and size of the attachment mass relative to the rest of the system mass will determine the level of symmetry breaking. The 2DOF masses are idealized by long slender rods of length 2*L* and mass, m_i. However, the rods are considered to have non-uniform mass distribution, which effectively uncouples the mass from the mass moment of inertia, J_i. Thus, in this study, m_i and J_i are treated as independent variables; an alternate choice would be to consider the mass and the radius of gyration as independent variables, which would accomplish the same degree of variability. The masses are restrained by 2N-1 identical springs, where *N* represents the number of masses in the system. Note that, other than the offset first mass, the system shown in Figure 4.1 is symmetric about the centerline; this assumption is relaxed in a later chapter when optimization studies are conducted. Low damping is assumed in the form of linear viscous dampers that are co-located with the spring elements. Motivation for maintaining low damping levels is that linear (viscous) damping is known to be detrimental to high-frequency shock isolation [7].

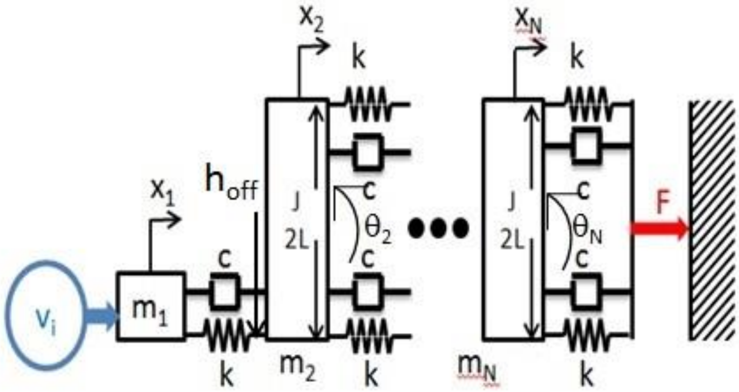

Figure 4.1: Translational and rotational isolation mount.

The input to the system is taken to be an impulsive load applied to the first mass; mathematically, this amounts to an instantaneous change in the first mass' initial velocity. Thus, the impulse response of the system is the free response with all displacements and velocities equal to zero except for the first mass' initial velocity given by: $\dot{x}_1(0) = v_1 = \sqrt{\frac{2E}{m_1}}$, where E is the desired initial energy into the system and m_1 is the mass of the first mass. The mass ratio of adjacent masses is defined as $\varepsilon = m_3/m_2 = m_5/m_4 = \ldots$ Furthermore, the first mass is set to a constant value of 1kg, unless otherwise noted. Using a small angle assumption: $\sin\theta \sim \theta$, the equations of motion can be simplified into linear, second-order differential equations of motion in the form:

$$[M]\{\ddot{\varphi}\} + [C]\{\dot{\varphi}\} + [K]\{\varphi\} = \{0\} \tag{4.1}$$

where:

$$\{\varphi\} = \{x_1, x_2, \theta_2, x_3, \theta_3, \dots, x_N, \theta_N\} \tag{4.2}$$

Proportional damping is assumed, which was described in equation (2.8).

A key feature of the system shown in Figure 4.1 is that the net wall force does not depend on the rotation of the last mass. The rotation, θ_N, causes an increase in the extension of the upper spring while causing a decrease in the extension of the lower spring by the exact same amount. Since the upper and lower springs are identical, the net wall force depends only on x_N:

$$F_{wall} = 2kx_N \tag{4.3}$$

This fact allows the rotational motion of the chain to uncouple from the wall force to some extent. The uncoupling gets more and more complete as the first mass gets smaller in size relative to the other 2DOF masses. In the limit as m_1 goes to zero, the translational and rotational modes completely uncouple.

Similar to the work done in Chapter 2, the overall mass and stiffness of the system are held constant as attachment mass location, h_{off}, and mount length, N, are varied. As before, the stiffness of the individual springs must be selected such that a unit force applied to the first mass results in a prescribed static deflection, Δ_s. The required value of the individual spring constants can be derived in a closed form, as a function of Δ_s, N, and h_{off}:

$$k = \frac{(N-1)*h_{off}^2+(N+1)L^2}{2*\Delta_s*L^2} \tag{4.4}$$

For consistency with the systems considered in Chapter 2, the overall mass of the system, unless otherwise stated, is maintained to be 21kg. The overall static stiffness is maintained to be 200 N/m.

Finally, the performance objectives of critical interest are the wall force, F_{wall}, and the first mass displacement, x_1.

4.3 Theoretical Predictions and Upper Bounds

The theoretical expectations and upper bounds for the linear system of Figure 4.1 are derived in a manner similar to that described in Section 2.3. The central hypothesis is that a lightly damped system will have a response comprised of contributions from all of its modes. A worst case scenario for the wall force occurs when the contributions from every mode add in phase at some time instant. The reader is referred to that section of the thesis for an overview on building the theoretical expectations.

Figure 4.2 shows the wall force for a ten-mass chain obtained through numerical simulation vs the mass ratio for the rotational mass elements. Also shown is the upper bound on the wall force, indicated with dashed lines. It is seen that the upper bound on the wall force does safely bound the numerically calculated wall force for simulations lasting 300 cycles of the lowest natural frequency sampled at approximately 10 times the highest natural frequency. The curves labeled as "theory" are based on the equation:

$$F_{max} = 2k \sum_{j=1}^{N} \frac{|\Phi_{1,j}||\Phi_{2*N-2,j}|}{\omega_j} \tag{4.5}$$

where $\Phi_{2*N\text{-}2,j}$ represents the translational displacement of the final mass, x_N, in the j^{th} mode. Note that the simulation results are quite erratic due to the fact that small changes in the mass ratio can lead to the coalescence of modal contributions, or the discouragement of coalescence in the time window of the simulation. This is similar in nature to the phenomenon observed for dimer chains in Chapter 2. The degree of variation depends on the amount of damping in the system and on the time window as previously discussed. In addition to validating the theoretical upper bound, Figure 4.2 also demonstrates the influence of mass rotation on the wall force. For small values of the mass ratio, the no rotation case outperforms the case with rotation; however, for larger values of mass ratio that trend is switched. However, this was just for a specific value of mass moment of inertia and input energy: J=1e^{-3} kgm^2 and E=0.5 Nm.

Figure 4.3 shows the influence of mass moment of inertia as the mass ratio is held fixed. As the value of the mass moment of inertia increases the system exhibits less and less rotation, acting more and more like a translational chain of masses. Note that between mass moments of inertia of 10^{-2} and 10^{-1} kgm^2, there is an interesting dip predicted by both the theory and the numerical simulation. Thus, it is interesting to note that there may exist a certain combination of mass ratios and mass moments of inertia that provides a reduction in the transmitted wall force.

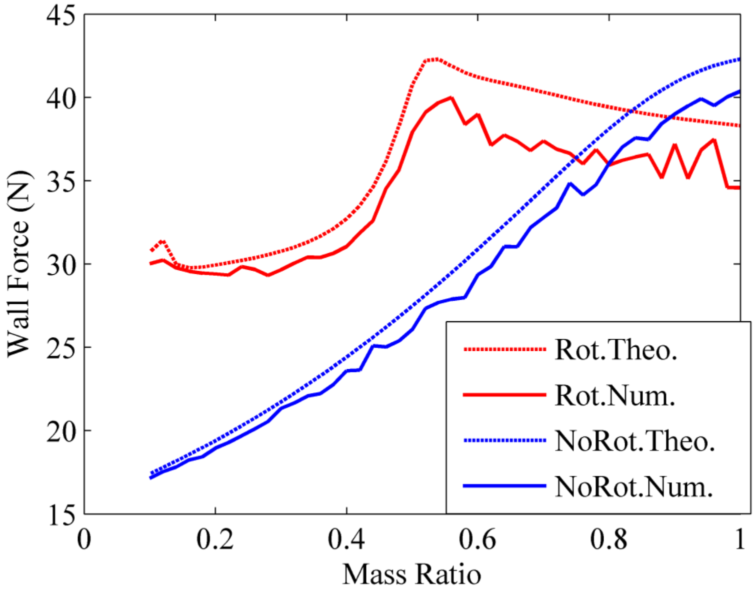

Figure 4.2: Wall force versus mass ratio for undamped ten mass system with comparison of numerical simulations and theoretical upper bounds.

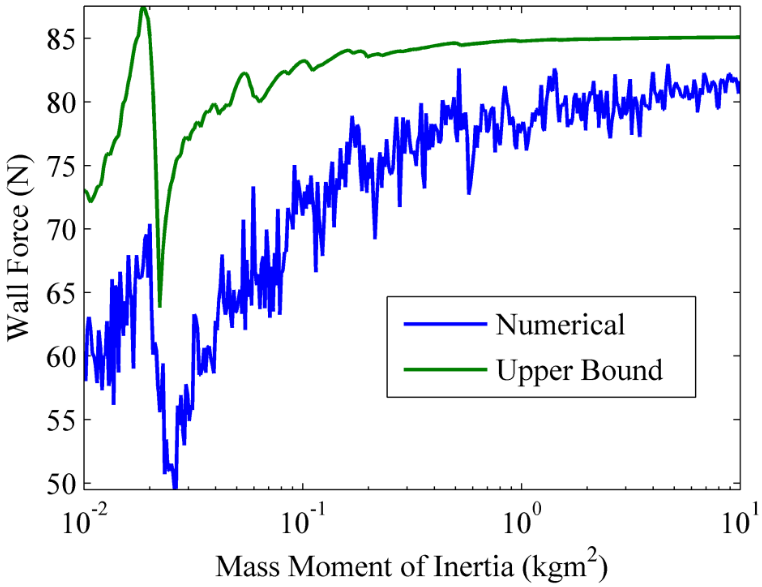

Figure 4.3: Wall force versus mass moment of inertia for undamped 10 mass system with comparison of numerical simulation and theoretical upper bound.

4.4 Initial Energy Input Influence

In the case of a truly linear system, as the level of input energy imparted to the system is increased, the magnitude of the response scales proportionately. However, the system under investigation shown in Figure 4.1 is not truly linear; instead, it is assumed to be linear as long as the small angle approximation holds. The amount of error introduced by the small angle approximation is plotted in Figure 4.4. The rate at which the relative error changes with change in angle increases rapidly. However, up until about 24^o the amount of error introduced is less than 3%.

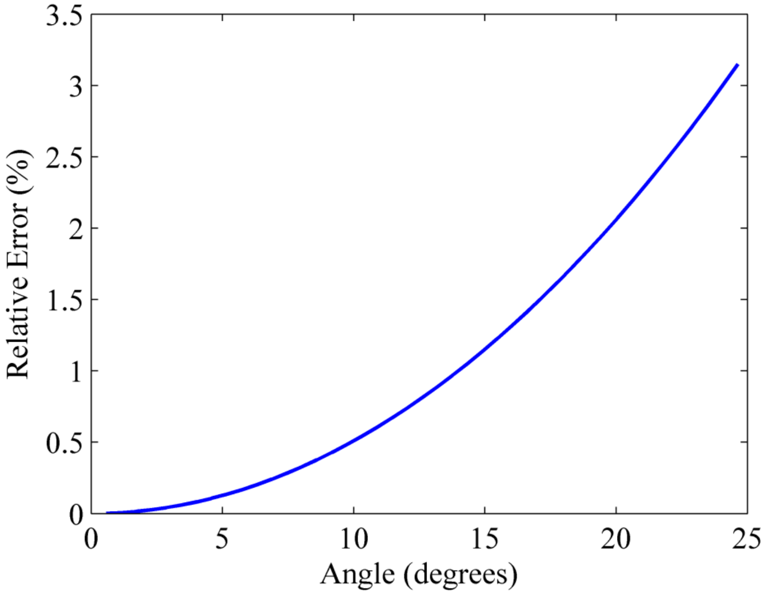

Figure 4.4: Relative percent error due to the small angle approximation.

As the mass moment of inertia is decreased in the system, in general the system will exhibit larger angular movement. Consequently, if that angular displacement becomes too large, the system is no longer linear due to a violation in the small angle approximation – increasing levels of error between the linear assumption and actual sinusoidal value. Therefore, an investigation was conducted into the acceptable input energy levels for a range of mass moments of inertia, such that the small angle approximation is not violated. The results of this study are shown in Figure 4.5-Figure 4.7. The number of masses in the system is six (one purely translational mass and five rotational/translational masses). The total mass of the system is 21 kg, the magnitude of the translational mass is 1kg. The energy input is performed at three different levels of energy: low energy (0.5 Nm), medium energy (1 Nm), and high energy (3 Nm). It is worth noting that changes in the static stiffness constraint will influence the acceptable range of mass moments of inertia, similar to the energy influence shown.

In the case of high energy levels, allowing as much rotation as possible provides the smallest transmitted wall force both numerically and theoretically. However, in the case of medium and low energy excitation, there exists a specific range of mass moments of inertia that minimize the transmitted wall force. The first mass displacement, shown in Figure 4.8, follows a much simpler pattern. For all three energy input values, as the mass moment of inertia is decreased, the magnitude of the first mass displacement is increased. Depending on the desires of the mount: force isolation, stroke minimization, or a combination of the two becomes important in the selection of the mass moment of inertia.

The reason for the unique structure in the transmitted wall force plots, that is to say the existence of a specific mass moment of inertia that reduces the transmitted wall force, is investigated in the next section. This specific location is exhibited in both the theoretical results and the numerical simulation. Thus, to obtain a better understand of the phenomena at work, a simpler system will be studied that helps to explain the results.

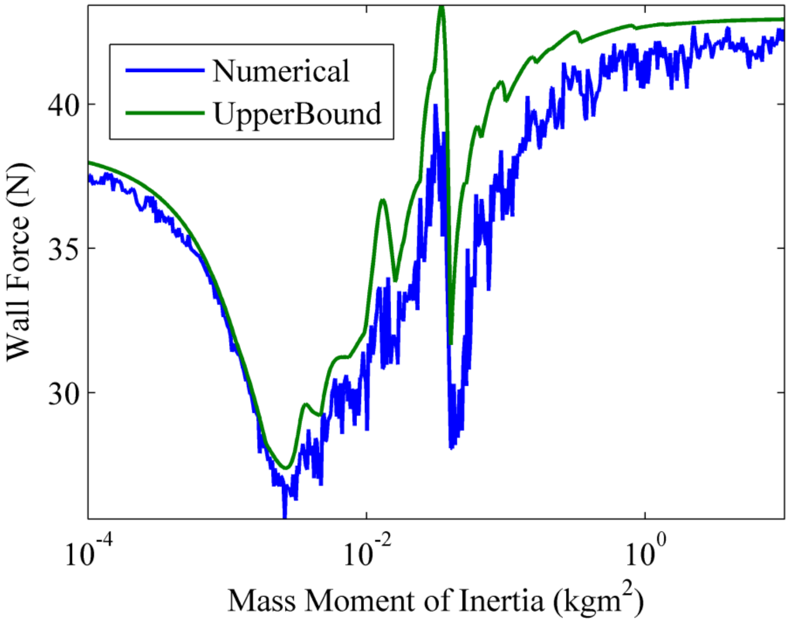

Figure 4.5: Transmitted wall force for input energy of 0.5 Nm.

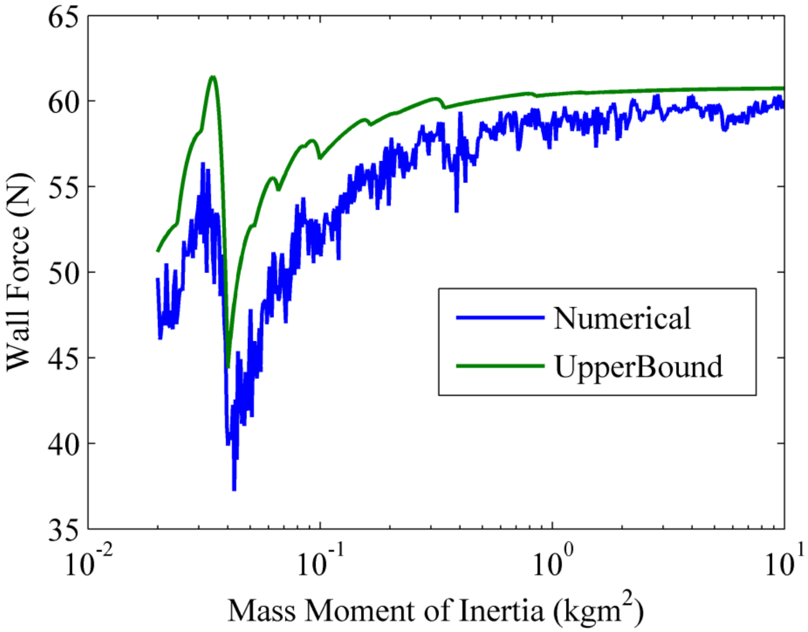

Figure 4.6: Transmitted wall force for input energy of 1.0 Nm.

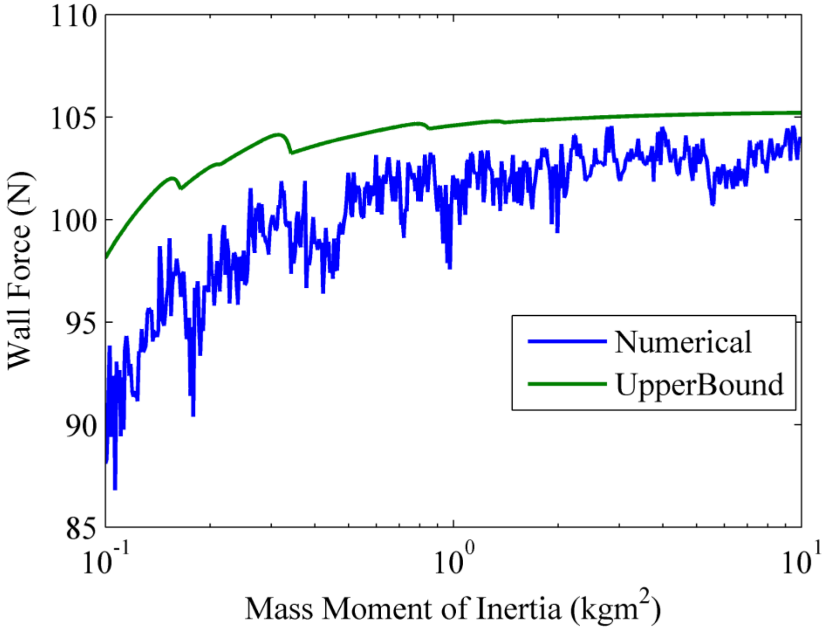

Figure 4.7: Transmitted wall force for input energy of 3.0 Nm.

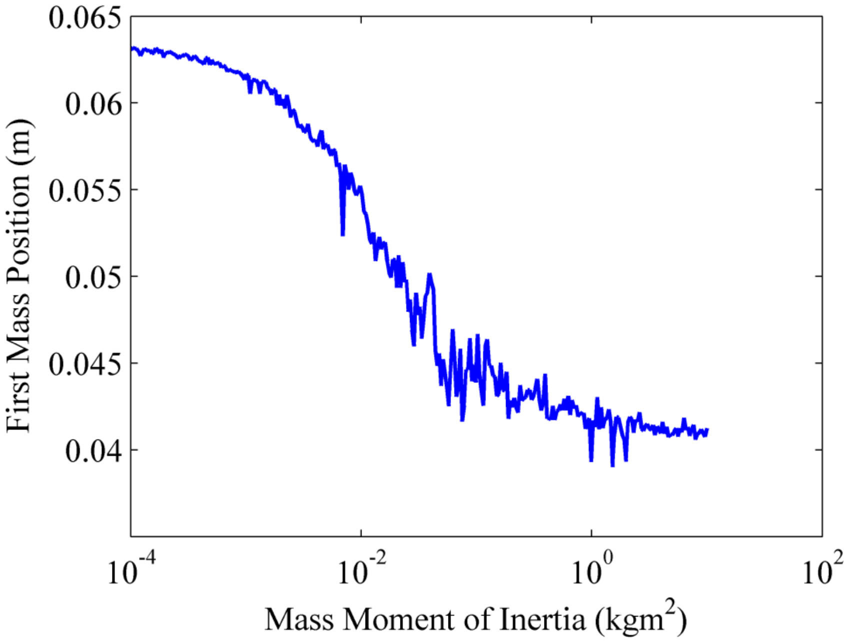

Figure 4.8: First mass displacement for input energy of 0.5 Nm.

4.5 Simplified Two Mass, Three Degree-of-Freedom System

The results above considered long chains which accentuate the wave-transmission attributes of the isolation mount. But, due to the high order of the system, it is difficult to uncover any fundamental insights into the isolation behavior of the mount. To simplify the system as much as possible, a system is considered that consists of one translating mass and one translating and rotating mass. The total mass of the system is 1kg, static stiffness of 200 N/m, and the input into the system is an instantaneous change in the velocity of the first mass. Two parameters are investigated to see their influence on the dip in the wall force; those two parameters are the offset location of the first mass, h_{off}, and the magnitude of the first mass, m_1, relative to the second mass.

Figure 4.9 and Figure 4.10 display the results of numerical simulations as the magnitude of the first mass is increased. The offset location, h_{off}, is 0.1 m and the energy into the system is 0.8 Nm. As the mass moment of inertia is changed, the transmitted wall force curve changes; in particular, it exhibits various degrees in dip severity, depending on the magnitude of the first mass. As the magnitude of the first mass increases, the magnitude of the dip decreases. Also, the overall force level decreases as the first mass size decreases relative to the other mass. As the magnitude of the first mass is increased, the first mass displacement increases as shown in Figure 4.10. However, if one investigates m_1=0.25 kg, the dip in the wall force represents a 40% decrease across its domain; whereas the increase in the first mass displacement is only approximately 15%. Ultimately, this shows that if high isolation (low wall force) is the primary objective, it is possible to select a design corresponding to the dip in the force curve as an attractive parameter choice.

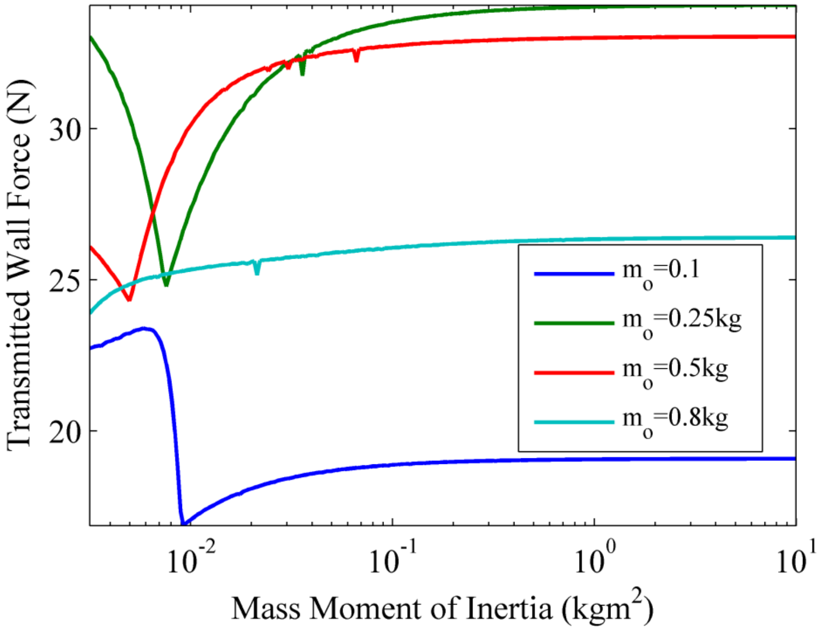

Figure 4.9: Influence of the magnitude of the first mass on wall force.

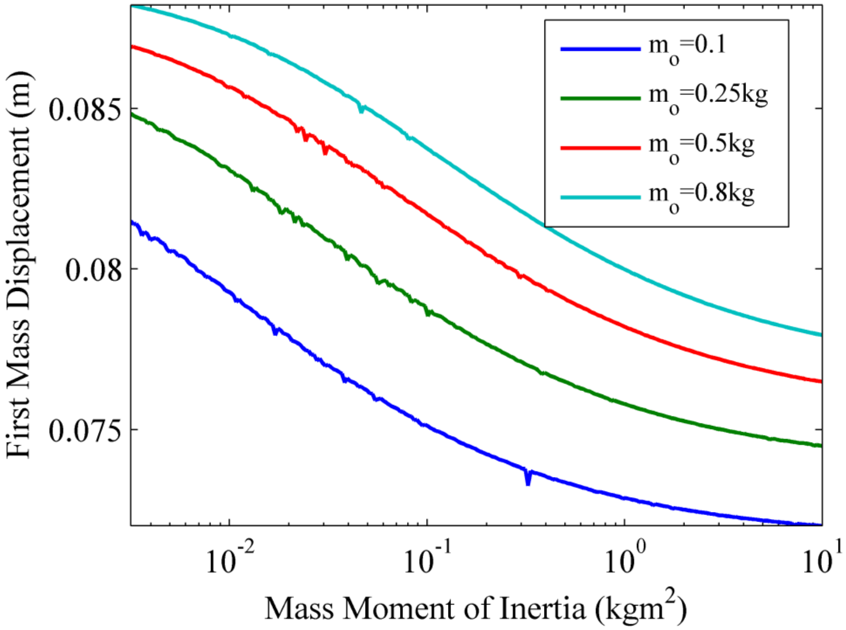

Figure 4.10: Influence of the magnitude of the first mass on first mass displacement.

The other parameter of interest in the two mass three degree-of-freedom system is the attachment location, h_{off}. The magnitude of the first mass is chosen to be 0.25 kg, and h_{off} is varied between 0 to 0.1 m, the half-length of the rotational mass. Shown in Figure 4.11 and Figure 4.12 is the transmitted wall force and the first mass displacement, respectively, as a function of the rotational inertia of the second mass for various values of h_{off}. For h_{off} = 0 m, both the transmitted wall force and first mass displacement are horizontal lines. This makes sense since, with h_{off} =0 m, there is no excitation to the rotational dynamics of the system. This results in the three degree-of-freedom system reducing to a two degree-of-freedom system (pure translational motion). However, as the offset attachment location is increased, certain mass moments of inertia result in larger transmitted force (in part due to the static stiffness constraint), while the characteristic dip in the wall force begins to emerge and become more significant. At the same time, the first mass displacement begins to become smaller and smaller as h_{off} increases. Again, this is in part due to the spring rates changing to account for the static stiffness constraint. Recall that this resulted in increased force in the linear purely translational systems studied in Chapter 2. The ability of the offset attachment location, h_{off} =0.1 m, to decrease the wall force (approximately 16% reduction when compared to the no rotational system), and to decrease the first mass displacement (approximately 2% when compared to the no rotational system), results in a superior mount. Improvement percentages were chosen at the same value of the mass moment of inertia: 7.564e^{-3} kgm^2.

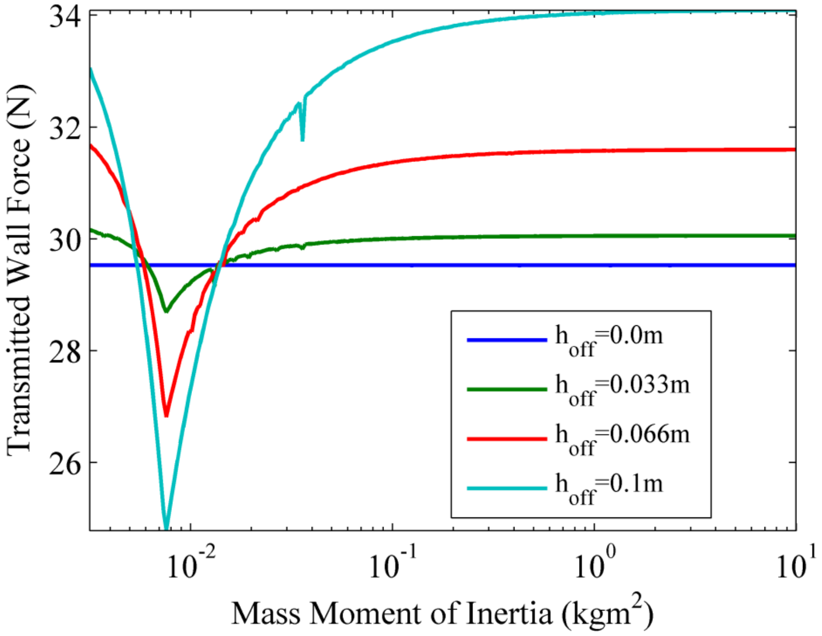

Figure 4.11: Influence of the offset attachment location on wall force.

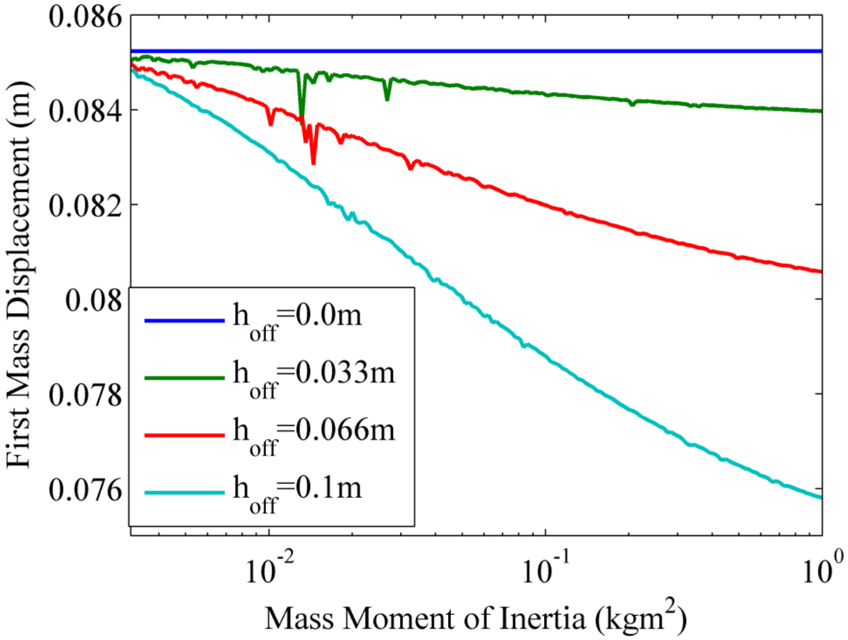

Figure 4.12: Influence of the offset attachment location on first mass displacement.

Since modifications to the mass matrix (m_1 and J adjustments) and stiffness matrix (h_{off} adjustment) result in significant changes to the transmitted wall force theory, it is hypothesized that the eigenstructure of the problem has a beneficial result for certain mass moments of inertia. Recall that the construction of the upper bound theoretical line was generated utilizing the mode shapes. Therefore, utilizing the theory presented in Section 2.3, the contribution of each mode to the wall force can be determined and normalized to see the level of contribution to the wall force.

Figure 4.13 shows the normalized contribution to the wall force from each mode. The offset attachment location is 0.1 m and the magnitude of the first mass is 0.25 kg. For small values of the mass moment of inertia, it is shown that mode 3 has little contribution. Mode 3 is primarily rotational, which does not contribute to the net wall force because the forces in the top and bottom springs cancel when the stiffnesses are equal. As the mass moment of inertia increases, the system will have less and less rotation, this results in the three degree-of-freedom system behaving more like a two degree-of-freedom system. During this sweep of increasing mass moments of inertia, an interesting lack of transmission to the wall force occurs for mode 2. In the event that the mass moment of inertia is equal to $7.564*10^{-3}$ kgm^2, mode 2 has approximately zero contribution to the wall force. For this to occur, it must be the case that either the system has been excited at a nodal location or that the final mass is purely rotating.

Table 4.1 gives the three mass-normalized modeshapes at the point where the wall force contribution from the second mode is at a minimum (J= $7.564*10^{-3}$ kgm^2).

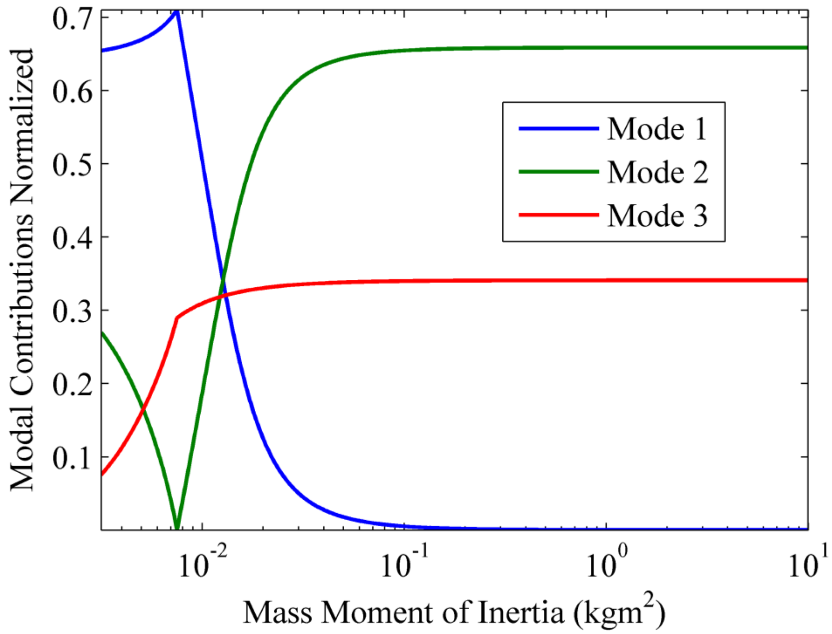

Figure 4.13: Normalized modal contributions to the wall force for a two mass, three degree-of-freedom system.

Table 4.1: Mode shapes for the two mass three degree-of-freedom system.

$\begin{Bmatrix} x_1 \\ x_2 \\ \theta_2 \end{Bmatrix} = \begin{Bmatrix} 1.5493 \\ 0.5165 \\ 5.1633 \end{Bmatrix}$	$\begin{Bmatrix} x_1 \\ x_2 \\ \theta_2 \end{Bmatrix} = \begin{Bmatrix} -0.0003 \\ 0.8165 \\ -8.1661 \end{Bmatrix}$	$\begin{Bmatrix} x_1 \\ x_2 \\ \theta_2 \end{Bmatrix} = \begin{Bmatrix} -1.2648 \\ 0.6324 \\ 6.3266 \end{Bmatrix}$
Mode 1	Mode 2	Mode 3

As shown in Table 4.1, there is a nodal location at the location of the first mass, x_1, for the 2nd mode. Since x_1 is the excitation point for the applied impulse, mode 2 has very little participation in the response. This behavior is further evident in Figure 4.14, which plots the transfer function from a harmonic force applied to mass 1 and measured at the translation of the 2nd mass. It is seen that the 2nd mode's peak, which should occur at a frequency of 32.66 rad/s, is almost completely absent from the frequency response curve. Therefore, this mount exhibits the best shock response when the 2nd mode has no contribution to the wall force.

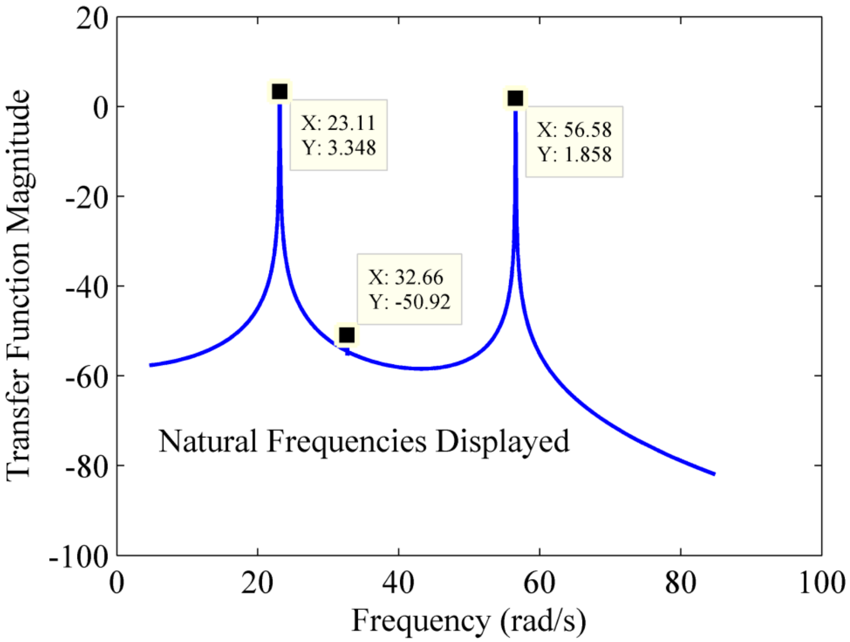

Figure 4.14: Transfer function for the two mass system relating the final mass translation to the first mass translation.

4.6 Determination of Ideal Mass Moment of Inertia Based on 2nd Mode Removal

Previous solutions have been numerically computed. However, at least for the simple two mass three degree-of-freedom system, the ability to compute the value of the mass moment of inertia that will remove the 2nd natural frequency from the transfer function, relating translation of both masses, can be determined. This process is similar to the inverse eigenvalue problem in vibrations and has strong resemblance to methods discussed in references [51]-[53]. To determine the ideal mass moment of inertia, we investigate the determinant of the dynamic absorption matrix:

$$h_{21} = |[K_{21}] - \omega^2 [M_{21}]| \tag{4.6}$$

where h_{21} is the dynamic absorption matrix for the harmonic response of the system at x_1 when excited with frequency ω at x_2, K_{21} and M_{21} are the stiffness and mass matrices with the 2nd row and 1st column removed; note that $h_{21} = h_{12}$ via reciprocity. To create the pole-zero cancellation shown in Figure 4.14, the dynamic absorption matrix must be equal to zero: $h_{21}=0$ and $\omega=\omega_2$. However, as the mass moment of inertia is adjusted, the natural frequency will change. For the case shown in Figure 4.14, it is required that

$$h_{21} = \begin{vmatrix} -400 & -40 \\ 40 & 12 - J\omega_2^2 \end{vmatrix} = 0, \qquad (4.7)$$

which yields:

$$J\omega_2^2 - 8 = 0 \qquad (4.8)$$

While equation (4.8) looks very simple to solve, it must be noted that ω_2 is the second natural frequency of the three degree-of-freedom system, which depends on J in a complicated way. Still, the requirement that the system possess a natural frequency at a particular value of ω_2 consistent with equation (4.8) allows a solution for J, although a closed form solution might not be easily obtainable. A plot of equation (4.8) is shown below as the mass moment of inertia is varied, Figure 4.15.

For this simple system, there is an alternate way of determining the desired value of the mass moment of inertia so as to place a nodal point at x_1. Essentially, this will always occur whenever the system consisting of only the second mass and its springs to ground has repeated roots. For such a system, the natural frequency of the translating mode is simply sqrt(2*k/m_2) = 32.6599 rad/s. Substituting this value of natural frequency into equation (4.8) yields J = 0.0075 kgm^2, which is very close to the location where the wall force was minimized. For more complicated multi-degree-of-freedom systems, the more systematic method of [52] is recommended.

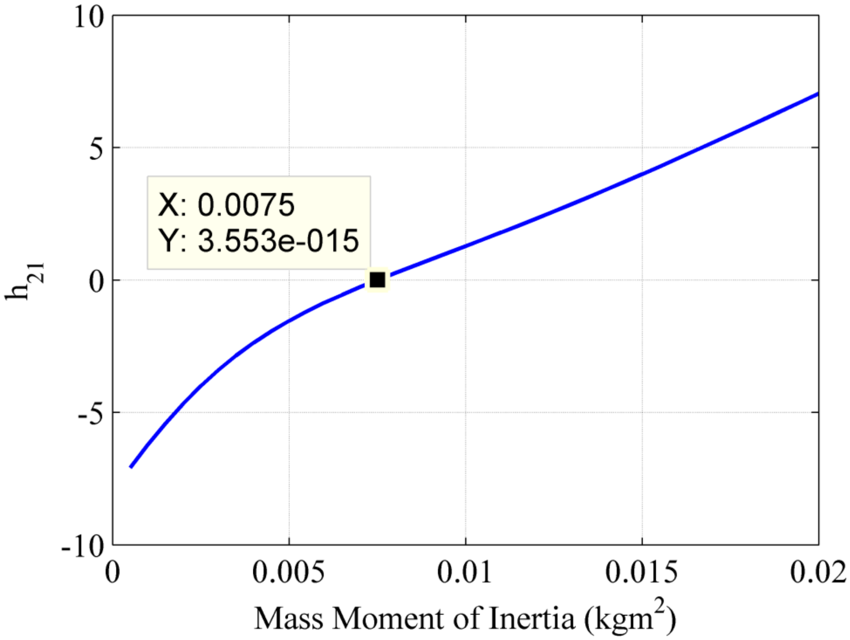

Figure 4.15: Determination of h_{21} as the mass moment of inertia is varied.

In general, adding internal dynamics to a mount can result in multiple resonances combining. However, if pole-zero cancellation occurs, that mode will no longer have a contribution to the system output quantity, the transmitted wall force. Furthermore, the allowance for rotation, which is non-harmful in the case of the final mass, may be beneficial. It should also be mentioned that, in the case of inexact pole-zero cancellation, the suppression effect of the cancelled mode on the transient response is still realized. This is evidenced by the relative width of the null in the wall force plots, such as the one in Figure 4.11. Sensitivity studies that also confirm this assertion may be found in Chapter 6 where optimization studies are presented.

4.7 Investigation by Energy Propagation

Other than the modal investigation, the investigation into the propagation of energy along the isolator provides useful insight into the dynamic isolation nature of the mount. In a finite length chain, the properties of wave reflection and attenuation influence the maximum force transmitted to the wall. A very simple but effective way of showing this is through energy, time, and element number plots [29]. The amount of energy in the system is tracked through the springs and velocity of the masses as:

$$KineticEnergy = \frac{1}{2} m_i v_i^2 + \frac{1}{2} J_i \omega_i^2 \tag{4.9}$$

$$PotentialEnergy = \frac{1}{2} k_i d_i^2 \tag{4.10}$$

where d_i is the deflection of the ith spring, v_i the translational velocity of the ith mass and ω_i the rotational velocity of the ith mass. To reduce the influence of impedance mismatching, which would cause early reflections and further complicate the situation of energy wave propagation (see Figure 2.8 as an example), the mass ratio, ε, is chosen to be 1 for this study with all masses and mass moments of inertia equal. As in previous studies, the total mass of the system was chosen to be 21 kg and the number of elements was chosen to be N=21. Thus, every mass in the system has a value of 1 kg; two different values of mass moment of inertia were investigated: J_i=10 kgm^2 and J_i=5e^{-3} kgm^2, for i=2-21.

Figure 4.16 displays the results for all mass moment of inertias set equal to the larger value: J=10 kgm^2. The kinetic energy of the masses displayed in the figure is placed at the nominal location of the masses; the potential energy of the springs is placed at the locations in-between the mass locations. For this large value of mass moment of inertia, the energy propagates cleanly along the chain for the first 0.3 seconds. This is due to the fact that the motion is dominated by translational movement, with little-to-no rotational movement. Only after the pulse strikes the wall does the wave begin to break up and the propagation pattern of the energy becomes more complex. In the case where all mass moment of inertias are set to: J=5e^{-3} kgm^{2}, which is shown in Figure 4.17, the main energy pulse begins to immediately break into two bands of propagation. This wave shedding from translational into rotational energy results in two different wave speeds. This varied speed of propagation results in a decreased wall force around 0.3 seconds because the energy from the two different waves arrives at the wall at different times; furthermore, while the rotational wave carries energy, the rotational movement of the last mass has no contribution to the wall force as discussed earlier. Similar to the case with larger mass moments of inertia, once the wave reflects from the wall, it breaks up and the propagation pattern becomes more complex.

In the presence of damping, the chance that the two different energy propagation bands will recombine later in time to form a large wall force is reduced. This is because damping acts as a means of reducing the signal strength with time as shown in equation (2.14). Further analysis on the influence of damping will be examined in Chapter 7.

4.8 The Phenomenon of Eigenvalue Curve Veering

It should be noted that in the absence of the first mass from the system shown in Figure 4.1, the translational and rotational modes of the system are completely uncoupled so long as the top and bottom springs are equal. When properly tuned, the natural frequencies of the translational and rotational modes can be made identical, so that each natural frequency is repeated. When the first mass is present, it disrupts this symmetry but the amount of that disruption depends strongly on its mass and on the offset location. When the mass is very small relative to the overall mount mass and/or the offset is small, eigenvalue veering may occur. This phenomenon is discussed in this section.

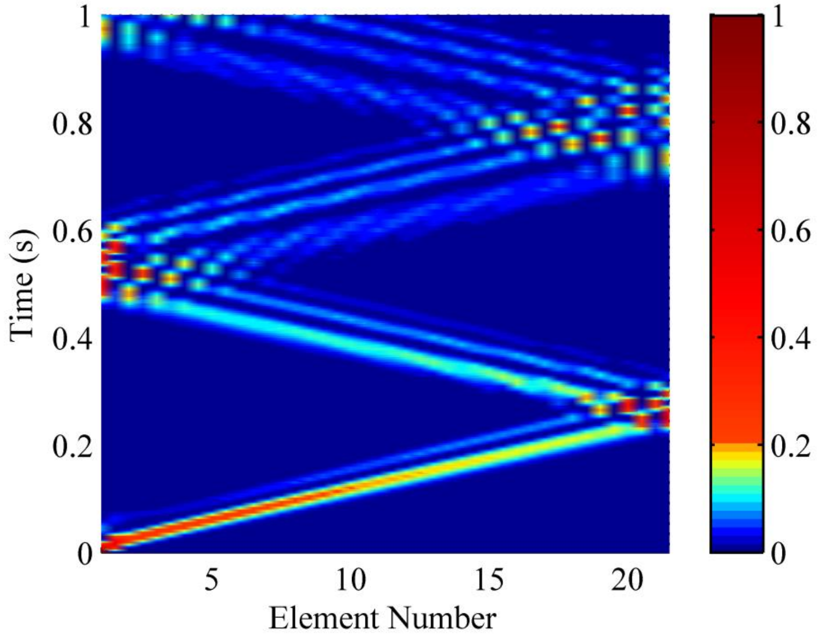

Figure 4.16: Energy evolution plot for 21 mass system with mass ratio 1 and mass moment of inertia 10 kgm^2.

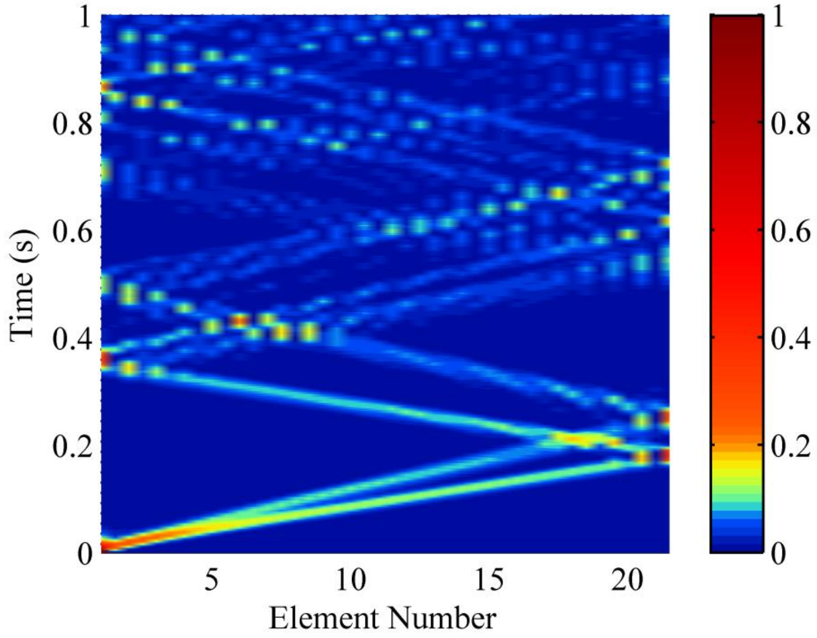

Figure 4.17: Energy evolution plot for 21 mass system with mass ration 1 and mass moment of inertias 5e^{-3} kgm^2.

When the first (leftmost) mass and spring are removed from the system, the translational and rotational dynamics of the system uncouple. It can be shown that the two sets of equations have a closely-related structure:

$$[M_x]\{\ddot{x}\} + [K_x]\{x\} = \{0\}$$

$$[M_\theta]\{\ddot{\theta}\} + [K_\theta]\{\theta\} = \{0\}$$

where $\{x\} = [x_2 \;\; x_3 \;\; \dots \; x_N]^T$, $\{\theta\} = [\theta_2 \;\; \theta_3 \;\; \dots \; \theta_N]^T$, $[K_\theta] = L^2[K_x]$, $[M_x]$ is a diagonal matrix having equal mass values m, and $[M_\theta]$ is a diagonal matrix having equal mass moments of inertia values J. Due to the fact that the rotational mass and stiffness matrices are just scaler multiples of their translational counterparts, it is easily concluded that each natural frequency of the rotational system is a scaler multiple of a natural frequency of the translational system. This scaler can be shown to be sqrt(mL^2/J), which suggests that if $J = mL^2$, the two translational and rotational systems will have equal natural frequencies. (Note that this agrees with the result of the preceding section, where $J=m_2L^2$ led to repeated roots.) We can refer to such systems where the translational and rotational systems are equal as systems that are “perfectly tuned.”

When the first mass, m_1, and its associated spring are added to a perfectly tuned system, the eigenvalues of the combined system will no longer occur in repeated pairs. However, if the mass is small, the eigenvalues will be very close, eigenvalue veering may occur. Studies of eigenveering first began in the 1960s, for example [54], [55]. As a particular parameter is varied, eigenvalue loci can approach one another and can either cross or veer. Three types of conservative systems that allow for truly multiple modes are: symmetric or cyclic structures, multi-dimensional substructures for which motions in different dimensions uncouple and structures with fully uncoupled substructures [56].

When two eigenvalue loci suddenly veer away, each one takes on the trajectory of the other and all the properties of the two modes are swapped: damping ratios, sensitivities, and eigenvectors [57].

The problem of quantifying veering has been historically difficult due to the subjective nature of its identification. Graphically veering can be determined via investigation; however, to determine a quantification of the veering depends on the curvature or second derivative of the eigenvalues. Liu suggested using critical values or curvature of eigenvectors, but conceded that determination of these values would remain subjective [58]. Perkins and Mote derived “coupling factors” that they used to identify the expected behavior of converging modes, which could be used to provide qualitative insight [59]. To alleviate some of this subjectivity, a veering quantification was created that utilized a nondimensional approach to provide universal identification of behavior via physically meaning quantities [60]. The approach in [60] is based on three criteria: the cross-sensitivity quotient, which describes the state of veering of two modes within their subspace; the modal dependence factor, which identifies the conformity of the modes to that subspace; and the veering index, which combines the two aforementioned factors to give a quantification of the veering intensity.

The discussion of this material is undertaken because of the potential to confuse the veering phenomenon with the true reason behind the wall force minima in plots such as Figure 4.5. Utilizing the formulation given in [60], the veering index for the system in Figure 4.5 was calculated. A veering index of one indicates a high level of veering, while a value near zero indicates no veering between the modes. From Figure 4.5 we see there is a large dip in the transmitted wall for near a mass moment of inertia of 0.04 kgm^2;

similarly, the veering index for multiple modes calculated in the same region, shown in Figure 4.18 indicates a large level of veering. However, investigation of the veering index in the vicinity of the deeper minimum of Figure 4.5, occurring near a mass moment of inertia of 2.7e^{-3} kgm^2, indicates little to no veering of the eigenvalues, Figure 4.19. Similar results were found for the higher modes (not shown.).

Thus, while eigenvalue veering is certainly a feature of the isolation system considered in this chapter, it seems that it does not appear to be the root cause of the favorable isolation performance. It occurs in some of the regions of low transmitted wall force and not in other regions of beneficial force isolation. Instead, the explanation for isolation rests in properties of the eigenstructure of the vibratory system, and on the coalescence and interference of modal contributions in the time response.

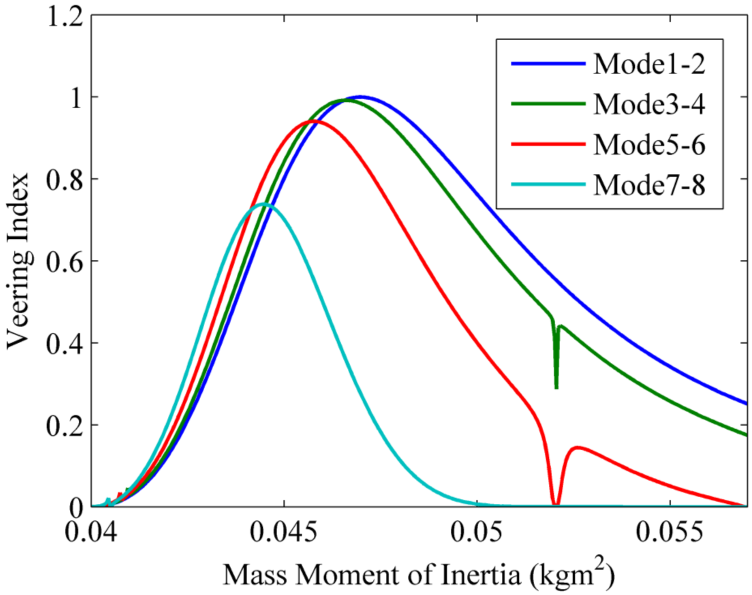

Figure 4.18: Veering index for multiple modes of a six mass system with M_{tot} = 21 kg and first mass = 1 kg around a mass moment of inertia of 4.5e^{-2} kgm^2.

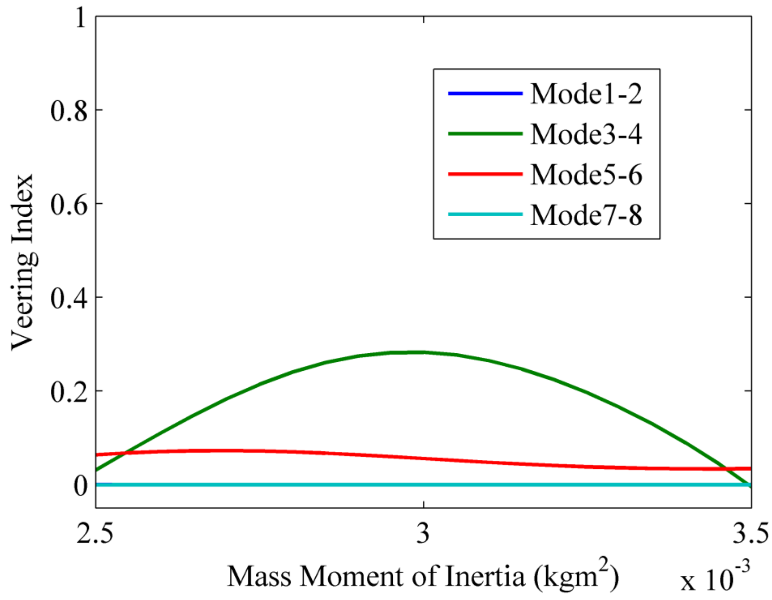

Figure 4.19: Veering index for multiple modes of a six mass system with M_{tot} = 21 kg and first mass = 1 kg around a mass moment of inertia of 3e^{-3} kgm^2.

4.9 Conclusion

In this chapter, the performance of finite-length chains of translational and rotational masses was evaluated. The systems consisted of 2 DOF masses interconnected with springs and dashpots. Trends in performance were studied as various system parameters were varied. The performance was evaluated based on the displacement of the first mass and on the wall force at the end of the chain. The design space was restricted in several important ways. Most notably, the overall mass of the isolation chains and overall static stiffness were held constant. Another restriction is that all spring constants were given equal values, and the masses and mass moments of inertias of the 2 DOF rigid bodies in the system were either identical, or varied in a 1-1 dimer chain manner. The restriction of equal masses, inertias, and spring values is relaxed in Chapter 6 where performance optimization is examined. The system's excitation was in the form of an initial velocity on the first mass (impulsive loading) whose magnitude resulted in a constant energy value.

For high energy inputs the chains possessing smaller masses moments of inertia yielded a decrease of the wall force while resulting in an increase in the displacement of the first mass. However, as the energy level was decreased it was found that certain values of the mass moment of inertia resulted in significant reduction in the transmitted wall force without large increases in the first mass displacement.

Examination of a simplified 3 DOF (2 mass) system showed that the magnitude of the first mass and the offset attachment location played an important role in generation of the substantial decrease in the wall force. Two different possible reasons for minima in the wall force were investigated: 1) The fact that the lightly coupled system could exhibit eigenvalue veering, and 2) That the dip may be the result of a beneficial eigenstructure related to how the first mass and offset attachment locations influenced the mass and stiffness matrices, respectively.

Application of a veering index showed that while veering may occur, it was not the main reason for the reduction in wall force. Instead, the system’s favorable eigenstructure, with the ability to place nodes at the excitation location, proved to be the main source in the reduction of the transmitted wall force.

Alternatively, examination of the energy propagation showed that the decrease in the wall force could be partially explained by the fact that the rotational motion led to the generation of multiple waves having different wave speeds, which arrived at the wall location at different times. When the mass values along the chain alternated in magnitude, it also resulted in the wave shedding energy as it propagated.

CHAPTER 5.

ISOLATOR CHAINS WITH INTERNAL ROTATING MASSES

5.1 Overview

This chapter documents the investigation of shock and vibration isolation in a chain of translating carts or housings having internally rotating eccentric masses. The internal masses have viscous damping, but nominally have no elastic or gravitational restraint, unless otherwise stated. Due to the lack of elastic or gravitational constraint on the rotating eccentric masses, they provide a nonlinear inertial coupling to their housings. First an investigation into the shock isolation potential of such a system is performed [61]. Afterwards, the response of the system to harmonic excitation is investigated [62]. It is seen that the dynamics of these systems is very complicated, but that trends are observed which have implications for practical isolation systems. Using simulation studies, tradeoffs are examined between displacement and transmitted force for a range of physical parameter values.

5.2 Isolation System Model

Figure 5.1 shows a simple schematic representation of the system with N translating masses. With the exception of the first mass, the remaining elements along the chain consist of a cart-housing having mass M and an internally rotating mass, m, which is assumed to be rotating in a track of radius, r_o, within the cart. The first mass is assumed to have no internally rotating mass, but has a mass value equal to the total mass of the remaining cart/mass systems, $M+m$. The carts are connected by linear springs of stiffness k. It is assumed that the circular track is oriented in the horizontal plane, so there is no "pendulum effect" present for the internal masses. The eccentric rotor mass, *m*, is inertially coupled to the primary mass and progresses along its track with damping, γ. The justification for omitting damping between the carts is based on high-frequency transmissibility in mounts. It is well known that as the damping between elements is increased, the high-frequency isolation performance is degraded.

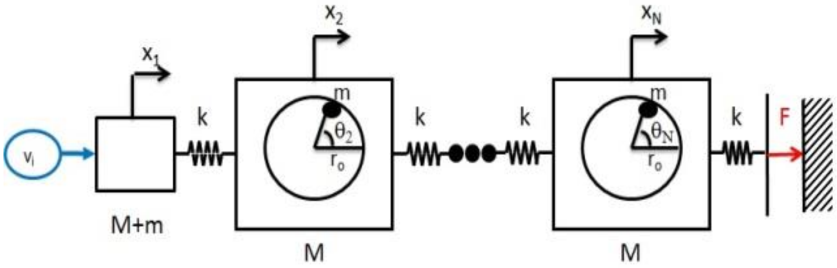

Figure 5.1: The isolation system mount for large internal rotation.

It is noted that the cart/mass systems are nominally identical, so the modelling approach can focus on a single cart and incorporate the appropriate elastic coupling of each cart to its nearest neighbors. To determine the equations of motion, Lagrange's method is applied; the kinetic and potential energy expressions and the Rayleigh's dissipative function for the ith cart (i > 1) are given by:

$$T = \frac{1}{2}(M+m)\dot{x}_i^2 + \frac{1}{2}mr_o^2\dot{\theta}_i^2 - mr_o\dot{x}_i\dot{\theta}_i \sin\theta_i \tag{5.1}$$

$$V = \frac{1}{2}k(x_{i-1} - 2x_i + x_{i+1})^2 \tag{5.2}$$

$$D = \frac{1}{2}r_o^2\gamma\dot{\theta}_i^2 \tag{5.3}$$

where γ is the linear viscous damping coefficient which relates the damping force tangent to the track to the relative velocity, and other terms are defined as shown in Figure 5.1. After application of Lagrange's method the equations of motion are given as:

$$\ddot{\theta}_i = \frac{m\dot{\theta}_i^{\,2}cos\theta_i sin\theta_i}{(M+m)*\left(1-\frac{m}{M+m}sin^2\theta_i\right)} + \frac{k\Delta X_i sin\theta_i}{r_o*(M+m)*\left(1-\frac{m}{M+m}sin^2\theta_i\right)} - \frac{\gamma\dot{\theta}_i}{m*\left(1-\frac{m}{M+m}sin^2\theta_i\right)}$$

$$\ddot{x}_i = \frac{-r_o\gamma\dot{\theta}_i sin\theta_i + m r_o\dot{\theta}_i^{\,2}cos\theta_i + k\Delta X_i}{(M+m)*\left(1-\frac{m}{M+m}sin^2\theta_i\right)} \tag{5.4}$$

where x_i is the displacement of the i^th^ cart housing, θ_i is the angle of the internally rotating mass of the i^th^ cart, and ΔX_i is the term related to the relative displacements of the cart to its nearest neighbors:

$$\Delta X_i = x_{i+1} - 2x_i + x_{i-1} \tag{5.5}$$

Note that x_1 is the displacement of the first mass (having no internally rotating mass) and x_{N+1} is zero since it corresponds to the wall attachment point.

Similar to the work in Chapter 2, the system mass and static stiffness are held constant, the performance objectives of critical interest are the wall force, Fw, and the displacement of the first mass, x_1. The input into the system is taken to be an impulsive load applied to the first mass, which represents an instantaneous change in the velocity of the first mass is given by: $\dot{x}_1(0) = v_1 = \sqrt{\frac{2E}{m_1}}$, where E is the desired initial energy imparted to the system and M+m is the total mass of the first mass. The total mass of the mounting system was assigned to be 1 kg and was held constant regardless of the number of masses in the chain and the ratio of the cart-housing to the rotating mass was varied. The ratio of the rotating mass, m, to the cart housing, M, is given as:

$$R_m = \frac{m}{M} \tag{5.6}$$

Note that the theoretical range of R_m is $[0,\infty)$. The overall static stiffness of the system is maintained to be 200 N/m unless otherwise indicated.

Shown in Figure 5.2 and Figure 5.3 are numerical simulations results for a chain of N=5 masses as the initial rotating mass angle, θ (rad), was varied along with R_m. The damping, γ, is 5 Ns/m and the radius of the circular path, r_o, was 0.1 m. The initial energy was kept constant at E=1 Nm. Figure 5.2 indicates that the transmitted minimal wall force occurs for large R_m and for oscillator initial angle positions near $\theta = \pi/2$; i.e., when the internal rotating masses are furthest from the center line of the chain. This is due to the fact that this geometry results in the largest amount of initial moment and causes the largest amount of internal rotational movement. This results in the largest amount of energy to be captured in the form of kinetic energy of the rotating masses as well as the greatest amount of energy removal by way of the viscous track damping. Similarly, when the rotation mass is initially positioned at oscillator angles of 0 or π, the wall force is relatively high because it results in zero movement of the internal masses.

The effect of the angle and radius on the amount of rotation can be seen by considering a single cart-mass system. Summing moments about the center of the track and neglecting damping, we can obtain the relation:

$$\ddot{\theta} = \frac{\sin\theta}{r_o}\ddot{x} \qquad (5.7)$$

where $\ddot{x}$ is the horizontal acceleration of the housing. This equation shows that the angular acceleration of the internal mass is maximized at $\theta = +/- \pi/2$, and is inversely dependent on r_o.

When comparing Figure 5.2 and Figure 5.3, it can be seen that the transmitted wall force is far more sensitive to the initial oscillator angle and R_m than is the maximum first mass displacement. The maximum first mass displacement is held to a minimum over a large range of values for both varied parameters. However, a significant reduction in both the maximum first mass displacement and maximum wall force occurs in similar regions of the parameter space: $\theta = \pi/2$ and R_m=1.80. This simultaneous reduction does not follow the classic tradeoff relationship in mount isolation systems, which is a welcomed finding.

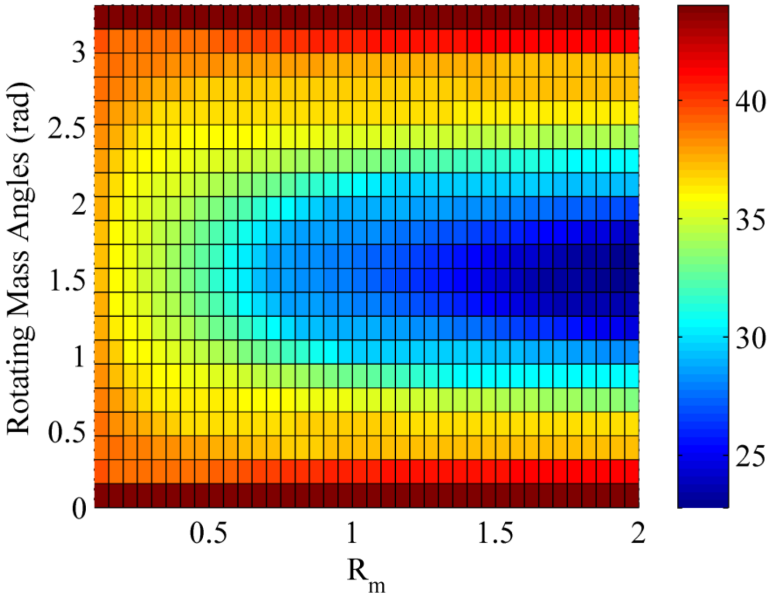

Figure 5.2: Maximum wall force for γ = 5 Ns/m, r_o = 0.1 m for chain length of five.

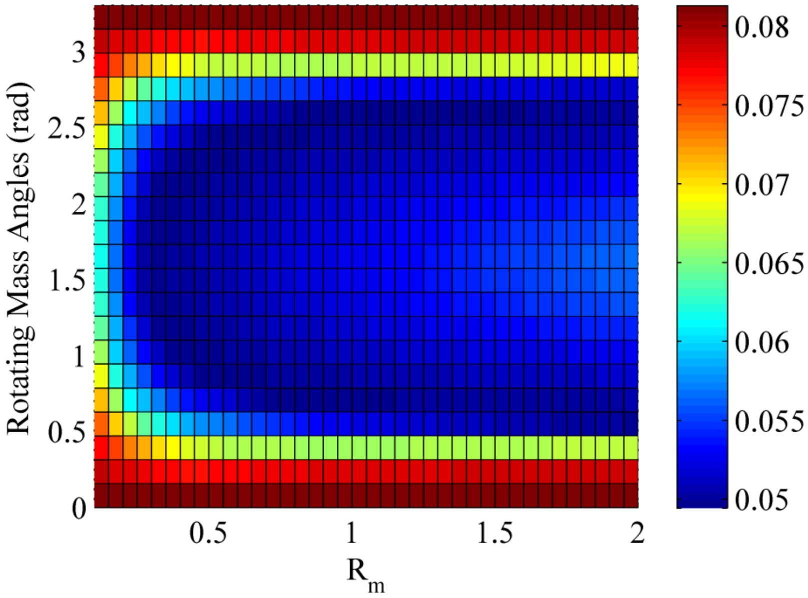

Figure 5.3: Maximum first mass displacement for γ = 5 Ns/m, r_o = 0.1 m for chain length of five.

Figure 5.4 and Figure 5.5 display the time-response movement of selected cart-housings and rotating masses versus time for γ =5 Ns/m and r_o=0.1 m for a chain of length N=5. Recall that there is no rotating mass inside the first mass of the chain. As can be seen in Figure 5.4 and Figure 5.5 for R_m=1.8 and initial angle $\theta = \pi/2$, the impulsive load propagates down the chain of masses as time evolves. The maximum displacement of the first housing is approximately double that of the maximum displacement of the final house, housing 5, which determines the wall force. This result is due to the fact that the chain system can quickly shift some of the translational vibratory energy into rotational energy and then remove some of it via the viscous damping of the rotating masses. As shown in Figure 5.5 the rotating masses move as soon as their housing begins to move and thus begin to dissipate the transmitted impulsive load. The dissipation of the vibration results in a decrease in the movement of subsequent masses and ultimately results in a decreased wall force as shown in Figure 5.2. Sigalov et al. [63] showed that for a single attachment, resonance capture corresponds to nonlinear normal modes, which could result in complete energy transfer to the nonlinear energy sink after a limited number of oscillations of the primary mass. However, in the present case, the movement of translational to non-harmful rotational movement is being utilized to alleviate the motion *prior to* the shock disturbance hitting the wall. While this helps explain the concepts under consideration, the mount length, viscous damping and circular pathway radius have yet to be explored and will be done so now.

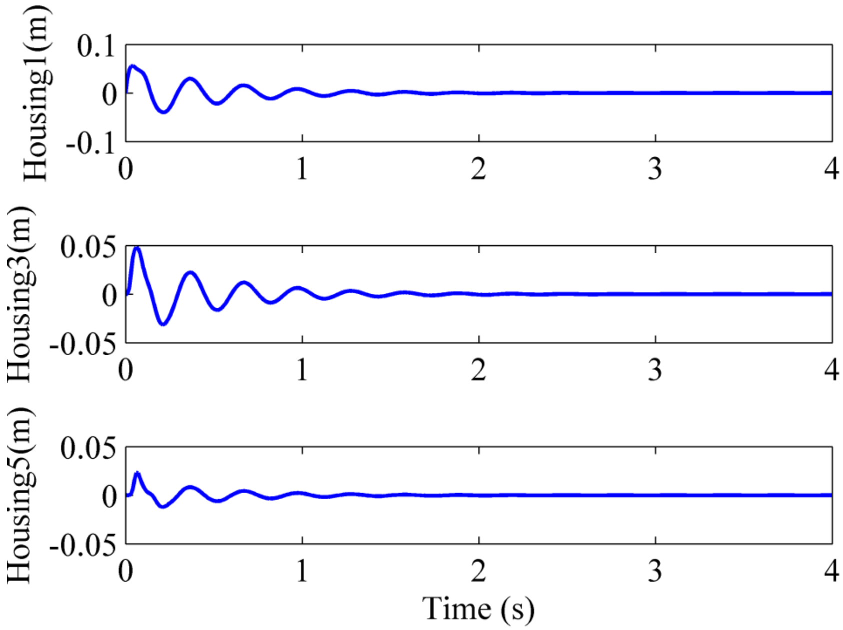

Figure 5.4: Comparison of selected housing displacement (m) versus time (s) for R_m = 1.8, γ = 5 Ns/m, r_o = 0.1 m for chain length of five.

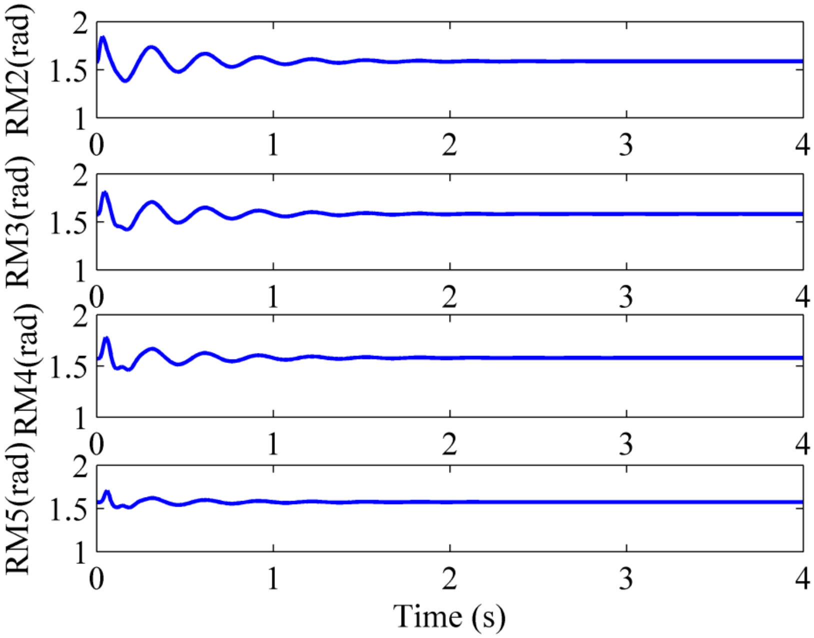

Figure 5.5: Comparison of rotating mass (RM) angular displacements (rad) versus time (s) for R_m = 1.8, γ = 5 Ns/m, r_o = 0.1 m for chain length of five. (Note: There is no rotating mass one)

5.3 Shock Isolation Design Space Exploration

One of the parameters under consideration is the radius of the rotating mass pathway, r_o. The results for decreasing r_o to 0.01 m are shown in Figure 5.6 and Figure 5.7. In spite of the 10x reduction in the pathway radius, the range of values in the transmitted wall force have remained approximately the same. Similarly, the maximum first mass displacement range has remained approximately the same. However, the result indicates that the most favorable initial starting angle decreases from π/2 rad (90^O) to 1.25 rad (72^o). Figure 5.7 implies that the sensitivity of the maximum first mass displacement has increased for r_o=.01 vs r_o=0.1m. This is evident by the large fluctuation in the maximum first mass displacement for small values of mass ratio R_m.

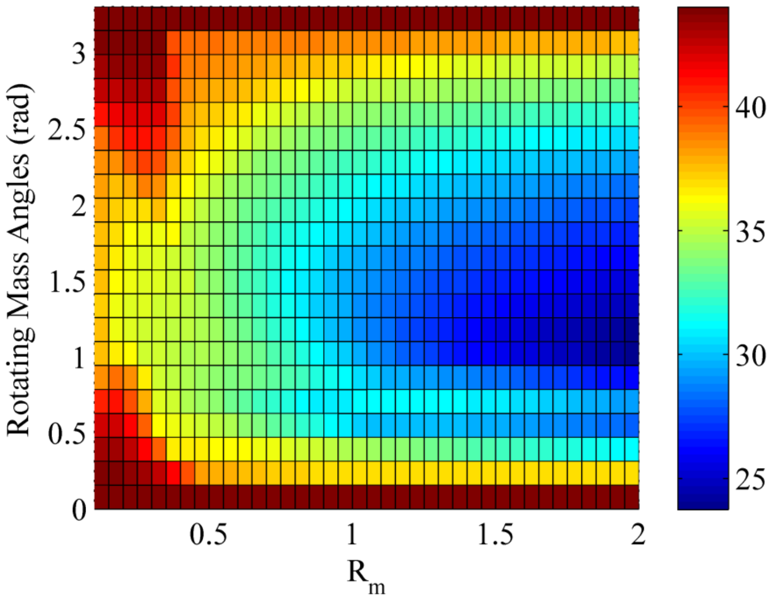

Figure 5.6: Maximum wall force (N) for γ = 5 Ns/m, r_o = 0.01 m for chain of length five.

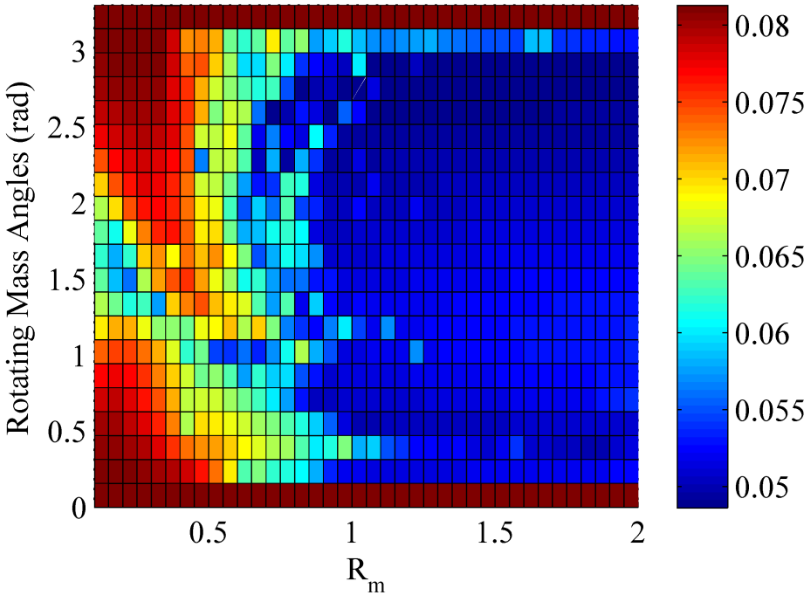

Figure 5.7: Maximum first mass displacement (m) for γ = 5 Ns/m, r_o = 0.01 m for chain of length five.

At the present level of damping, it was found that increasing the circular track's radius to r_o=1 m, did not result in a significant change in either the transmitted maximum wall force or maximum first mass displacement. A dimensional analysis reveals that this situation is likely to change if the damping value, γ, and/or the initial energy level, E, is changed. In other results, increasing γ beyond 5 Ns/m had relatively little effect on the mount performance. However, lowering the damping level to a small value, such as γ=0.01 Ns/m did have a noticeable effect as shown in Figure 5.8 and Figure 5.9.

The damping coefficient, γ, influences the level and rate of energy extraction from the system. As γ approaches 0, the isolation system runs the increased risk of returning energy from the internal rotating masses to the outer housing at inopportune times. If the damping coefficient is too high, the energy loss will also diminish because it will inhibit the movement of the inner masses.

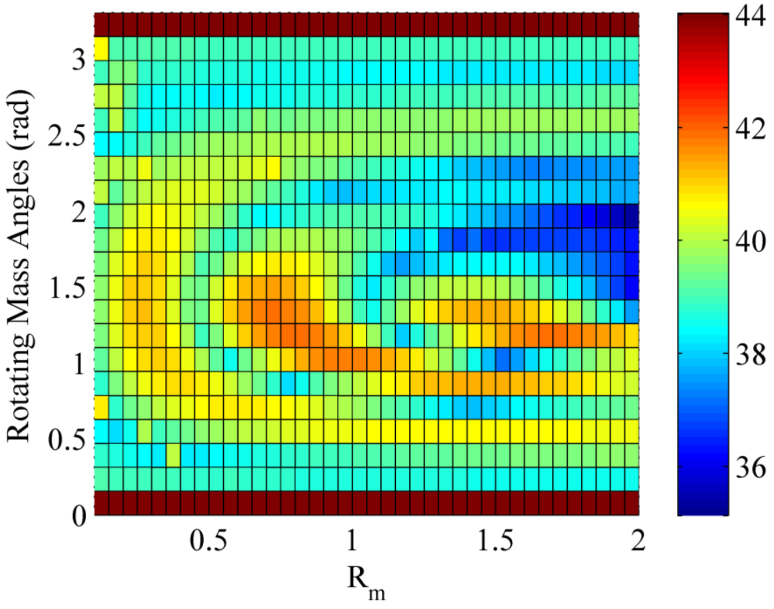

Figure 5.8: Maximum wall force (N) for γ = 0.01 Ns/m, r_o = 0.1 m for chain of length five.

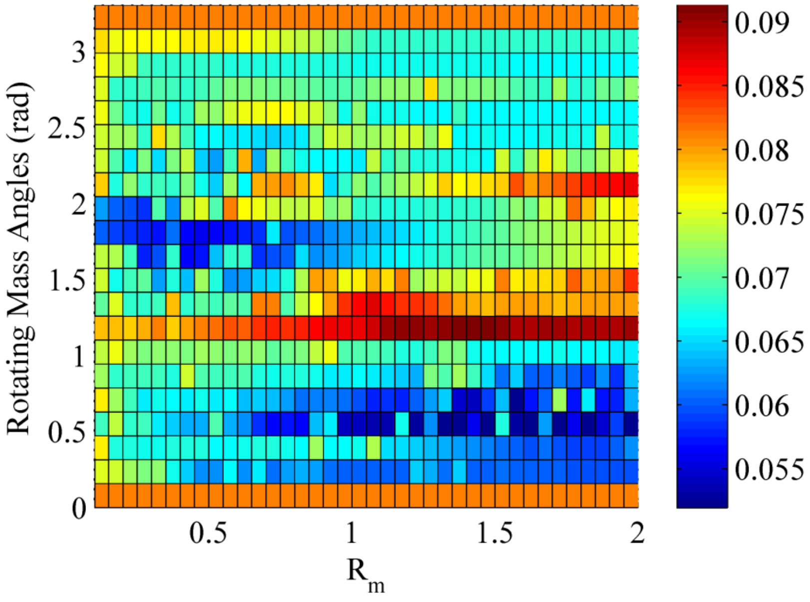

Figure 5.9: Maximum first mass displacement (m) for γ = 0.01 Ns/m, r_o = 0.1 m for chain of length five.

Comparing Figure 5.8 to Figure 5.2, it is seen that that the minimal value for the maximum transmitted wall force has increased by approximately 40% for the lower level of damping. This is due to the lack of energy removal via dissipation. Of course the maximum values in Figure 5.2 and Figure 5.8 are equal due to the fact that at $\theta = 0,\pi$, the damping coefficient has no influence on the result due to the lack of motion in the rotating mass, *m*. The change in the maximum first mass displacement plot, Figure 5.9, shows a complex distribution of the maximum and minimum values. However, the range of values does not change very much, indicating that the maximum first mass displacement may not be influenced very much by the level of damping. This result may not be surprising, as the first mass does not have a rotating inner mass. Thus, the energy is removed from the system only after it has passed to subsequent masses in the chain.

Figure 5.10 - Figure 5.13 display the results of numerous numerical simulations as the length of the chain, *N*, is increased with γ and r_o held constant. For *N*=9, the maximum transmitted wall force is decreased slightly relative to the results for the shorter chain, *N*=5, while the maximum first mass displacement is greatly reduced. For *N*=21, the maximum transmitted wall force is decreased slightly further relative to *N*=9, with a larger decrease shown in the first mass displacement. Recall, that as the number of housings in the system is increased, the spring constant, *k*, must be increased to keep the overall static stiffness constant. Due to this inherent design constraint, a stiffer system should have a decrease in the first mass displacement. However, it is expected that this would result in a large wall force. This issue seems to be contrasted by the fact that the energy is extracted from cart to cart through the action of the nonlinearly rotating mass.

The rotation redirects the transmitted impulse to a non-harmful movement and then dissipates it through the viscous damping.

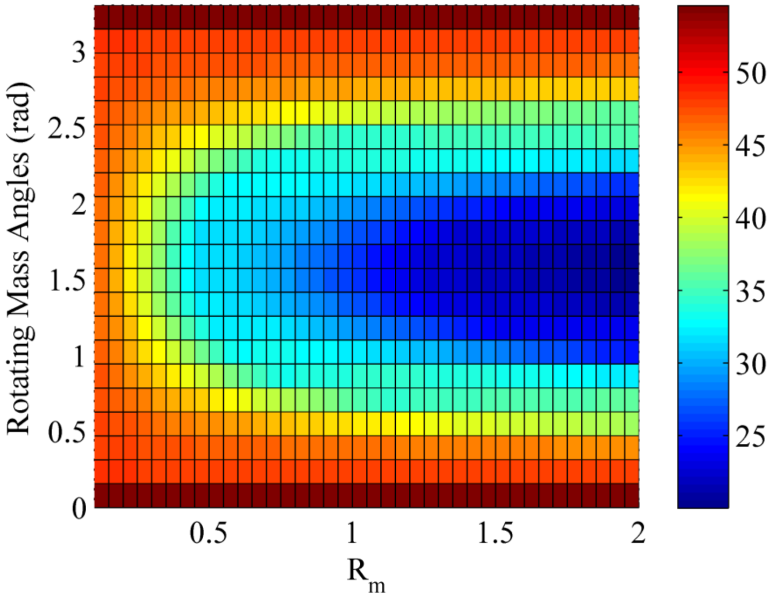

Figure 5.10: Maximum wall force (N) for γ = 5 Ns/m, r_o = 0.1 m for chain of length nine.

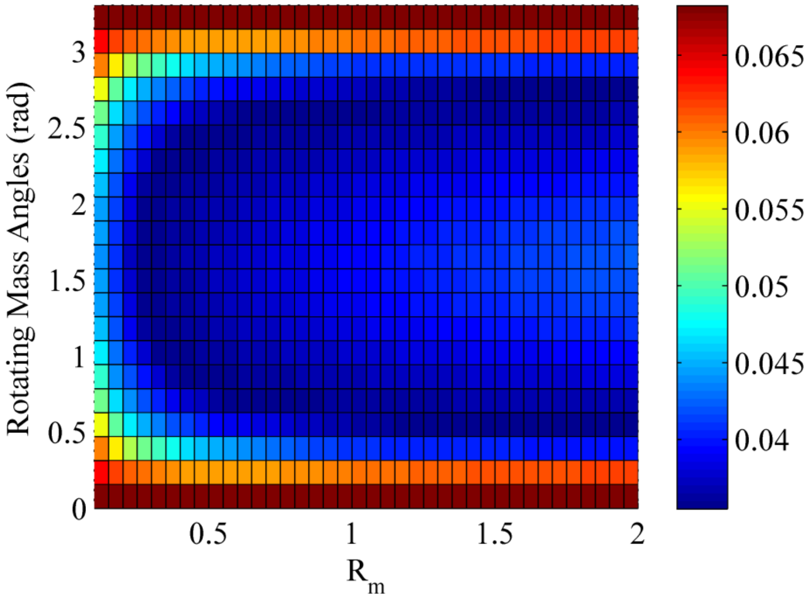

Figure 5.11: Maximum first mass displacement (m) γ = 5 Ns/m, r_o = 0.1 m for chain of length nine.

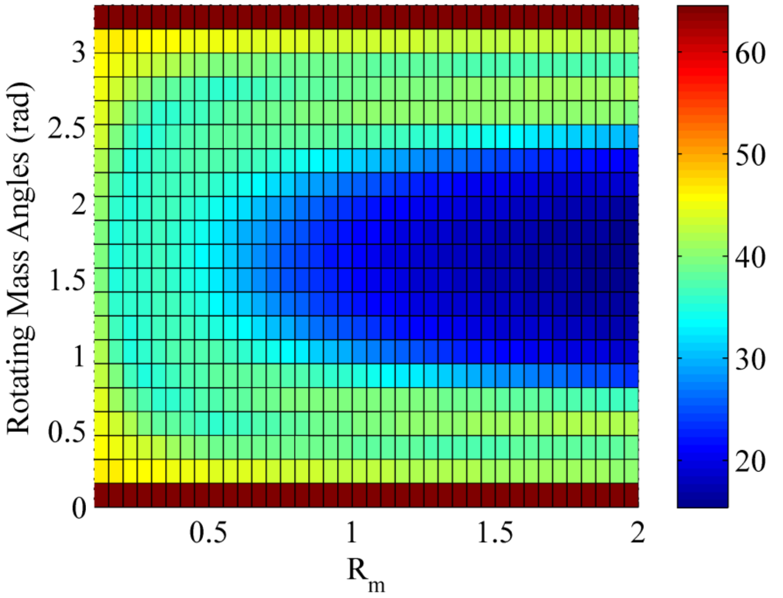

Figure 5.12: Maximum wall force (N) for γ = 5 Ns/m, r_o = 0.1 m for chain of length twenty-one.

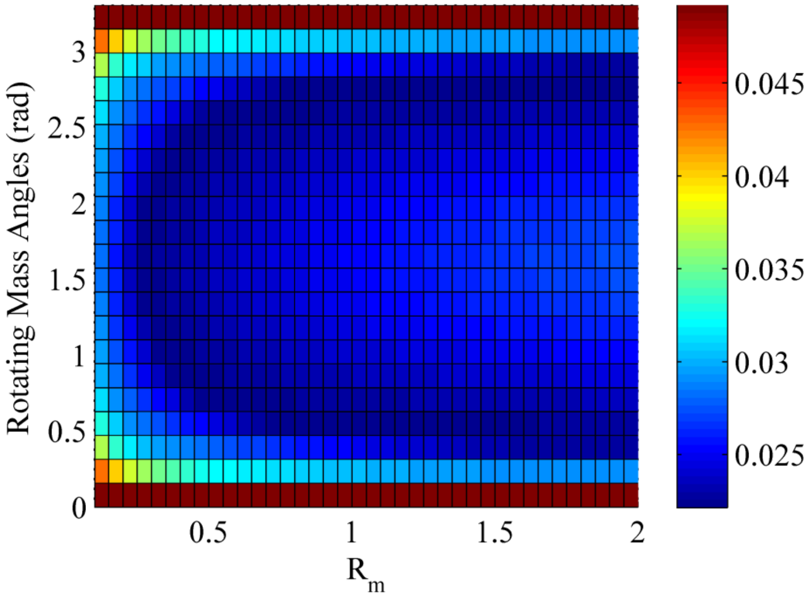

Figure 5.13: Maximum first mass displacement (m) for γ = 5 Ns/m, r_o = 0.1 m for chain of length twenty-one.

Figure 5.14 and Figure 5.15 show the movement of the housing and rotating masses, respectively, for N=21, γ =5 Ns/m, R_m=1.8, and r_o=0.1 m. Housing 1 is where the impulsive load is applied and the movement of housing 21 determines the transmitted wall force. As shown in Figure 5.14 there is a substantial decrease in the movement of the housing 21 when compared to housing 1, nearly amounting to a factor of 10. Figure 5.15 displays the movement of the rotating masses as the impulse travels down the chain. Each rotating mass goes through a sudden movement as the impulse travels down the chain, quickly dissipating the energy down the chain.

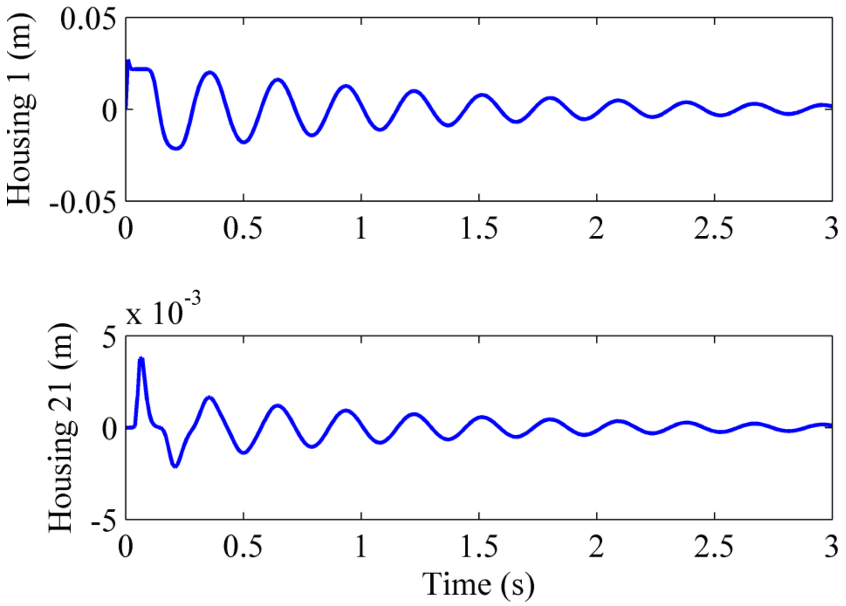

Figure 5.14: Comparison of selected housing displacement (m) versus time (s) for R_m = 1.8, γ = 5 Ns/m, r_o = 0.1 m for chain of length twenty-one.

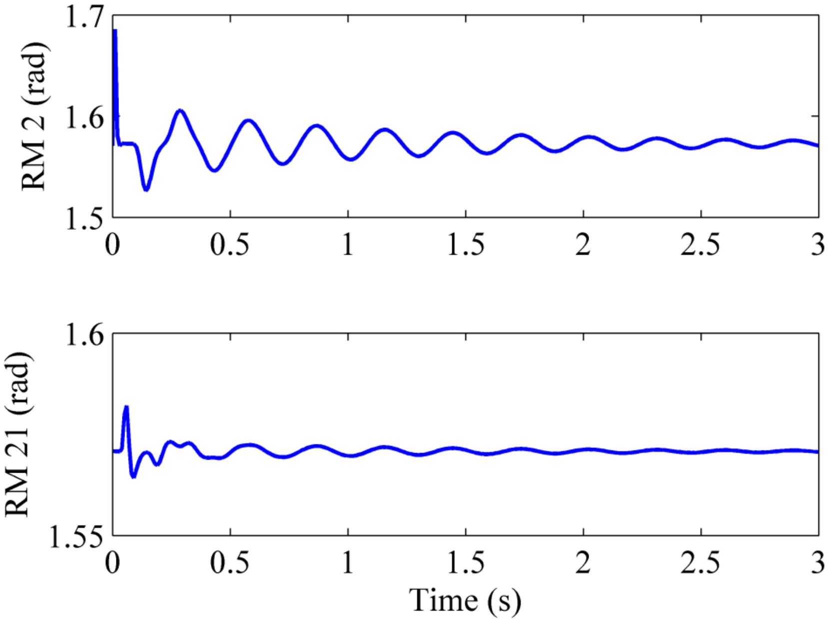

Figure 5.15: Comparison of rotating mass angular displacements (rad) versus time (s) for R_m = 1.8, γ = 5 Ns/m, r_o = 0.1 m for chain of length twenty-one.

The results shown above have displayed relatively small rotation angles occurring over the course of the time response simulations. However, if the strength of the impulsive input is increased, the oscillation of the rotating eccentric masses can become substantial. To showcase this phenomenon, a five-mass chain with γ =5 Ns/m was investigated for an initial angle of each rotating eccentric mass set to $\pi/2$ radians and R_m of 1.8. The amount of energy placed into the system is 100 times greater than the previous cases. This results in an increase in the instantaneous velocity of the first mass by a factor of 10. As shown in Figure 5.16, after the large input is applied to the system, the amount of oscillation that each rotating mass undergoes is significantly increased. For example rotating eccentric mass 2 undergoes rotation over a range of 382^o while rotating eccentric mass 5 only undergoes a rotation range of 119^o.

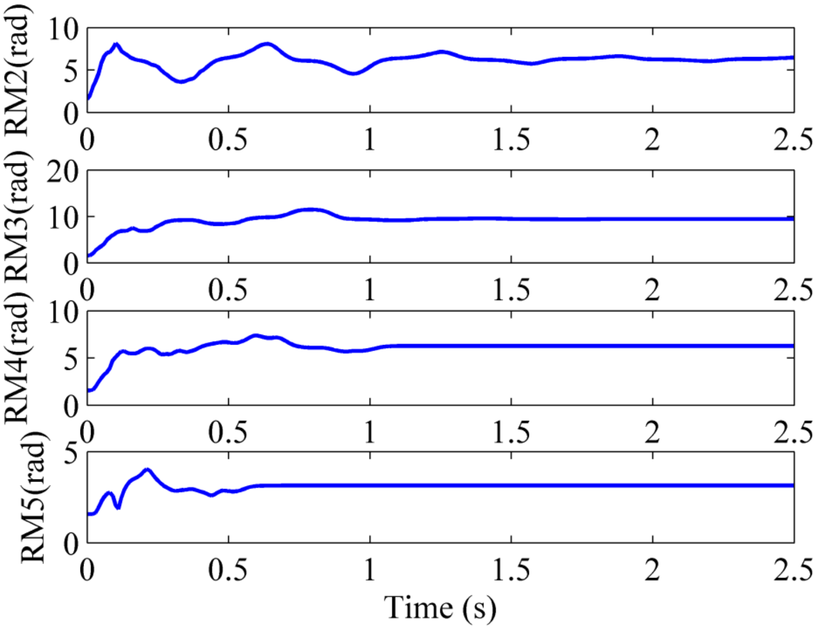

Figure 5.16: Comparison of rotating mass angular displacements (rad) versus time (s) for $R_m = 1.8$, $\gamma = 5$ Ns/m, $r_o = 0.1$ m for chain of length five. Energy input is 100 Nm.

5.4 Harmonic Excitation: Large Amplitude Rotational Single Degree-of-Freedom System

Clearly, the rotation angles of the internal masses can be quite significant as the amplitude of the vibration of the housing increases. Considerable insight into the range of expected motion can be obtained from an examination of a single cart/mass system. In particular, we consider a single “housing”, M, whose translational motion is described by the coordinate x. The housing is assumed to undergo prescribed harmonic motion of the form:

$$x(t) = A\sin(\omega t) \tag{5.8}$$

Inside the housing is a rotating eccentric mass, m, which travels along a circular pathway of radius r_o. Again, the circular pathway is oriented in the horizontal plane so that gravity can be neglected. The position of the rotating eccentric mass is defined by θ. The only form of damping in the system is linear viscous damping along the circular pathway defined by γ. The resulting single-degree-of-freedom (SDOF) system is shown in Figure 5.17.

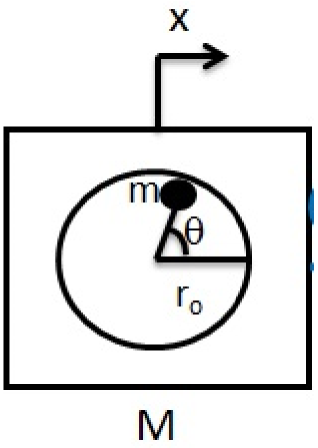

Figure 5.17: System model for one housing and one rotating eccentric mass.

The equation of motion for the system can be shown to be:

$$m r_o \ddot{\theta} + \gamma r_o \dot{\theta} - m \sin(\theta) \ddot{x} = 0 \qquad (5.9)$$

Substituting τ = ω*t* and utilizing the prescribed motion of the housing, equation (5.8), equation (5.9) becomes:

$$\theta'' = -g\theta' - X \sin(\theta) \sin(\tau) \qquad (5.10)$$

where primes denote derivatives with respect to τ and dimensionless parameters are defined as:

$$g = \frac{\gamma}{m\omega}; X = \frac{A}{r_o} \qquad (5.11)$$

Initial conditions [θ, θ'] are applied and the response of the system is found numerically based on nondimensional values for *g* and *X*. This approach is similar to that conducted in reference [64] in that prescribed harmonic excitation is applied to the system. However, the system under study here lacks the gravitational restoring moment. Depending on the specific values of X and g, and depending on the initial conditions, a variety of different trajectories for $\theta(\tau)$ can evolve. After a number of clockwise or counterclockwise rotations, the response can settle into a specific value of θ. However, it is also possible that no equilibrium angle is approached, and the mass settles into a uni-directional rotation, either clockwise or counterclockwise. Figure 5.18-Figure 5.20 show that the rotating eccentric mass converges or diverges for various initial conditions and for some values of g and X. These can be viewed as the domains of attraction for various types of steady-responses in the space of initial conditions (θ, θ'). The pink circles represent a convergence to an angle of 0 radians through counterclockwise rotation. The red circles are convergences to 0 radians through clockwise rotation. Light blue is convergence to π radians through counterclockwise motion. Dark blue is convergence to π radians through clockwise rotation. Finally, the black circles represent a continuous rotation which does not provide a distinction between clockwise or counterclockwise rotation.

Convergence is defined as a settling on or oscillating slightly around a specific angular position for the rotating eccentric mass. As shown, depending on the initial conditions, $[\theta, \theta']$, and the nondimensional values of g and X, the system has rich and complicated regions of divergence or convergence. It is also worth noting that all of these plots reflect the fact that the nonlinearity in the governing equation, equation (5.10), is odd; i.e., if the initial conditions are negated, the resulting solution to equation (5.10) is negated. Another fascinating fact is that the number of rotations that occur before the mass settles to a final value can be highly variable.

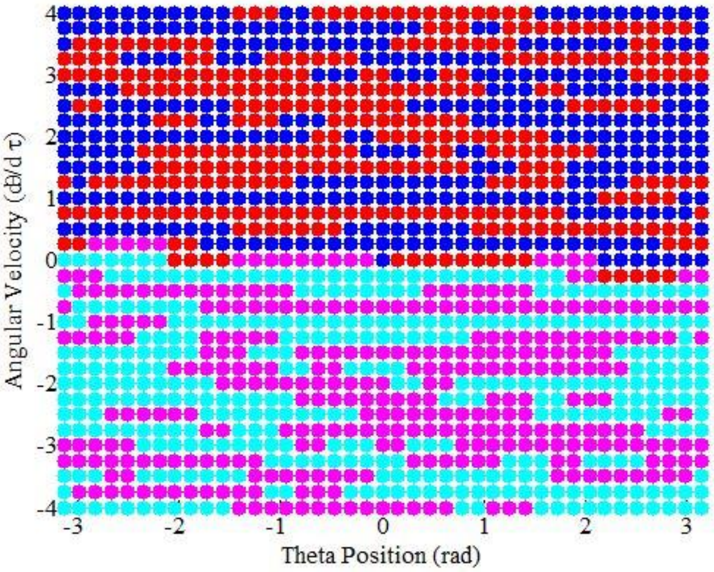

Figure 5.18: Domains of attraction for various types of observed response; θ′ (radians per non-dimensional time) vs θ (rad) for *g* = 0.1 and *X* = 0.1.

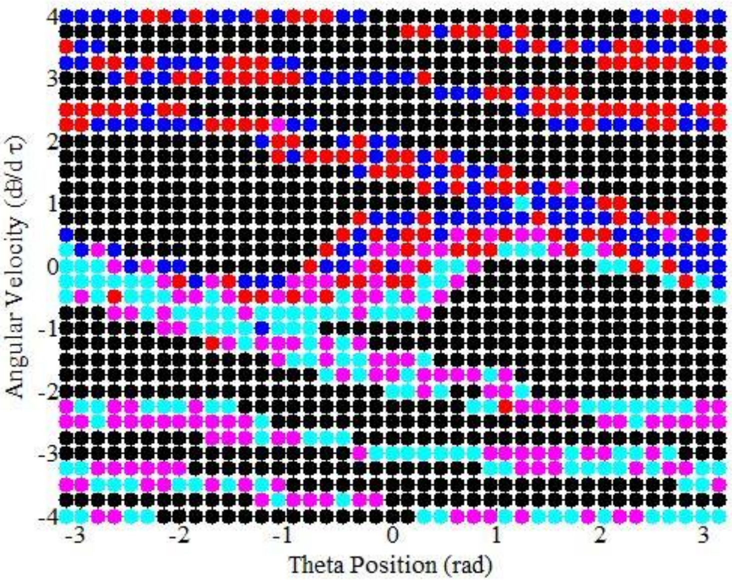

Figure 5.19: Domains of attraction for various types of observed response; θ′ (radians per non-dimensional time) vs θ (rad) for *g* = 0.1 and *X* = 0.5.

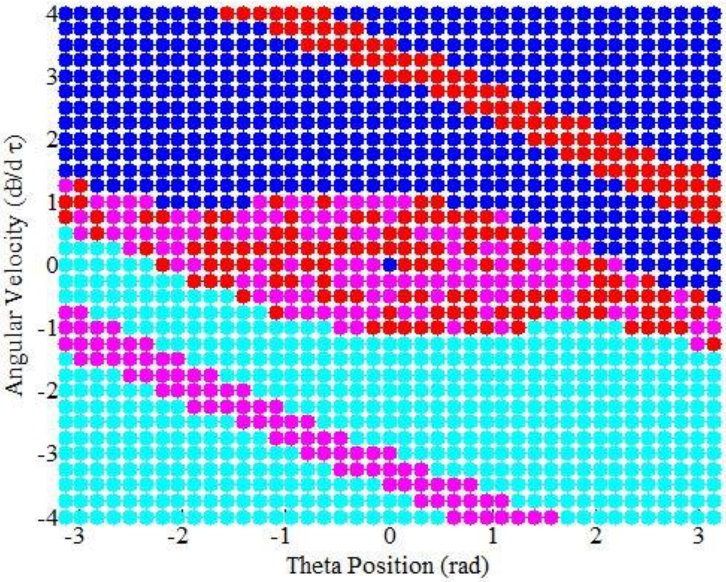

Figure 5.20: Domains of attraction for various types of observed response; θ′ (radians per non-dimensional time) vs θ (rad) for *g* = 0.5 and *X* = 0.5.

This behavior is exemplified in Figure 5.21, which shows the time response for the same initial position of the rotating mass, but with two different rotation rates. Both responses end with the mass converging to a location to the right of the path's center, but the higher initial rotation rate actually rotates counterclockwise through a complete revolution first.

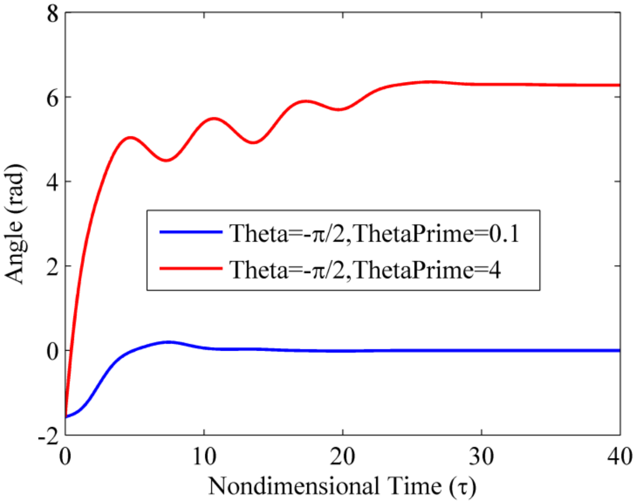

Figure 5.21: Comparison of two different initial starting velocities eccentric masses.

5.5 Harmonic Excitation of Chains of Large Amplitude Rotational Motion

In this section, we consider again the system of Figure 5.1, but examine the situation where the input to the system is harmonic excitation instead of impulsive loading. As shown previously, the motion of the rotating eccentric masses is highly dependent on the initial conditions. Due to this complication, the results below are started with every rotating eccentric mass at rest with an angle of $\theta = \pi/2$ and the housing masses are at rest. Note that this is very different than what might be done in an actual experimental test where the frequency is gradually changed and then dwelled until a new steady-state is observed. The reason for choosing the initial angular displacement of the rotating eccentric masses to be $\theta = \pi/2$ is simply to maximize the initial angular acceleration of the rotating masses and thus start dissipation of the harmonic excitation via the linear viscous damping as early as possible in the response.

Numerical simulations were performed in Matlab using the ode113 function. The simulation time was set to be 400 cycles of the input frequency; the steady-state results were checked by comparing the maximum transmitted force between cycles 300-350 to cycles 350-400 with a tolerance of 0.5% deviation. The results of the nonlinear systems were compared to associated linear systems. This “equivalent linear system” was created by placing linear viscous dampers between the masses and locking the rotating eccentric masses. The damping coefficients of the linear system were adjusted until the first resonant peak of the nonlinear and linear system was of equal magnitude.

Figure 5.22 and Figure 5.23 display the influence of mass ratio R_m on the steady-state amplitude of the wall force and first mass displacement for a chain of length N=5. As shown in Figure 5.22, as the value of R_m is increased, the amplitude of the transmitted force is decreased through the region of amplification. However, in the frequency region of isolation (ω > 140 rad/s), the isolation performance of the mount becomes worse as R_m is increased. This is due to the complex movement of the housings because of the rotating eccentric mass movement. For large R_m (i.e., $m >> M$), the displacement of the eccentric masses, m, will tend to zero in inertial space as ω goes to infinity. However, the housing masses will continue to move, thus contributing to higher wall force in the isolation frequency range.

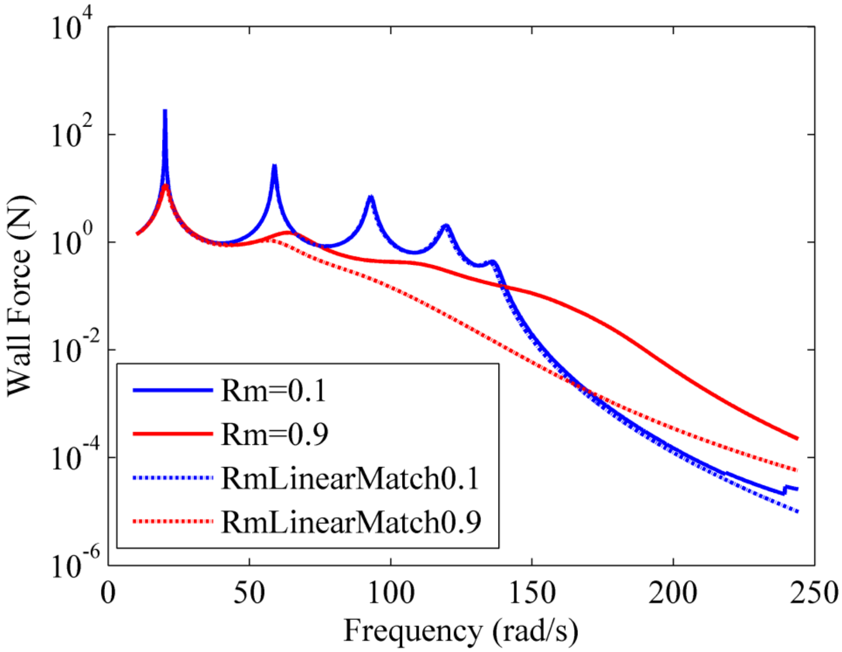

Figure 5.22: Transmitted wall force amplitude (N) for various values of R_m. $N = 5$, r_o = 1m, γ = 5 Ns/m and input force amplitude Force = 1 N.

Figure 5.23 displays the result of the first mass displacement as a function of frequency for various values of mass ratio R_m. As the value of R_m is increased, the first mass displacement decreases throughout the entire frequency range. However, the equivalent linear mount behaves slightly better than that of the nonlinear mount.

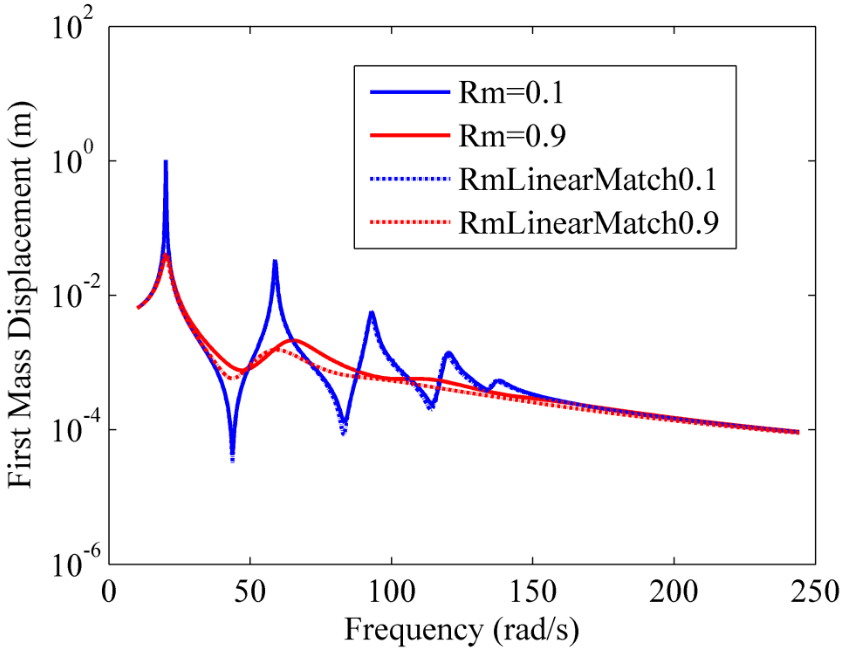

Figure 5.23: First mass displacement for various values of R_m. $N = 5$, $r_o = 1$m, $\gamma = 5$ Ns/m and input force amplitude Force = 1 N.

Figure 5.24 and Figure 5.25 display the movement of the housings and rotating eccentric masses for $R_m = 0.9$ and a driving frequency of the first natural frequency of the linear system ($\omega = \omega_{n1}$). It is seen that the housing masses undergo resonant growth until the level of damping in the system balances out the growth phenomena. The displacement amplitude of the rotating eccentric masses similarly increases as time progresses; however, the rotating eccentric masses tend to oscillate about an angle of $\theta = \pi/2$.

As the amplitude of the harmonic driving force in the system increases, the results significantly change from the case of smaller levels of forcing. In this case, the rotating eccentric masses may break away from their attraction to the region of $\theta = \pi/2$.

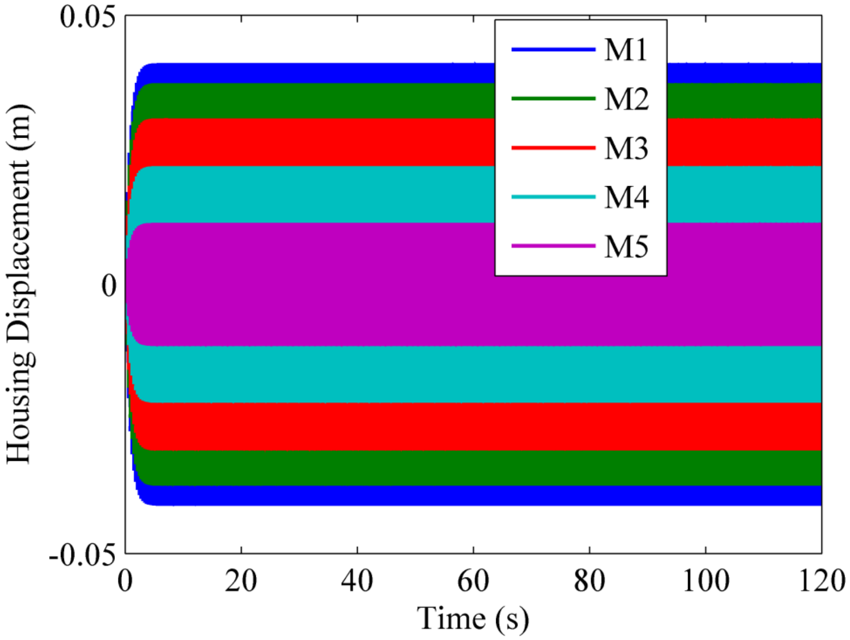

Figure 5.24: Housing displacement for $R_m = 0.9$, $\omega = \omega_{n1}$, $N = 5$, $r_o = 1$m, $\gamma = 5$ Ns/m and Force = 1 N.

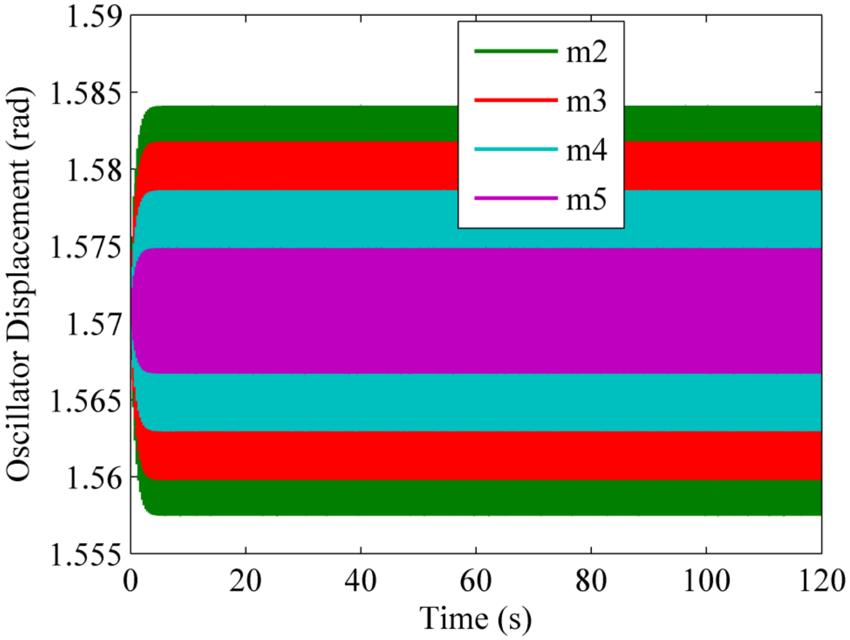

Figure 5.25: Eccentric mass rotation for $R_m = 0.9$, $\omega = \omega_{n1}$, $N = 5$, $r_o = 1$m, $\gamma = 5$ Ns/m and Force = 1 N.

This situation is shown in Figure 5.26 and Figure 5.27 for a force input amplitude of 16 N. Initially, Figure 5.27 shows that the rotating masses all seem to oscillate about 90-degree angles. However, at approximately t=70 s, the second mass (shown in dark green) breaks free, and the angle settles to zero. The loss of energy dissipation in the second rotating mass causes the oscillation amplitude of the other masses to grow until around t=90 to 110 s, the other masses break free, settling to angles of π.

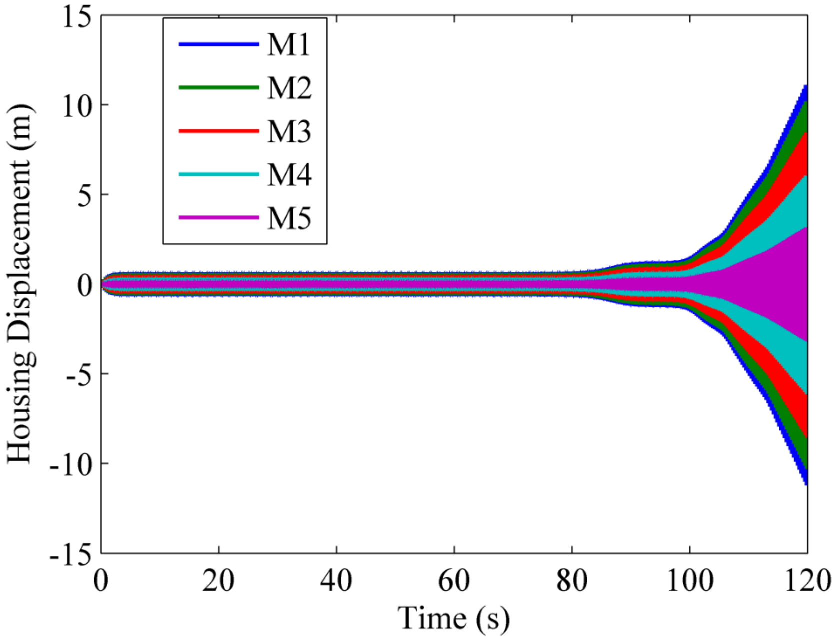

Figure 5.26: Housing displacement for $R_m = 0.9$, $\omega = \omega_{n1}$, $N = 5$, $r_o = 1$m, $\gamma = 5$ Ns/m and Force = 16 N.

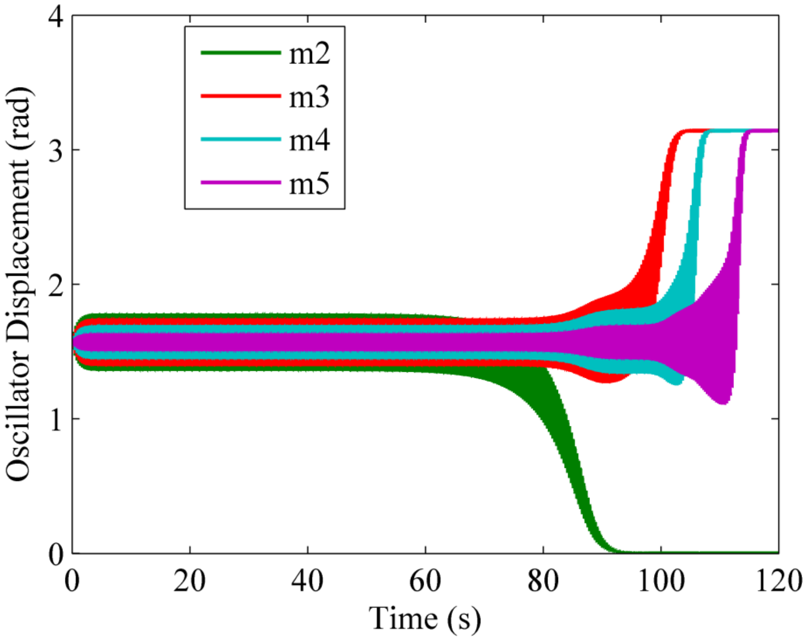

Figure 5.27: Eccentric mass rotation for R_m = 0.9, $\omega = \omega_{n1}$, N = 5, r_o = 1m, γ = 5 Ns/m and Force =16N.

If the force amplitude is further increased to 50 N, the situation is even more complicated and unpredictable as seen in Figure 5.28 and Figure 5.29. In this case, the movement of the rotating eccentric masses can significantly influence the housing movement. It is seen that only one of the rotating eccentric masses converges to a particular angle; the remaining three eccentric masses continue to oscillate and undergo full rotations, causing complex movement of the housing. Such situations make it extremely difficult to determine the steady-state value of the system, if one even exists. One way to investigate if steady-state exists is through Poincaré plots.

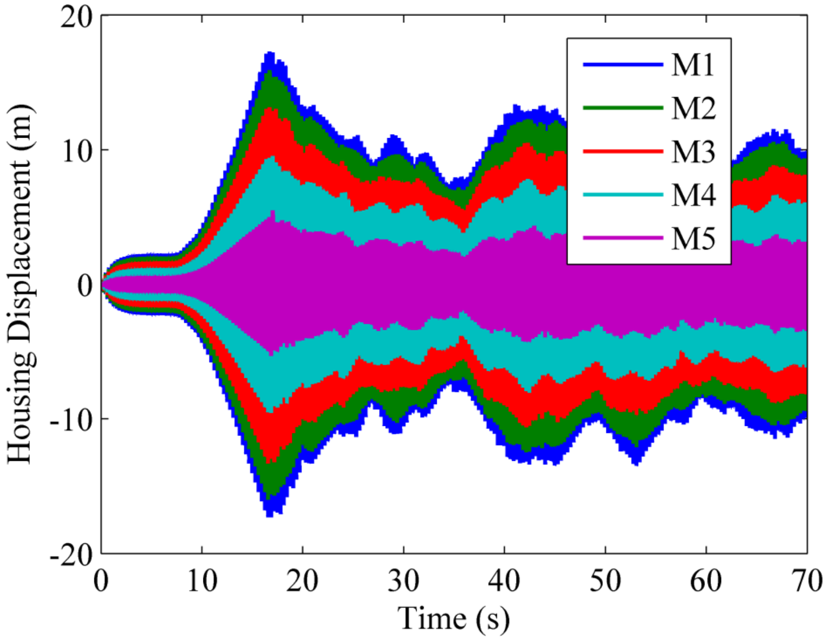

Figure 5.28: Housing displacement for $R_m = 0.9$, $\omega = \omega_{n1}$, $N = 5$, $r_o = 1$m, $\gamma = 5$ Ns/m and Force = 50 N.

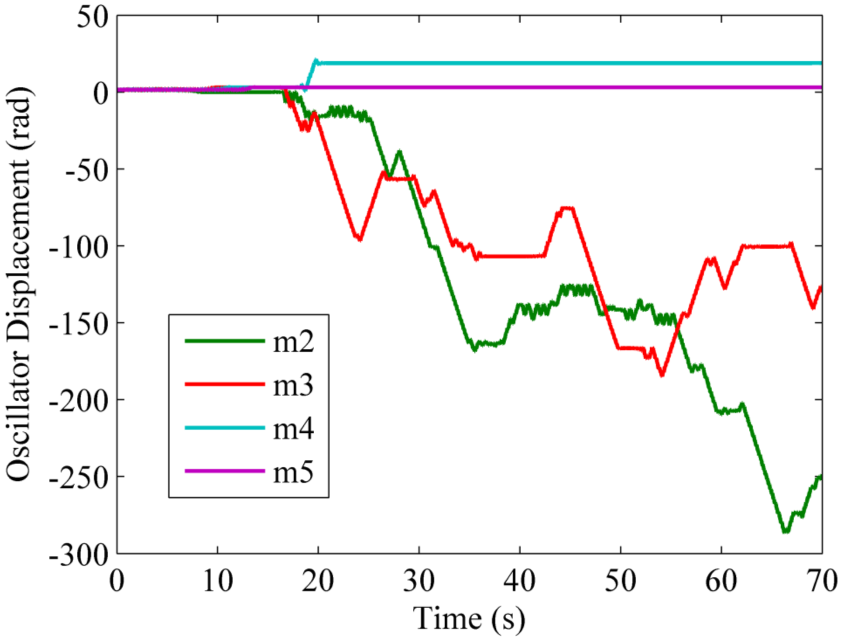

Figure 5.29: Eccentric mass rotation for $R_m = 0.9$, $\omega = \omega_{n1}$, $N = 5$, $r_o = 1$m, $\gamma = 5$ Ns/m and Force =50N.

An example of the Poincaré plot for housing #3 of this system is shown in Figure 5.30. The figure is generated via 1800 forcing cycles of the system. All housings have a similar Poincaré section, corresponding to the time instants $t_n = 2\pi n/\omega$ When looking at a figure of this nature, ideally, the sequential points in the Poincaré mapping would converge after some transient time. This would correspond to so-called period-1 motion, which is the simplest steady-state periodic behavior. If the mapping converged to repeated groupings of k points, the motion would be termed period-k motion, indicating that the steady-state response repeated every k cycles of the applied forcing (also termed a kth subharmonic response). In contrast, the Poincaré plot shown in Figure 5.30 does not repeat, even after 1800 cycles of excitation. The diffuse, nonrepeating pattern is behavior typically associated with chaos [65].

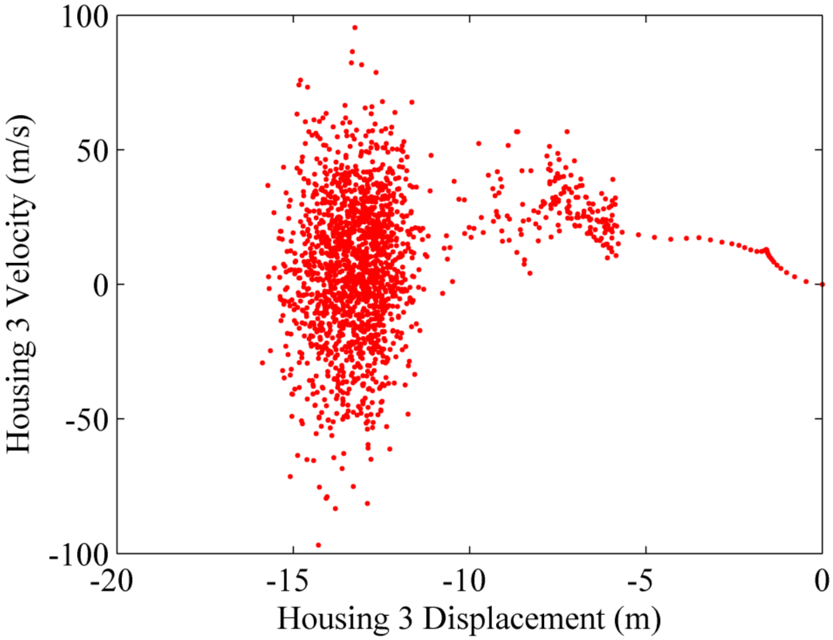

Figure 5.30: Poincaré plot for housing three driven at the first natural frequency. R_m = 0.9, $\omega = \omega_{n1}$, $N = 5$, r_o = 1m, γ = 5 Ns/m and Force = 50 N.

The complex behavior of the housings can be contrasted with the response of the rotating eccentric masses. In Figure 5.31, the 2nd rotating eccentric mass undergoes large oscillations and never seems to settle down to a value. It does exhibit regions of attraction between: 0, π, -π; however, never settles to a velocity of zero in the 1800 cycles considered. Again, the diffuse quality of the Poincaré plot shown in Figure 5.31 is indicative of chaos.

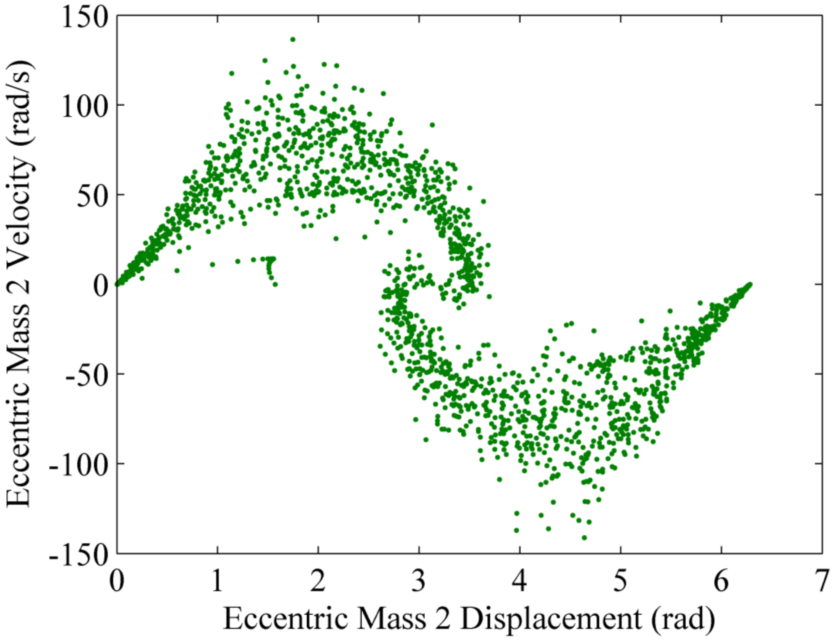

Figure 5.31: Poincaré plot for rotating eccentric mass second driven at the first natural frequency. $R_m = 0.9$, $\omega = \omega_{n1}$, $N = 5$, $r_o = 1$m, $\gamma = 5$ Ns/m and Force = 50 N.

The complex behavior of rotating eccentric mass #2 can be contrasted with the movement of rotating eccentric mass #5 shown in Figure 5.32. As the Poincaré plot indicates, there is a transient portion for the response of the rotating eccentric mass; however, after some time, the movement settles down and the rotating eccentric mass converges to a position value of π ($-\pi$) and a velocity of 0. Therefore, the rotating eccentric mass never deviates from its location and remains fixed for the remainder of the investigation. It is interesting that the system can support chaotic and non-chaotic oscillations in the same response depending on which variables one considers. This is especially surprising because all degrees of freedom in this system are coupled, albeit some only lightly.

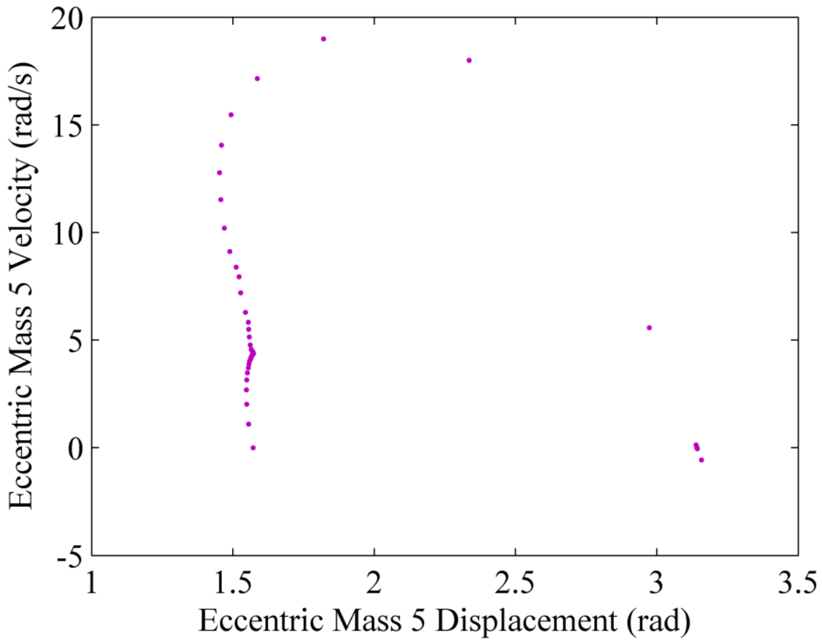

Figure 5.32: Poincaré plot for rotating eccentric mass five driven at the first natural frequency. $R_m = 0.9$, $\omega = \omega_{n1}$, $N = 5$, $r_o = 1$m, $\gamma = 5$ Ns/m and Force = 50 N.

5.6 Inclusion of Gravity in Shock Response

As shown in the previous sections, the lack of gravity in the system can result in the rotating eccentric masses coming to rest at values of 0, π, or $-\pi$. Once a rotating eccentric mass has come to rest at an angle aligned with the mount, it is no longer excited by the translational movement of the housings. Since the only form of damping in the system is based on the movement of the rotating eccentric masses, it is advantageous to keep them in motion. This ensures that attenuation occurs in shock transmission and that the mount has protection against resonant excitation. Another important consideration is that the mount "resets" so that it is ready for the next disturbance that might occur. One way to accomplish this is through use of an elastic torsional spring which resists movement of the mass away from the angle of π/2. However, this results in additional potential energy being stored in the mount, which invariably will be released at a later time. A slightly better option is to allow gravity to act on the masses in the manner of a pendulum. Similar to the torsional spring, the gravitational moment acts as a rotational spring to ground. But unlike the torsional spring, the gravitational moment does not continue to accumulate potential energy if the angle goes through a full 360^{O} rotation. In this section, it will be assumed that the orbits of the eccentric masses is in the vertical plane, however, the influence of gravity can be reduced if the mount is rotated so that the plane of the mass' orbit is inclined away from vertical.

To include gravity in the equations of motion of the system, Lagrange's method can be applied with the inclusion of gravitational potential in the potential energy function. The result is to add a gravitational moment for each angle θ in the form:

$$Q_{\theta} = -mg\hat{\jmath}\frac{\partial \vec{r}_B}{\partial \theta} \tag{5.12}$$

where $\vec{r}_B$represents the location of the rotating eccentric mass and where gravity is assumed to act in the negative $\hat{\jmath}$ direction. With this inclusion, equation (5.4) now becomes:

$$\ddot{\theta}_i = \frac{m\dot{\theta}_i^{\,2} cos\theta_i sin\theta_i}{(M+m)*\left(1-\frac{m}{M+m}sin^2\theta_i\right)} + \frac{k\Delta X_i sin\theta_i}{r_o*(M+m)*\left(1-\frac{m}{M+m}sin^2\theta_i\right)} - \frac{gcos\theta}{r_o*\left(1-\frac{m}{M+m}sin^2\theta_i\right)} - \frac{\gamma\dot{\theta}_i}{m*\left(1-\frac{m}{M+m}sin^2\theta_i\right)}$$

$$\ddot{x}_i = \frac{-r_o\gamma\dot{\theta}_i sin\theta_i + mr_o\dot{\theta}_i^{\,2} cos\theta_i + k\Delta X_i - mgcos\theta sin\theta}{(M+m)*\left(1-\frac{m}{M+m}sin^2\theta_i\right)} \tag{5.13}$$

In the case of gravity, all of the initial angles, θ, for the rotating eccentric masses are 3π/2.

Figure 5.33 and Figure 5.34 show comparisons for the isolation performance of the mount with and without a gravitational restoring moment. The maximum wall force and the maximum displacement of the first mass are plotted vs the mass ratio, R_m, for a chain of length *N*=5 (4 rotating masses), viscous damping coefficient γ =5 Ns/m, and a unit-energy impulsive load, *E*=1 Nm. Due to the small level of input shock and relatively large amount of damping, the rotating eccentric masses do not undergo significant movement. As such, the influence of gravity has little effect on both the maximum transmitted wall force and the first mass displacement. In contrast, Figure 5.35 and Figure 5.36 show the isolation performance vs R_m for an impulsive loading of energy *E*=50 Nm and a damping coefficient of γ =0.1 Ns/m, which results in large movement of the oscillators. Note that, in contrast to the low-energy impulse, the trends of shock performance with R_m are much more complicated. But it is also evident that one cannot conclude that the shock performance of the mount with gravity is always better or always worse than the non-gravitational case. What is not shown in these curves is the fact that, in the case of gravity, all vibrational energy is removed from the mount and the system settles to the original state of the system with angles θ = 3π/2 (plus or minus some multiples of 2π). Thus the mount passively resets itself for the next disturbance event. In the case without gravity, the system may in fact have lingering amounts of energy if the rotating eccentric masses come to rest at values of 0, π, -π.

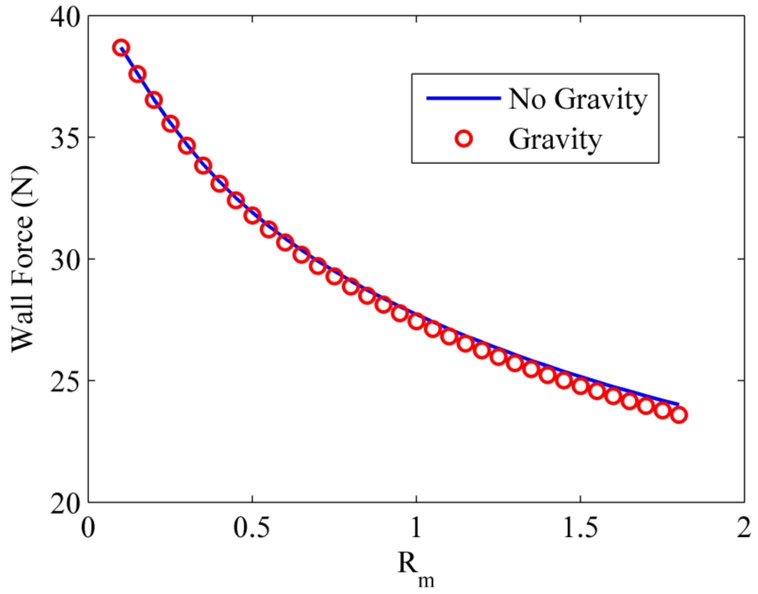

Figure 5.33: Maximum wall force with and without gravity for $\gamma = 5$ Ns/m, $r_o = 0.1$ m , $v_1 = 3.16$ m/s, $N = 5$ and initial energy of 1 Nm.

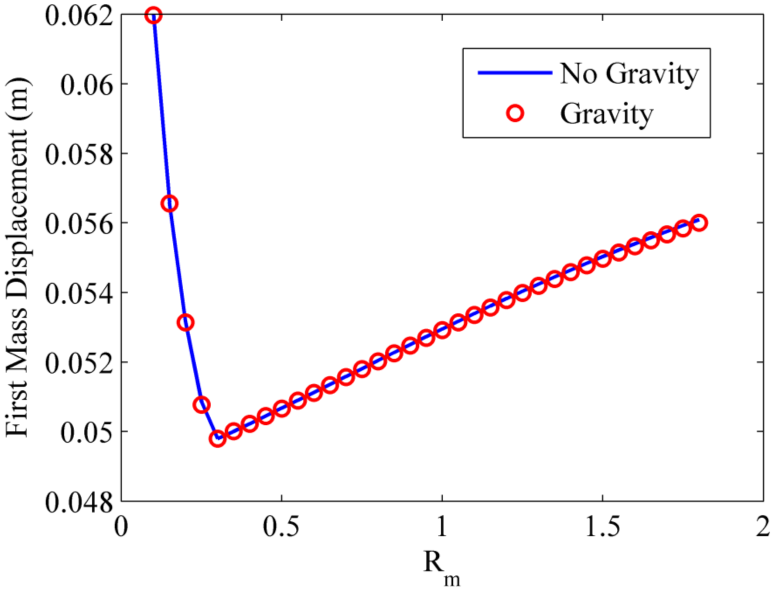

Figure 5.34: Maximum first mass displacement with and without gravity for $\gamma = 5$ Ns/m, $r_o = 0.1$ m, $v_1 = 3.16$ m/s, $N = 5$ and initial energy of 1 Nm.

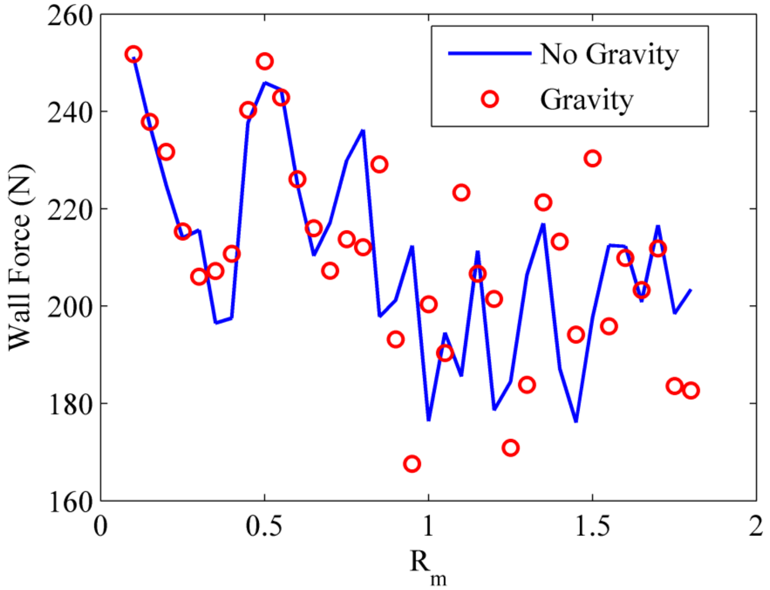

Figure 5.35: Maximum wall force with and without gravity for γ = 0.1 Ns/m, r_o = 0.1 m , v_1 = 22.36 m/s, N = 5 and initial energy of 50 Nm.

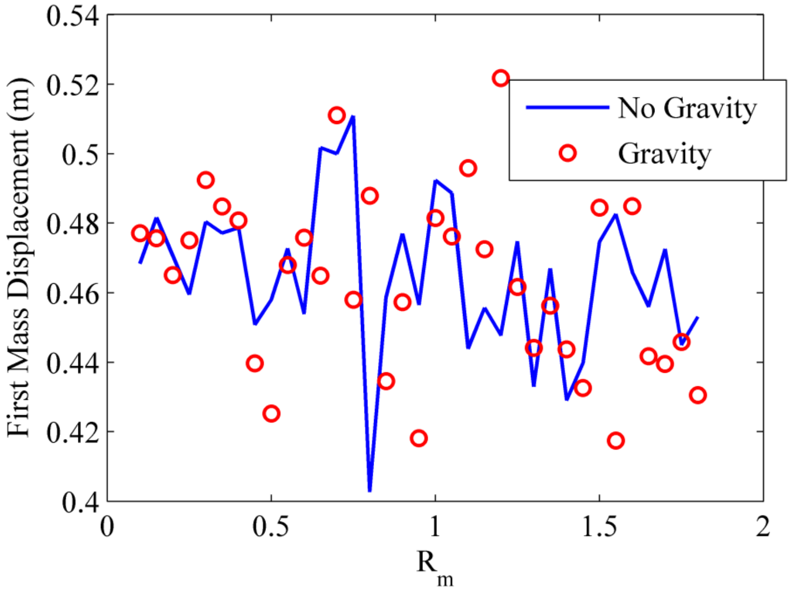

Figure 5.36: Maximum first mass displacement with and without gravity for γ = 0.1 Ns/m, r_o = 0.1 m , v_1 = 22.36 m/s, N = 5 and initial energy of 50 Nm.

5.7 Inclusion of Gravity – Harmonic Excitation

Through extensive numerical simulations, it was found that the inclusion of gravity in the harmonic excitation case prevents any individual mass from remaining aligned with the mount for long periods of time. As such, every rotating eccentric mass remains in a constant state of motion, which ensures the each rotating mass can dissipate energy at all times. Shown in Figure 5.37 and Figure 5.38 is an example of how a harmonic force of amplitude 16 N, which previously caused resonant growth in the system without gravity (Figure 5.26, Figure 5.27), no longer exhibits the resonant growth if gravity is included.

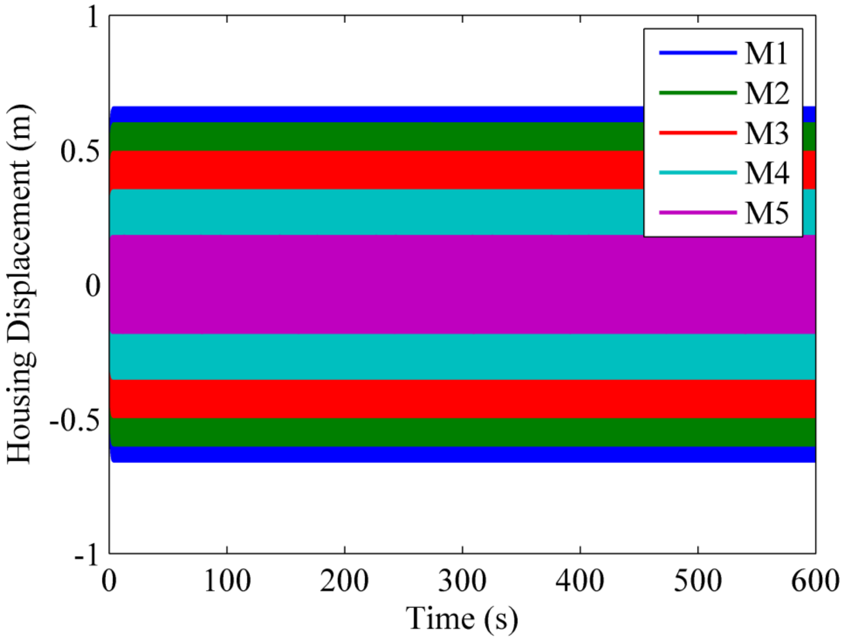

Figure 5.37: Harmonic excitation of system with gravity – housing displacements. Five mass system with r_o = 1 m, γ = 5 Ns/m and Force = 16 N.

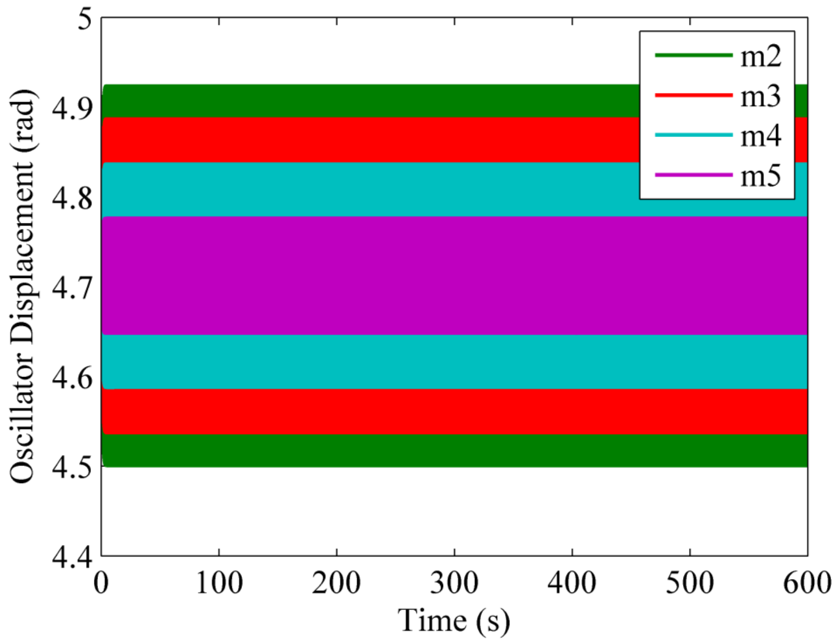

Figure 5.38: Harmonic excitation of system with gravity – oscillator displacements. Five mass system with $r_o = 1$ m, $\gamma = 5$ Ns/m and Force = 16 N.

5.8 Conclusion

The performance of an isolator formed from a series connection of masses and springs was analyzed. All but one mass in the chain consists of a housing or cart and an internally rotating mass - the first mass consists only of a housing. Shock mitigation was accomplished through two different mechanisms. Translational energy was transferred into rotational energy of the internal masses. Then, the rotational motion was dissipated via viscous damping of the relative motion of the internal masses. The internal masses investigated initially did not have any elastic restraint, so there was no tuning of the internal resonances to the vibration modes.

The performance of the isolators was studied numerically by considering various system parameters and initial conditions. Some of the key parameters that were varied were the ratio of the internal masses to the housing mass, the radius of the circular track that guided the internal mass, and the viscous damping coefficient between the internal mass and the track. Also varied was the initial angle of the internal masses. Surface plots (two-dimensional projections) were generated that showed how the transmitted force and first mass displacement changed as a function of the mass ratios and the initial angle of the internal masses.

Several general trends were observed. First, it was seen that as the ratio of the internal masses to the housing mass was increased, shock isolation generally improved. However, in the case of harmonic excitation this resulted in an increase in the transmitted force in the high frequency domain, which is undesirable. It was also seen that favorable initial angles were in the vicinity of 90^{o}. This initial angle led to the highest level of rotation from a given translational disturbance. As the number of masses in the chain increased, the level of attenuation for shock loading increased, even with the overall mass and static stiffness of the isolator mount held constant. Low levels of damping led to substantial amounts of rotation and rotation rates for the internal masses, which in turn gave rise to unpredictable reaction forces at the wall. In certain circumstances, the rotating eccentric masses would fall into convergence regions that would align them with the forcing direction and thus no longer provide damping into the system. This issue was remedied with the inclusion of gravity and showed that the resulting shock response was not significantly changed with the introduction of gravity.

The complex motion of the rotating eccentric mass was further studied in a single degree-of-freedom system with prescribed housing motion. It was found that, based on the initial conditions for the angle and angular velocity, and based on the system parameters, the rotating mass could experience highly complex motion that would either continually rotate or converge to a specific value. Convergence was defined as either small or no oscillation about an angle. Chains of the system were then harmonically excited and it was shown that for small mass ratios the nonlinear system behaved very similar to the linear system. However, as the rotating eccentric mass became larger relative to the housing mass, linear chains could outperform the harmonic response of the nonlinear chains.

CHAPTER 6.

OPTIMIZATION OF ISOLATION CHAINS

6.1 Overview

The focus of previous chapters has been to examine isolator performance of mounts having explicit or implicit symmetry and structure. This greatly reduced the parameter space for improvements, by requiring that many springs, masses, or dampers have specific values and specific relationships to one another. Thus, whether linear or nonlinear, the isolator chains were composed mostly of repeated or periodic cells. Such a repetitive pattern makes a lot of sense when applied to infinite or semi-infinite chains, but in the presence of boundaries, the finite-length isolator chains often behave in surprisingly different ways than expected.

In this chapter, the parameter space for design is greatly expanded to consider mounts for which the individual masses, springs, and/or damping are selected through an optimization process. It is still very important to constrain the mount design so that realistic and practical mounts are developed. But by expanding the parameter space, it is seen that significant improvements in mount performance can be achieved. The chapter begins with a discussion of the optimization algorithm selected for use. It then applies the optimization algorithm to the translational chains, which are no longer restricted to be dimer chains. The chapter next focuses on the small-rotation chains studied in Chapter 4. The chapter concludes with a brief discussion of optimization in the isolator chains having internal rotating masses.

6.2 Discussion of the Optimization Algorithm

There are many different optimization algorithms with each routine having various features making it well suited or poorly suited to particular applications. They all share common attributes, such as the fact that almost all optimization routines use an iterative process to achieve a minimum of some function called a “cost function” or “objective function.” The objective function used in the optimization process is composed of mount stroke, x_1, and transmitted wall force, F_w:

$$Cost = \rho F_w + (1-\rho) k_{eff} x_1 \tag{6.1}$$

where ρ is a unitless parameter that is used to adjust the influence of the wall force vs stroke in the cost function. As ρ varies from 0 to 1, the cost weights the wall force more and more relative to the stroke. Because the magnitude of the stroke is much less than the wall force, the stroke in equation (6.1) is multiplied by k_{eff}, the effective static stiffness. After evaluating a particular design point (or several design points), the next iterate is chosen in a manner that hopefully improves incrementally on the previous designs. For example, gradient based routines use the local slopes of the cost function to move “downhill” from step to step, with the hope of converging to the lowest point on a “valley.” One of the most challenging aspects of optimization problems is to know whether the converged minimum is the true minimum, or just a “local minimum;” perhaps another minimum exists that is even better than the obtained solution.

Another aspect of optimization problems is the fact that practical limitations exist and impose constraints on the design variables. Sometimes, the cost function can be modified to incorporate system constraints, such as the case here:

$$Cost = \rho F_w + (1-\rho) k_{eff} x_1 + w_1 \left| M_{total}^{*} - M_{total} \right| + w_2 \left| k_{eff}^{*} - k_{eff} \right| \tag{6.2}$$

The parameters w_1 and w_2 are large positive constraint penalty weightings scaled to allow only smaller than 0.5% deviation from the target mass and stiffness (k^*_{eff} = 200 N/m and M^*_{total} = 21kg). Deviations from the target mass and stiffness carry a significantly larger cost than wall force or stroke, thus constraining the system. The terms k_{eff} and M_{total} represent the current static stiffness and total mass on the current value of the optimization parameters. In other cases, constraints are handled outside of the cost function. In the case of smooth cost functions and simple constraints, minimization of the cost function is straightforward and reliable. However, when the cost function is complicated and has numerous local minima, it is quite challenging to find the global optimum of the system. As shown below, the dynamic mounts considered in this thesis are characterized by having cost functions that have numerous local minima, making their optimization very difficult.

Simulated annealing [66] is a probabilistic technique for obtaining the global optimum of a given function. A benefit of the algorithm over gradient descent methods is that the initial guess does not necessarily need to be near the global minimum due to the algorithm's willingness to accept a "worse" solution in the process of ultimately finding the best solution. For example, Figure 6.1 shows a one dimensional cost function having several local minima and one global minimum depicted as point 5. A gradient-based algorithm starting at point 1 would most likely take a series of small steps to move downhill and converge to point 2 in the figure. However, simulated annealing algorithms are designed to be able to move "uphill" in the initial phase of the optimization, for example being capable of moving from point 2 to point 3 in Figure 6.1. This “metaheuristic approach” allows for a more extensive search for the optimal solution [67].

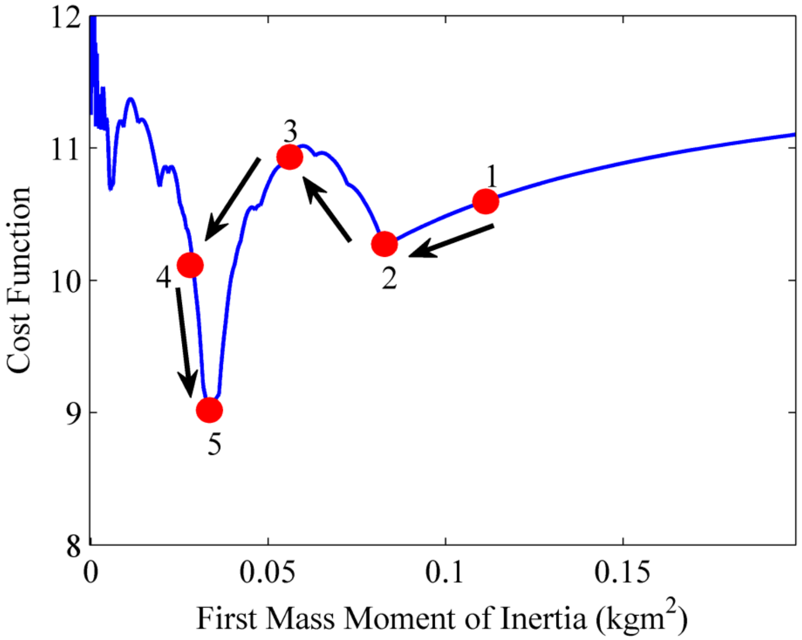

Figure 6.1: Example optimization path for simulated annealing.

The simulated annealing algorithm progresses by moving from one solution to a neighboring solution if either of the two conditions is met:

$$cost(x_{i+1}) < cost(x_i) \tag{6.3}$$

or

$$exp\left[\frac{-cost(x_{i+1})+cost(x_i)}{T}\right] > rand(0,1) \tag{6.4}$$

where x_i and x_{i+1} are the current and next trial solution vectors respectively, rand(0,1) is a random number between zero and one, T is the temperature parameter, and *cost* is the cost or objective function. Similar to a physical, metallic annealing process, the temperature determines the allowance of a worse solution being selected as the new current solution. As the iterations proceed, the temperature is gradually lowered, which reduces the probability that the algorithm will accept worse solutions, allowing it to converge on a global minimum. The cooling schedule, the function that decreases the temperature distribution for the optimization parameters, used in this paper is an exponential model:

$$T_{new} = T_o \gamma^i \tag{6.5}$$

where i is the iteration number and γ is a constant, in this case taken to be 0.99. The algorithm terminates when neither equation (6.3) or (6.4) can be satisfied. If the cooling schedule is slow, the chance at determining the global minimum is increased at the expense of, perhaps, taking more iterations and computational effort. Alternatively, a "re-annealing" option can be introduced to raise the temperature and begin a large region search.

Proper selection of the initial temperature, T_o, is required to ensure the optimizer searches through a significant portion of the parameter space. Initially, T_o was determined based on differences in costs between the initial guess, x_o, and neighboring solutions as given by:

$$T_o = \frac{1}{N}\sum_{i=1}^{N}\left|cost(x_o) - cost(x_{r,i})\right| \tag{6.6}$$

where $x_{r,i}$ is a random neighboring solution and N is the number of solutions used to determine T_o, generally N was taken to be 10 solutions. Consequently, this led to very high initial temperatures, which allowed the algorithm to search massive portions of the domain of possible solutions to find a minimum. Once an optimized solution was found using the simulated annealing algorithm, validation runs were performed.

Due to the difficulty of ensuring that a true, global minimum has been obtained, various methods were used to validate optimized outputs as good approximations to the global minimum. Cost function plots, such as the one displayed in Figure 6.1, were used to help establish good initial guesses. Bounds were sometimes refined for certain parameters if the minimum was known to exist in a smaller interval. This was especially convenient to do due to the odd scaling nature of the problems (i.e. very high stiffnesses, small masses) and their proximity to zero. Sometimes the bounds of a problem could vary over several orders of magnitude, but optimized values generally fell within much smaller ranges.

6.3 Essentially Nonlinear Cubic Chain Optimization

Simulated annealing optimization was applied to the performance improvement of the dimer chains discussed in Chapter 2. Presented below is a study performed for shock excitation of an essentially nonlinear cubic chain of seven masses with total mass of 21 kg and a static stiffness of 200 N/m. The lower bound on all the masses is 5% of the total mass with an upper bound on all the masses of 80% total mass. The input excitation is an impulsive load applied to the first mass such that a specified amount of initial energy was imparted to the system; initial energy E=1 Nm. Note that this differs from the work presented in Chapter 2 where the input was a unit impulse excitation. The level of damping was chosen to be 1 Ns/m, which was done to limit the reflections in the system while still ensuring that the system was lightly damped. The numerical simulations were performed in Matlab and utilized ode45.

The algorithm was tasked with minimizing the size of the first peak in the force transmitted to the wall. While this could miss higher forces that may develop later, previous experience with the system with this level of damping revealed that this was a reasonable way to limit the amount of computational effort while still focusing on the vibratory aspects of the dynamic mount design. In this initial optimization study, only the values of the masses were used as design variables. It was found that the final solution for the masses was: 1.05, 4.14, 1.90, 7.27, 1.13, 3.50, 2.00 kg, which led to a wall force of 125 N. In contrast, if the dimer-structure is imposed as an additional constraint such that the ratio of consecutive masses is given as ε, the minimal wall force for a seven mass chain is 333 N, which occurs for $\varepsilon = 0.42$. Thus, the optimized chain manages to reduce the wall force to approximately one third of the result that was only optimized with respect to the mass ratio.

One of the most telling reasons why the optimized system outperforms the ratio based, dimer-chain system can be drawn from the energy, time, and element number plots. Shown in Figure 6.2 is the best case wall force transmission for the ratio driven mass assignment approach. As shown, there is still a primary pulse of energy that propagates along the chain. Figure 6.3 shows the alternative design which allows the masses to be chosen in a more general manner. The figure shows that almost all the energy is trapped in the first half of the chain due to the optimization of the system.

To verify the robustness of the optimization, a sensitivity analysis was performed. Each mass in the system was changed by +5% and -5% (note: this violates the total mass constraint) to see how the first peak of the wall force would change. Figure 6.4, shows the peak wall force as the mass values are independently varied by 5%. The blue circles give the wall force resulting from a 5% increase in each mass and the red circles give the wall force resulting from a 5% decrease in each mass. It is seen that increases in some

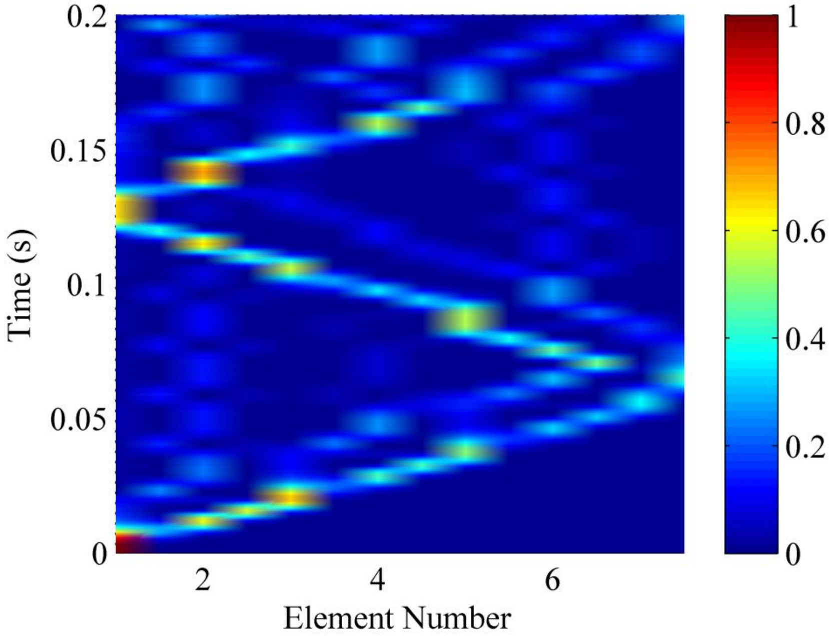

Figure 6.2: Energy, time, element number plot for a seven mass chain of 21 kg, static stiffness of 200 N/m and mass ratio of 0.42.

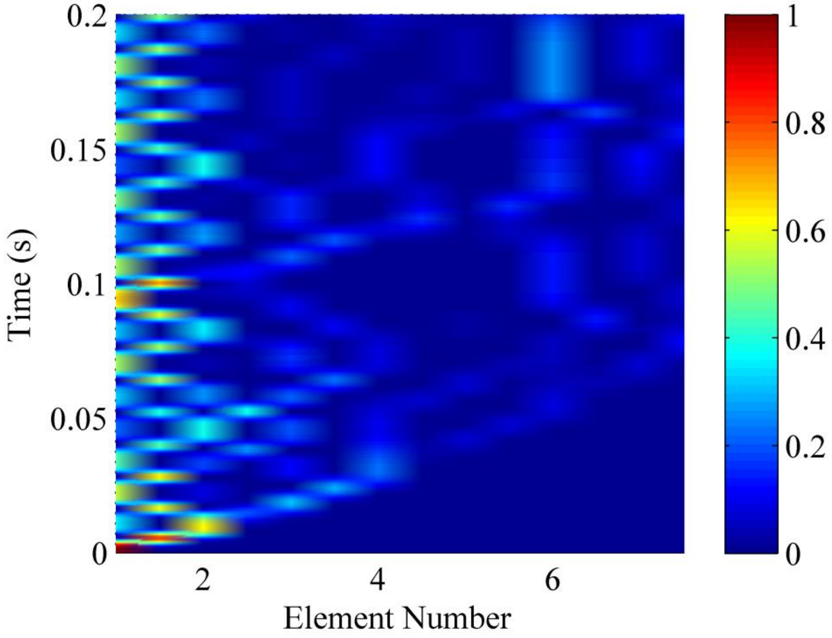

Figure 6.3: Energy, time, element number plot for an optimized seven mass chain of 21 kg, static stiffness of 200 N/m.

masses increase the wall force and others decrease the wall force, but all changes are very small, with the largest change in the wall force being only 1%. Thus, this shows that the optimization is robust in regards to imperfections in the design such as manufacturing tolerances for such a mount. No investigation into the spring coefficients was performed due to the desire to satisfy the static stiffness constraint and to preserve the essential nonlinear characteristic of the system. However, it would be interesting to see if inclusion of a linear part of the spring function results in further improvement.

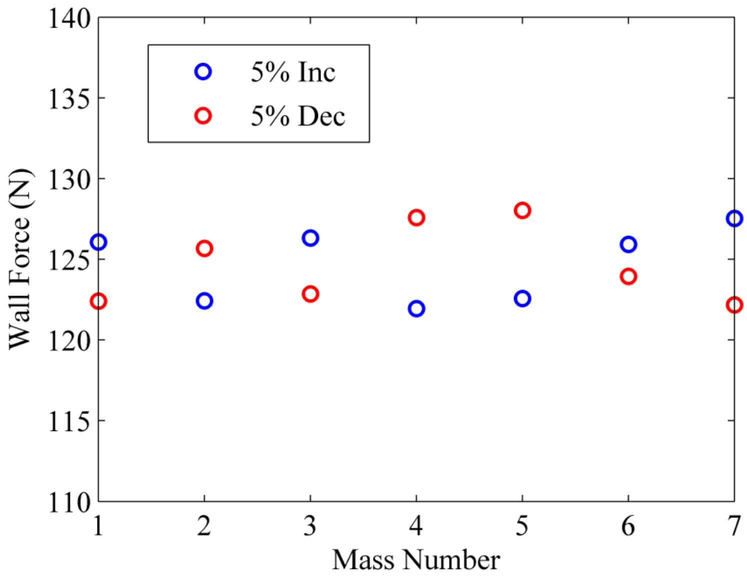

Figure 6.4: Sensitivity analysis of the wall force for +/- 5% adjustment to each mass for the purely cubic system.

An optimization study was also performed using a cost function that consisted of the magnitude of the first mass' displacement, *cost* = abs(x_1). For the seven mass system considered above, the simulated annealing technique found that the minimum first mass displacement was attained for a system having all masses equal. While somewhat a surprising result, giving all masses 1/7 of the total mass resulted in the first mass displacement being 0.0074 m. Figure 6.5 shows the displacement of the first mass versus time. As shown in the figure, the displacement is similar to a square function, which often occurs when maximum values are extremized [68].

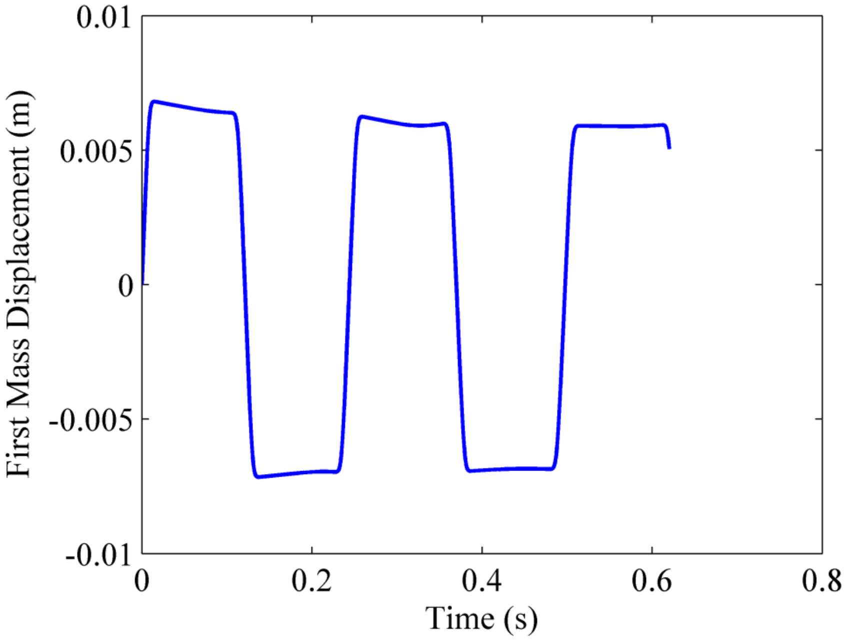

Figure 6.5: First mass displacement of optimized essentially nonlinear chain of seven masses.

6.4 Optimization of Linear Small Rotation Chains

The simulated annealing technique was applied to the problem of isolation performance optimization for the chain of two degree-of-freedom masses undergoing translations and small rotations [69]. This system was discussed extensively in Chapter 4 for a simplified architecture in which the mass-inertia-stiffness parameters were either equal or alternated in a dimer fashion. In order to facilitate the optimization procedure, the system of equations were first recast into a different form due to convenience. The APPENDIX gives a full derivation of this approach, which results in all of the mass, inertia, and stiffness parameters being easily partitioned in the form of diagonal matrices. This form for the equations is convenient, but is not essential for application of the method.

The performance metrics of greatest importance are the displacement of the first mass and the transmitted wall force of the mount. These quantities can be combined into a cost function. But prior work showed the importance of constraining the mounts to have prescribed values for the overall mass and static stiffness. This prevents the optimization process from producing impractical and undesirable designs having very high mass and/or very low stiffness. Within the context of optimization this can be accomplished by adjoining the constraints on mount mass and static stiffness to the cost function using a penalty method, equation (6.2).

Numerical simulations of the isolator response were performed using Matlab's *initial* command. In order for efficient optimization and system constraints, bounds were imposed on mount parameters as shown in Table 6.1. The lower bound on the first mass offset, *d*, was selected due to the way the simulated annealing algorithm chooses neighboring solutions. Neighboring solutions are chosen by searching within a percentage of the current value. If the lower bound on *d* is set at zero, the algorithm could select zero for a single iteration. If this were to occur, all the subsequent iterations would result in a value of *d* equal to zero, and the optimization process could stall at a suboptimal point. Eventually, the optimized rotational system will be compared to an optimized non-rotational linear system. The upper bound on *d* is chosen to be equal to *L*, which is the offset attachment location of all the subsequent springs. The damping model chosen is modal damping, which can be expressed in terms of modal damping ratios and

Table 6.1: Bounds used for optimization of small rotational system.

Parameter	**Lower Bound**	**Upper Bound**
First mass offset, d (m)	0.001	0.1
First mass, m_0 (kg)	4.2	16.8
Mass 1-N, m_1-m_N (kg)	1.05	16.8
Mass moments of inertia: 1-N, J_1-J_N (kgm^2)	0.0005	1000
Spring Stiffness, s_1-s_N, k_0-k_N (N/m)	50	100000
Damping Ratio, ζ	0.009	0.01

the mass-normalized modal matrix, [Φ]:

$$[C] = [M][\Phi][2\zeta\omega_n][\Phi]^T[M][\Phi] \qquad (6.7)$$

Unless otherwise stated, the damping ratio on each mode is equal, which adds a single damping parameter to the design vector. As done previously, the damping is initially limited to a small value due to the trade-off in high frequency isolation as damping is increased. The bounds on the masses, mass moments of inertia, and spring stiffnesses shown in Table 6.1 were set far apart to ensure the optimizer searched through a wide range of possible parameter combinations. The bounds are not meant to reflect a practical design limitation, but to allow solutions which demonstrated the influence of adding rotation into the system. It should be noted that the design parameter vector for this system is fairly large. Counting all of the parameters listed in Table 6.1 the total size of the design vector is 4N+4, where N represents the number of rotating masses.

During the process of optimization, thousands of different parameter combinations must be simulated. In each simulation, the maximum wall force and stroke must be determined from the time response of the system. As previously discussed, determining the maximums for very lightly damped systems is not straightforward. Thus, for efficient optimization, simulation durations are defined by the amount of time necessary for the response of the system's slowest vibratory mode (first natural frequency) to decay to 2% of its initial amplitude. Durations are calculated by:

$$T_S = \frac{4}{\zeta \omega_1} \tag{6.8}$$

where ω_1 is the slowest natural frequencies (rad/s) of the system. To prevent aliasing, the sampling rate is also based on the system's natural frequencies. The sample rate for any system is eight times the highest natural frequency:

$$f_S = \frac{4\omega_{2N+1}}{\pi} \tag{6.9}$$

Where f_S is the sample rate in Hz, ω_{2N+1} is the system's highest natural frequency, and N is the number of rotational bodies.

As discussed in Chapter 4, in the case where the final two springs are equal, the rotation effect cancels out on the wall force. However, in the case in which the last two springs are not equal, the general wall force expression is given:

$$F_W = x_N(s_N + k_N) + \theta_N L(k_N - s_N) \tag{6.10}$$

An example of the wall force and first mass displacement response plots for a 3-mass (1 translational, 2 rotational) optimized system are shown in Figure 6.6 and Figure 6.7.

In order to assess the influence of rotation on the system, a comparison between a system with and without rotation is performed. For the comparisons, the chain length, total mass, static stiffness, and damping were held equal to provide a valid comparison between the rotating and non-rotating systems.

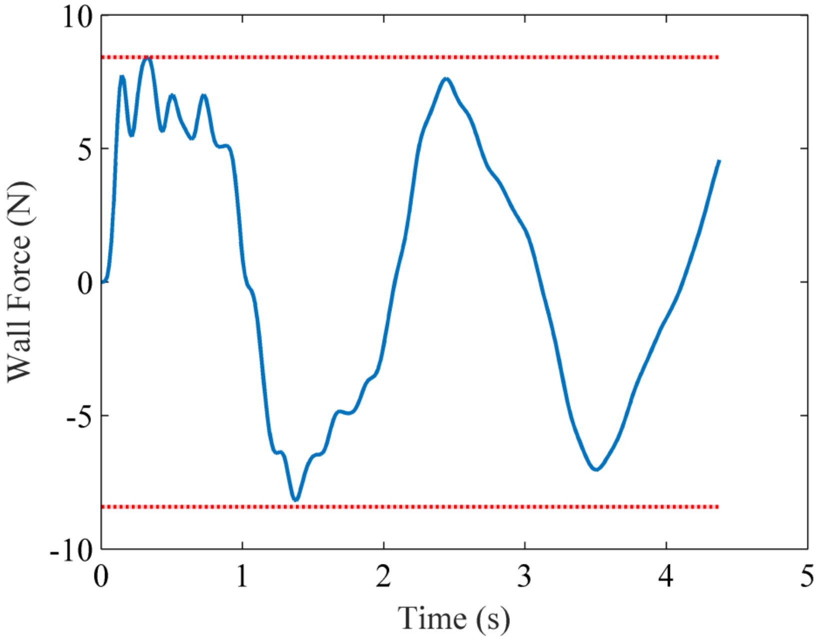

Figure 6.6: Wall force versus time for optimized system with *N*=2.

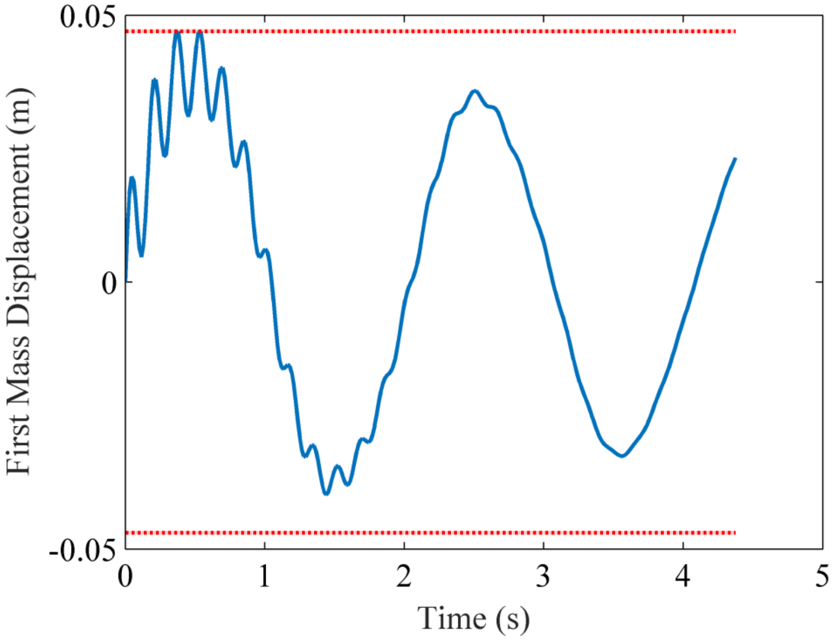

Figure 6.7: First mass displacement versus time for optimized system with *N*=2.

The optimized parameters for a non-rotational mount with two masses (2DOF) are in Table 6.2. The resulting wall force, stroke, and cost are listed in Table 6.3. This system was optimized with $\rho=1$; i.e., cost function only had weighting on wall force and not on first mass displacement.

Table 6.2: Optimized parameters for non-rotational mount with two masses.

Parameter	m_o	m_1	k_o	k_1	ζ
Units	Kg	Kg	N/m	N/m	Unitless
Value	4.2	16.8	10000	200.4	0.01

Table 6.3: Performance metrics for optimized non-rotational mount with two masses.

Result	**Value**
Max Wall Force (N)	8.882
First Mass Displacement (m)	0.045
Cost	8.883

For different chain lengths, optimized non-rotational systems appear to approach the same qualitative solution. That is to say, the system behaves as a single large mass attached to the wall with the softest spring possible when $\rho=1$. As the chain length increases, the springs k_o-k_{N-1} remain relatively stiff, effectively combining the masses, m_o-m_N, into one large mass. This solution makes sense because the system is optimized with an emphasis on only force; a heavy, highly-compliant mount is an optimal solution.

In an effort to improve the isolator performance, internal rotation is introduced into the vibratory response. Rotation in the aforementioned systems can be introduced via two methods: small mass moments of inertia and an offset attachment location, *d*, greater than zero or through unequal springs between the masses. When rotational motion is introduced, optimized designs tend to include significant levels of rotation along the chain. Figure 6.8 shows the amount of rotation for an optimized system with N=2. In this case both masses exhibit small values for the mass moment of inertia and unequal springs between the rotating masses, which results in both rotating masses, m_1 and m_2, exhibiting approximately 15^o of rotational displacement amplitude.

In general, the mass moments of inertia, J_1-J_N, are small in all optimized rotational systems regardless of chain length. Values for the offset attachment location, d, were generally close to zero. An example of the cost function as d is varied is shown below in Figure 6.9. This figure was generated by varying d while scaling spring stiffness to maintain the overall static stiffness constraint; all other parameters were held constant.

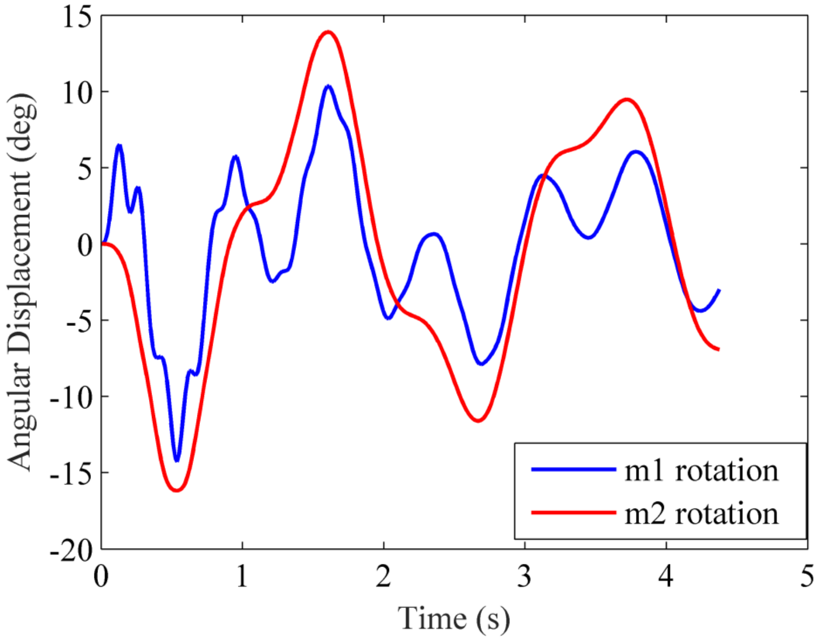

Figure 6.8: Rotation versus time for optimized system with two rotational masses.

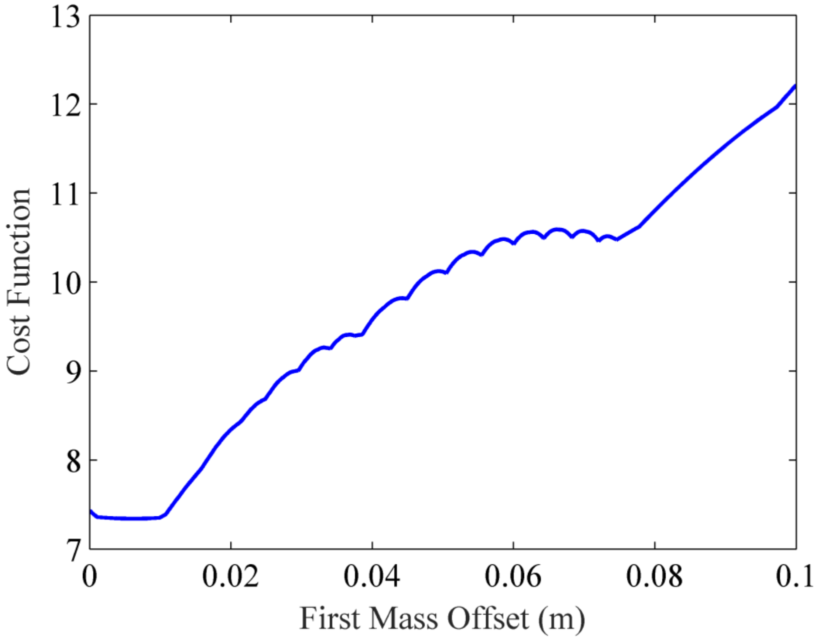

Figure 6.9: Cost function value vs first mass offset attachment location for single rotational mass system.

The plot suggests that the optimum height position for the first mass is very close to the center of the first rotating link. Although the first mass attachment point is near the center of the first rotating mass, differences in the top and bottom spring stiffnesses result in the rotational motion inside the chain. The optimized result suggests that differences in stiffness, not offset attachment location, is the preferred way to generate rotation. Designs with large offsets were within the range of possibilities, but the optimizer determined these were not the most effective solution. This optimization result is influenced by the individual spring stiffnesses associated with the offset attachment location. Recall that as the offset attachment location is shifted, individual springs became stiffer in systems with all the springs equal.

Optimization parameters for a mount with a single rotational mass (N=1), are shown in Table 6.4 for ρ =1. Note the cost is not just the wall force, this is because the actual static displacement of the mount under a 1 N load is 5.019e^{-3} m instead of 5.0 e^{-3} m, which results in an error of less than 0.5% for the static displacement. This amount of error is accounted for in the cost via equation (6.2), resulting in the cost being slightly higher than the wall force component alone.

Table 6.4: Optimized parameters for rotational mount with one rotating mass.

Parameter	m_o	m_1	J_1	k_o	s_1	k_1	D	ζ
Units	Kg	kg	kgm^2	N/m	N/m	N/m	m	Unitless
Value	4.2	16.8	0.034	31192	66.2	198.4	0.001	0.01

Table 6.5: Performance metrics for optimized system with one rotating mass.

Result	Value
Max wall force (N)	7.355
First mass displacement (m)	0.045
Cost	9.062

The results presented above were all optimized only with respect to minimizing the peak wall force. This was achieved by setting ρ =1 in the cost function, equation

(6.2). Studies were also conducted as ρ was varied, changing emphasis from wall force to first mass displacement. Table 6.6 contains the results as ρ is varies for a system with one rotating mass.

Table 6.6: Wall force and stroke as ρ is varied, optimized rotational system with one rotating mass.

ρ	**Wall Force (N)**	**First Mass Displacement (m)**
0.0	124.9	0.0154
0.2	32.9	0.0182
0.4	26.3	0.234
0.6	24.7	0.0295
0.8	15.6	0.0305
1.0	7.33	0.041

The results of Table 6.6 are shown below in graphical representation in Figure 6.10. Also shown in Figure 6.10 is a curve fit using a simple reciprocal function. The results of the transmitted force when compared to the first mass displacement sweep through the classic tradeoff curve. As ρ goes from 1 to 0, some general observations can be made. First, d and ζ remain nearly unchanged. The mass moment of inertia increases as more emphasis is placed on stroke. For ρ =1, the top spring between the last mass and the wall, s_1, is very soft; however, as ρ decreases, the configuration changes to a stiff value for k_o and s_1 and a very soft value for k_1. Because k_1 is very soft, rotation of the first rotational mass could be a significant source of displacement.

The eigenstructure of the system with ρ =0 includes a mode with significant rotation – mode 1 in Table 6.7. However, when the system is excited, mode 2 and 3 provide the most significant contributions to the first mass displacement. Modes 2 and 3 are primarily translational modes. Exciting the translational modes of the system with stiff springs results in a high wall force with a low first mass displacement. The low natural frequency of the first mode also limits its contribution to the first mass

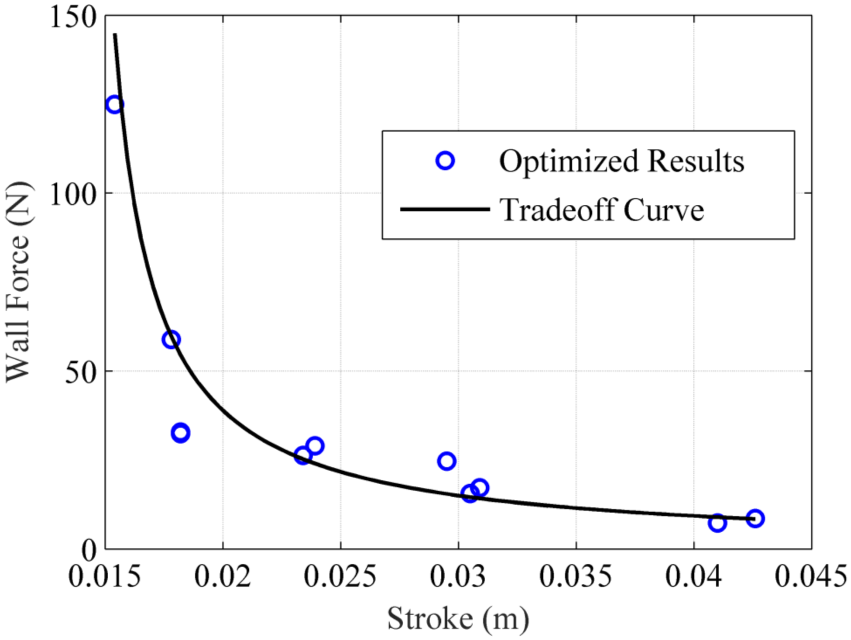

Figure 6.10: Wall force and stroke of optimized systems as ρ varies from 0 to 1.

Table 6.7: Eigenstructure of system with single rotating mass, optimized with ρ =0.

Mode	**1**	**2**	**3**
Frequency (Hz)	0.05	3.15	13.27
x_0	0.0218	0.237	-0.0543
x_1	0.0218	0.107	0.476
θ_1	0.219	-0.0213	-0.0052

displacement. By the time mode 1's contribution to the stroke is at a maximum, the other modes have been significantly damped.

In optimization studies, the sensitivity of the final solution to the parameters is highly important. If a small change in a parameter results in a large change in the performance metrics, the viability of the optimization is significantly reduced. An investigation was conducted to determine the sensitivity of wall force and stroke to variations in the design parameters. This was accomplished by beginning with an optimized system, then applying deviations up to 1% in the design parameters. Changes in individual parameters and changes in all parameters simultaneously were investigated. Note that this approach slightly violates the overall mass and static stiffness constraint. Figure 6.11 shows variations in wall force and stroke due to changes in the spring stiffness k_1 with $\rho=1$.

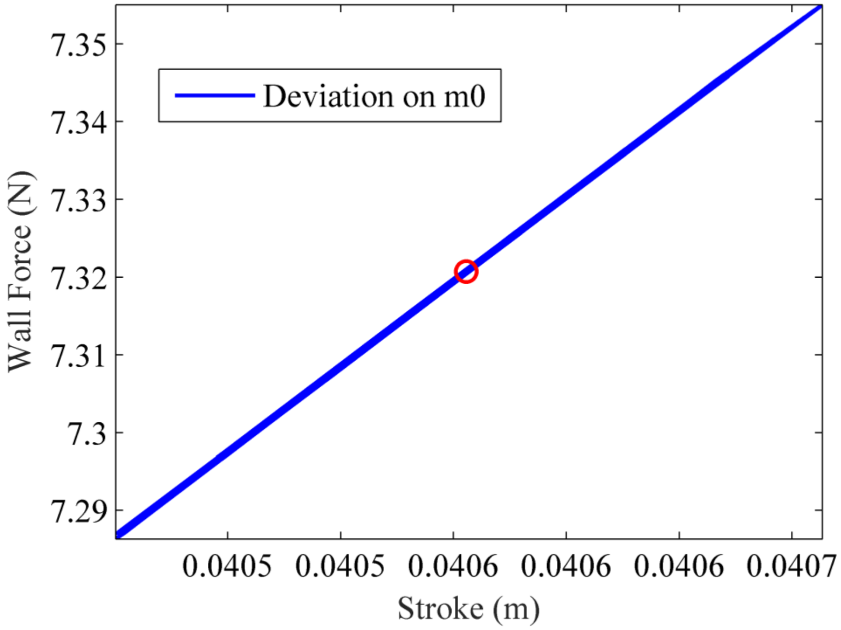

Figure 6.11: Changes in wall force and stroke for $\rho = 1$ system as stiffness k_1 is varied.

Sensitivity analyses were performed on systems optimized with $\rho=1$, 0.5 and 0. Table 6.8 through Table 6.10 lists the results as individual parameters are perturbed. As shown in the tables, 1% deviations in an individual parameter do not greatly influence the system isolation performance. The largest observed change is a 0.64% change in the peak first mass displacement when a 1% change in k_0 is introduced.

Table 6.8: Sensitivity analysis for ρ =1 with 1% variations in individual parameters.

Parameter	m_0	m_1	J_1	k_0	s_1	k_1	ζ	d
Max F_w (N)	7.355	7.327	7.349	7.322	7.337	7.340	7.328	7.321
% Change	0.46%	0.08%	0.38%	0.01%	0.22%	0.26%	0.1%	0%

Table 6.9: Sensitivity analysis for ρ =0.5 system with 1% variations in individual parameters.

Parameter	m_0	m_1	J_1	k_0	s_1	k_1	ζ	d
Max F_w (N)	29.19	29.20	29.05	29.12	29.24	29.06	29.06	29.05
% Change	0.52%	0.54%	0.02%	0.26%	0.69%	0.06%	0.07%	0.02%
Max x_0 (m)	0.0239	0.0239	0.0239	0.0239	0.0239	0.0239	0.0239	0.0239
% Change	0.16%	0.13%	0.08%	0.03%	0.03%	0.05%	0.03%	0.05%

Table 6.10: Sensitivity analysis for ρ =0.0 system with 1% variations in individual parameters.

Parameter	m_0	m_1	J_1	k_0	s_1	k_1	ζ	d
Max x_0 (m)	0.0155	0.0155	0.0154	0.0155	0.0155	0.0154	0.0155	0.0154
% Change	0.32%	0.32%	0.32%	0.64%	0.50%	0.32%	0.39%	0.32%

Figure 6.12 is an example of a sensitivity analysis in which all parameters are varied simultaneously. Each parameter was assigned an individual deviation up to 1%. A Monte-Carlo simulation was run 1,000 times and the results are shown in the plot. Table 6.11 lists the deviation percentages in wall force and stroke for different ρ values.

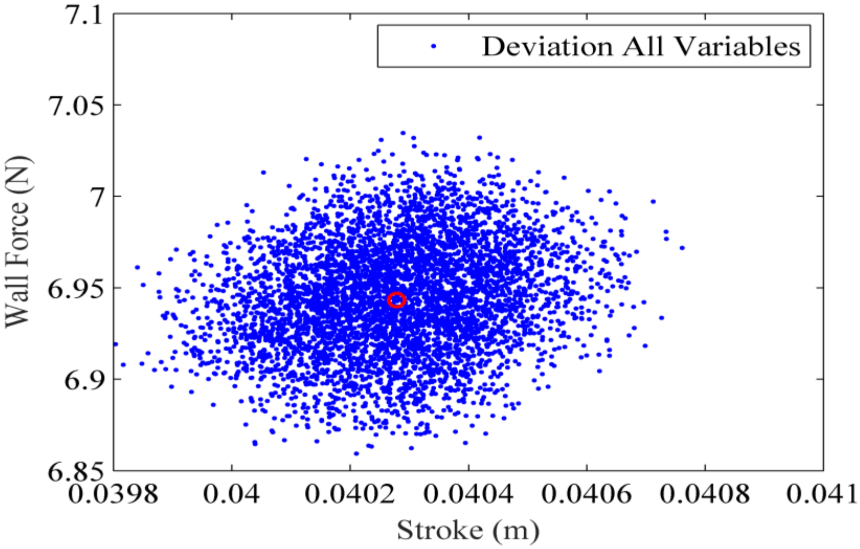

Figure 6.12: Sensitivity analysis on ρ = 1 system with all parameters varying simultaneously by 1%.

Table 6.11: Sensitivity analysis results for varying all parameters simultaneously by 1%.

ρ	F_w **Change (%)**	**Stroke Change (%)**
1	1.3	1.02
0.5	1.84	0.76
0	0.92	0.84

Across all sensitivities studies, the maximum increases in force and stroke were minor, which is a favorable result especially if the system is to be fabricated. The low sensitivities suggest optimized systems are robust to manufacturing tolerances and to unmodeled dynamics.

When isolators were optimized, trends common to rotational and non-rotational systems emerged. The first mass, m_0, was always as light as possible. The damping ratio was always at or very near the maximum value. This is expected as higher damping causes high natural frequencies to die out quickly, limiting their contribution to the maximum wall force. Soft springs were always found at the end of the chain (for a non-rotational system the last spring is soft, for a rotating chain one of the last springs is soft). Soft springs reduce transmitted force but allow more displacement. It was expected that the optimizer would choose the two springs connecting the final rotating mass to the wall to be equal. In this situation, the contribution of the rotation to the wall force would cancel out. However, this was not found to be the case. The reasoning behind this is dependent on the eigenstructure of the problem and further discussed below.

The trend observed in non-rotational systems was that all springs except the last were as stiff as possible. The last spring was always as soft as the stiffness constraint would allow. The system behaved as a large mass attached to the wall by a soft spring. This trend makes sense considering the performance objective of wall force. The equivalent static stiffness constraint determines the lower limit for the stiffness of the last spring. For a system of three springs in series, the equivalent stiffness is:

$$k_{eq} = \frac{k_1 k_2 k_3}{k_2 k_3 + k_1 k_3 + k_1 k_2} \tag{6.11}$$

The trend in optimized, non-rotational systems is that k_1=k_2 and that both are as stiff as possible. Representing k_1 and k_2 as k_{12} and taking the limit as k_{12} approaches infinity yields:

$$\lim_{k_{12}\to\infty} k_{eq} = \lim_{k_{12}\to\infty} \frac{k_{12}^2 k_3}{2k_{12}k_3 + k_{12}^2} \to k_{eq} = k_3 \tag{6.12}$$

The solution to equation (6.12) agrees with the short chains optimized in this chapter. For longer chains lengths, the arrangement of a very stiff springs followed by a soft spring remains the optimum solution as equation (6.12) will produce the same result as more spring terms are added.

As mentioned previously, the goal of introducing rotation to the dynamic mount is to improve isolator performance by converting some of the initial impulse into less harmful rotational motion. Figure 6.12 and Figure 6.13 illustrate the advantages of internal rotation. For chains of equal length, the wall force is reduced (17% reduction) without an increase in stroke (1% reduction), which showcases the superiority of the new isolation mount design.

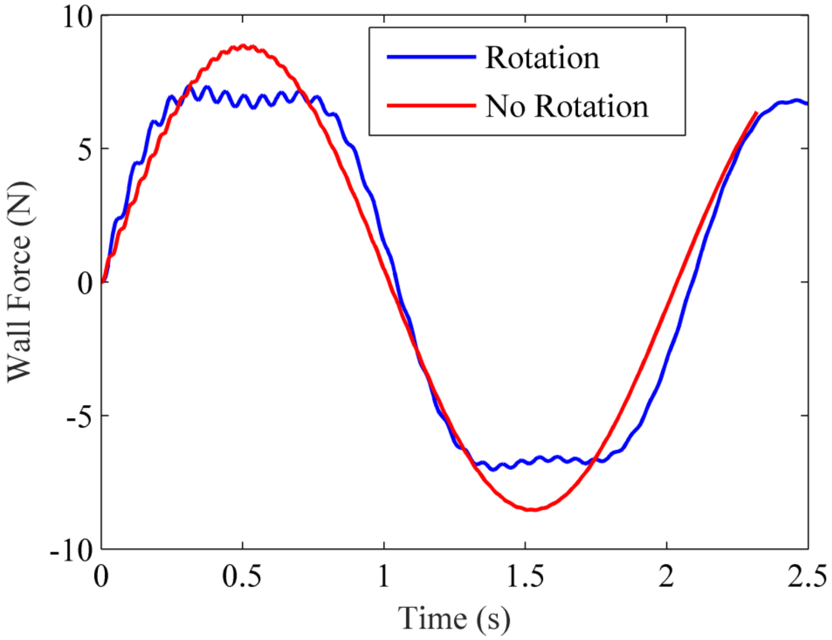

Figure 6.13: Comparison of wall force optimized systems with and without rotation, ρ = 1 and N = 1.

One advantage of mounts with rotation is that they are more effective at utilizing destructive interference between vibrational modes to reduce maximum wall force. A linear system's wall force is a linear combination of the contributions from the system's modes and natural frequencies. The lowest frequency, mode 1, always is the most

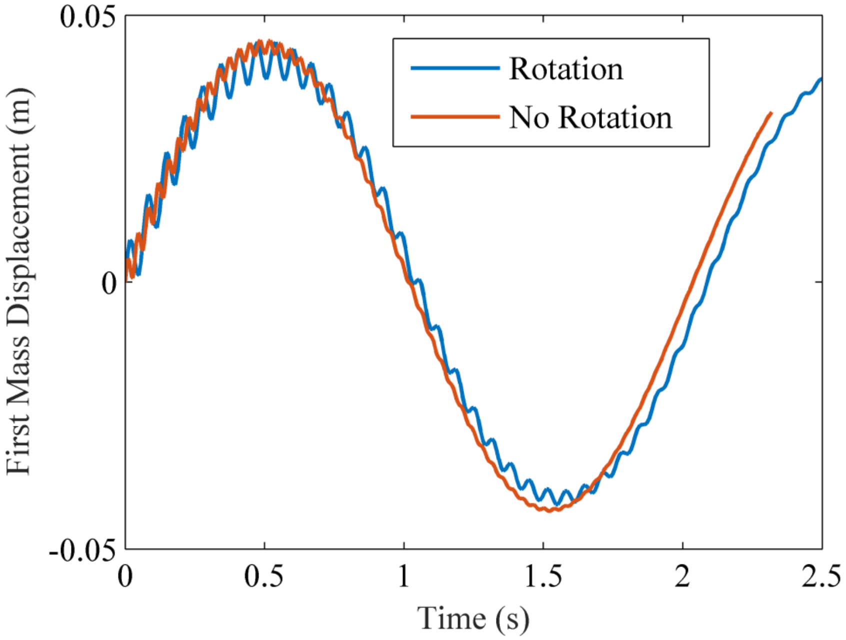

Figure 6.14: Comparison of first mass displacement of optimized systems with and without rotation, $\rho = 1$ and $N = 1$.

significant contributor to wall force in shock events. In optimized systems, parameters are chosen such that the higher modes destructively interfere with the first mode's contribution to the wall force. To showcase this effect, the wall force for the optimized rotational system in Figure 6.13 is broken into modal contributions to the wall force and is displayed in Figure 6.15. In this three degree-of-freedom system, wall force contributions from the first mode are reduced due to destructive interferences with the higher two modes, shown around the 0.5 second time. In fact, the first and second natural frequencies are commensurate with a 1:3 ratio.

The same decomposition can be performed for the system without rotation. The non-rotational system with the same chain length has one less degree of freedom. Interference is much less effective in the non-rotational system as indicated by

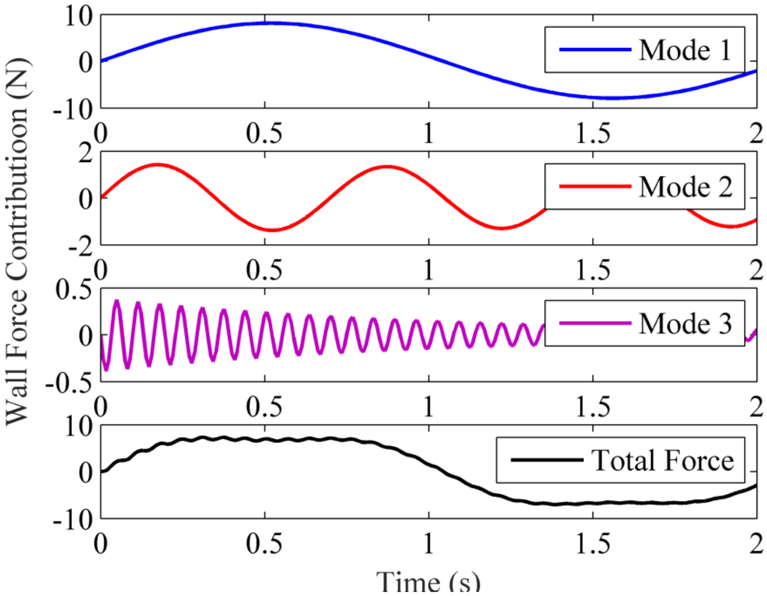

Figure 6.15: Wall force broken into modal contributions, optimized rotational system with $\rho = 1$ and $N = 1$.

Figure 6.16. Mode 2 primarily involves relative translation between m_0 and m_1, with deformation of the very stiff spring between the two masses. As previously noted this deformation is small compared to the overall translation of the two masses. Thus, mode 2 is ineffective at reducing force because the instances when it adds to and subtracts from the first mode are very close together and significantly smaller than the magnitude of mode 1.

The eigenstructure of optimized rotational systems suggests that nodal points at the ends of the structure improve isolator performance. Exciting a system at a nodal location results in that mode not contributing to the wall force – this is because application of a force input to a nodal location does not excite that particular mode. Similarly, if there is a node at the final mass displacement, then that mode will not

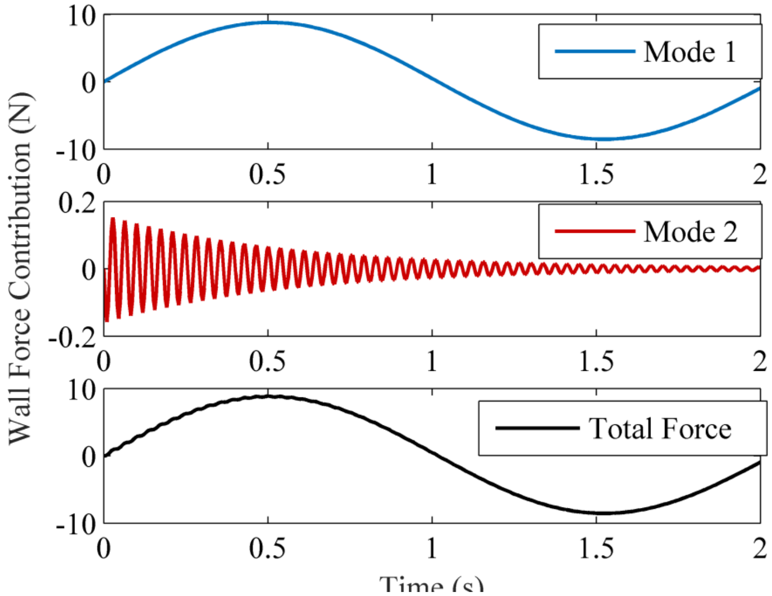

Figure 6.16: Wall force broken into modal contributions, optimized non-rotational system with two mases and $\rho = 1$.

contribute to the wall force. Shown in Figure 6.17 is the Bode plot for the optimized rotational and non-rotational system of two masses with ρ =1. As discussed in Chapter 4, the resulting eigenstructure of the optimized rotational systems indicates a pole-zero cancellation. Comparing the frequency response of the rotational mount with the non-rotational mount, it is shown that the rotational mount's 3rd natural frequency occurs before the 2nd natural frequency of the non-rotational mount, resulting in an increased region of isolation. Recall the rotational system had a 17% improvement in wall force reduction and 1% improvement in stroke reduction for shock excitation.

6.5 Optimization for Isolator Chain Having Internal Rotating Masses

Simulated annealing optimization of a chain of isolators having large-angle, internal eccentric masses discussed in Chapter 5 was also investigated for shock excitation. The goal of the optimization is to see which condition is better: the situation

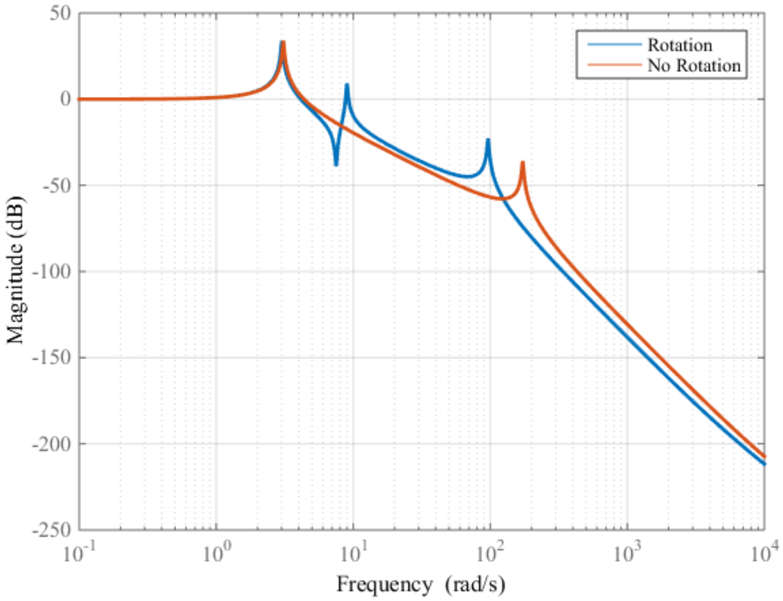

Figure 6.17: Bode plots of optimized rotational and non-rotational systems with two masses, $\rho = 1$.

Table 6.12: Comparison between optimized rotating and non-rotating systems for two different number of masses, $\rho = 1$.

Number of Masses	**Wall Force (N)**			**Stroke (m)**		
	Rot	**NRot**	**% Diff**	**Rot**	**NRot**	**% Diff**
2	7.36	8.88	-17	0.045	0.045	-1
3	8.41	9.76	-14	0.047	0.053	-11

where the rotating eccentric masses make complete rotations or if constraining the system such that only small rotations occur generate better transmitted wall force and first mass displacement results. Previously, the total mass of each housing plus rotating eccentric mass, $M+m$, was equal among the housing elements. Similarly, all the springs in the system were kept the same and variations to the radius of the circular pathway, r_o, and damping, γ, were investigated. An optimization study of a system having N=3 was conducted. The optimization variables were the three cart masses (M_1, M_2 and M_3), the rotating eccentric masses in the second and third carts (m_2 and m_3), three stiffnesses (k_1, k_2 and k_3), the radius of the circular pathway, r_o, and the damping coefficient, γ.

The input applied to the system is an instantaneous change in the velocity of the first mass, where the total energy into the system is maintained as 1Nm, unless otherwise noted. The total mass of the system is 1 kg and the static stiffness of the system is chosen to be 200 N/m (1 N static force results in a first mass deflection of 5 mm). The optimized system has the inclusion of gravity, which is set to 9.81 m/s^2, since it was previously shown that the inclusion of gravity is beneficial to the system. The optimization is guided by the algorithm and results obtained in Chapter 5. That is to say, it is expected that higher levels of damping, γ, will provide greater influence in results than the radius of the circular pathway, r_o. The lower and upper bounds on the system parameters are shown below in Table 6.13.

The goal of the optimization process was to limit the transmitted wall force while maintaining an overall mass and static stiffness of the system. It was found that the level of damping and the radius of the circular pathway were always maximized.

Table 6.13: Lower and upper bounds on large rotational optimization system.

Parameter	Lower Bound	Upper Bound
First Housing (M_1)	20% of total mass	80% of total mass
2nd and 3rd Housing (M_2 M_3)	1% of total mass	80% of total mass
Rotational Masses (m_2 m_3)	1% of total mass	80% of total mass
Springs (k_1 k_2 k_3)	200 N/m	50000 N/m
Damping (γ)	5e-3 kg/s	10 kg/s
Radius of circular path (r_o)	0.05 m	0.5 m

This is due to the nature of the impulsive loading and the ability to remove the largest amount of energy as quickly as possible from the structure. This quick energy removal results in a decrease in the transmitted wall force. While the optimizer did attempt to significantly change the magnitude of the springs, it was shown that this was detrimental to the transmitted wall force and final spring coefficients obtained were found to be less than 1% different from the initial guesses. The sizes of the masses did significantly change from their initial guesses. It was found that large rotating eccentric masses resulted in the best solution. The optimized solution, shown in Figure 6.18, exhibited a decrease in the wall force by 18%. The final optimized system parameters are shown in Table 6.14.

For small levels of damping, the ability for the rotating eccentric masses to completely spin around was possible. However, the optimization routine found that this was not beneficial to the shock isolation problem. In the case of large rotational motion, the reaction forces may constructively interfere at the wall resulting in an increased wall force.

6.6 Conclusion

Discussion of the simulated annealing algorithm and the benefit of the approach over gradient descent methods were discussed. The ability of the simulated annealing algorithm to accept worse solutions based on a gradually decreasing temperature allowed it to overcome pitfalls faced by gradient descent methods. However, this approach is metaheuristic in nature and thus it is not necessarily repeatable.

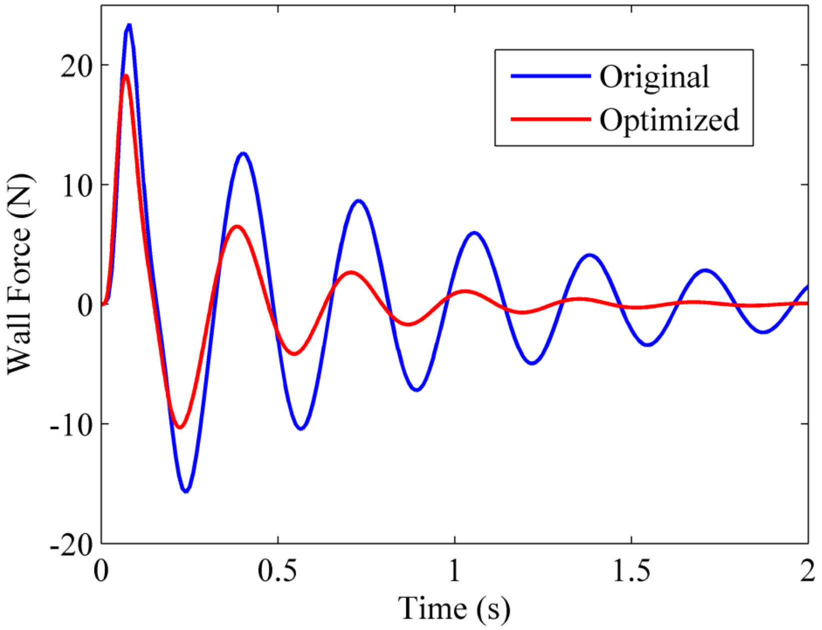

Figure 6.18: Comparison of the original and optimized large rotational system's wall force versus time.

Table 6.14: Optimized values for isolation system with large rotational motion.

Parameter	Optimized Values	Original Values
Housings: M_1, M_2, M_3	0.2557, 0.1325, 0.0101 kg	0.3333, 0.1111, 0.1111 kg
Rotating Ecc. Mass: m_1, m_2	0.3649, 0.2368 kg	0.2222. 0.2222 kg
Springs: k_1, k_2, k_3	599.9. 599.6, 600.6 N/m	600, 600, 600 N/m
Damping: γ	10 kg/s	10 kg/s
Circular Path radius: r_o	0.5 m	0.5 m

Optimization of the three previously discussed mount designs was investigated. Optimization of the wall force for the essentially nonlinear translation system showed favorability in impedance mismatching over the interesting resonant phenomena. However, when the weighting was placed entirely on the first mass displacement, the optimization routine selected the anti-resonant condition.

Optimization of the system with small rotation showed that it favored the unique eigenstructure that results in nodes at the excitation location of the structure. However, unlike previous work, this was accomplished with only a small offset in the first mass attachment location and with different final springs attached to the wall. Previously, identical springs were attached to the wall, which resulted in a cancellation of the rotational forces. The optimized rotational system was compared to optimized non-rotational systems and it was shown that the rotational system had the ability to outperform non-rotational systems in both shock and harmonic excitation isolation.

Optimization of systems with internal oscillators showed that while the system could choose to undergo large angle oscillation, the optimization algorithm indicated the system's wall force was minimized when only small angles were allowed. This condition was accomplished via adjustments to the radius of the rotating eccentric mass' pathway and increasing the level of damping. Furthermore, while the system had the ability to adjust the spring coefficients, these were only changed minimally (less than 1%) and instead the significant changes were seen in the mass values. The optimized solution preferred heavy rotating eccentric masses compared to the housing masses.

CHAPTER 7.

DAMPING AND HALF SINE INPUTS

7.1 Overview

Throughout this thesis, the vibratory systems that were investigated were designed purposely to have light damping so as to accentuate the influence of the system's vibratory characteristics. Low damping was also maintained in order to ensure good high-frequency isolation. In this chapter, we investigate the role of damping in further detail, and study the isolation performance of various dynamic mount designs when the damping is allowed to increase to modest levels. The chapter also discusses how the isolation performance of the mount changes when the applied input force is no longer equal to an impulsive loading. Thus, the chapter examines finite-amplitude half sine input force profiles, and compares the isolation performance against the impulsive input results.

The level of damping in classic built-up structures is in general low, with modal damping ratios of ζ=0.10 or less [70]. For welded or monolithic structures the damping ratios can be an order of magnitude lower. Examples of systems that use damping in isolation elements can be found in the automotive industry and in the earthquake seismic isolation foundations. Damping mechanisms found in automotive main suspensions are usually based on viscous dashpots, however some suspensions use electrorheological (ER) or magnetorheological (MR) fluids, and Coulomb friction also plays a role in some suspension elements such as leaf springs. Earthquake seismic isolation systems have been devised that incorporate damping supplied by elastomeric bearings, lead plugs, mild steel dampers, fluid viscous dampers, and friction in sliding bearings [71], [72].

7.2 Damping and the General Influence on Shock Isolation

Recall from Section 2.3 that the transmitted wall force in a linear system can be viewed as the sum of the modal contributions. This concept was used to derive upper bounds on the system response, for example equation (2.15). Equation (2.15) shows that the contribution of the j^{th} vibratory mode to the response variables is inversely proportional to the damped natural frequency $\omega_{d,j}$.. As the level of damping in the system is increased, the damped natural frequency decreases, but the rate of decay in the response envelopes increases.

To simplify the investigation, a single degree-of-freedom system utilizing linear viscous damping is considered first. The analysis can be found in many vibration texts, for example [39], but it is instructive to review it here. The input is a unit impulse applied to the mass (equivalent to an instantaneous change in the velocity) and the stiffness and mass of the system are held constant as the damping ratio, ζ, is changed. As shown in Figure 7.1, the transmitted wall force initially decreases as the level of damping increases; however, there is an optimum level of damping beyond which the transmitted wall force increases with damping.

It can be shown that, in the case of the single degree of freedom, the maximum contribution from the damper to the wall force occurs at t=0 because of the high initial velocity. All subsequent velocities will be smaller in magnitude than the initial condition due to energy removal via damping. The maximum damping force increases in a linear fashion with ζ and is given by the relation:

$$Force_{damp} = C\dot{x}(0) = v(0) * 2\zeta\sqrt{k * m} \tag{7.1}$$

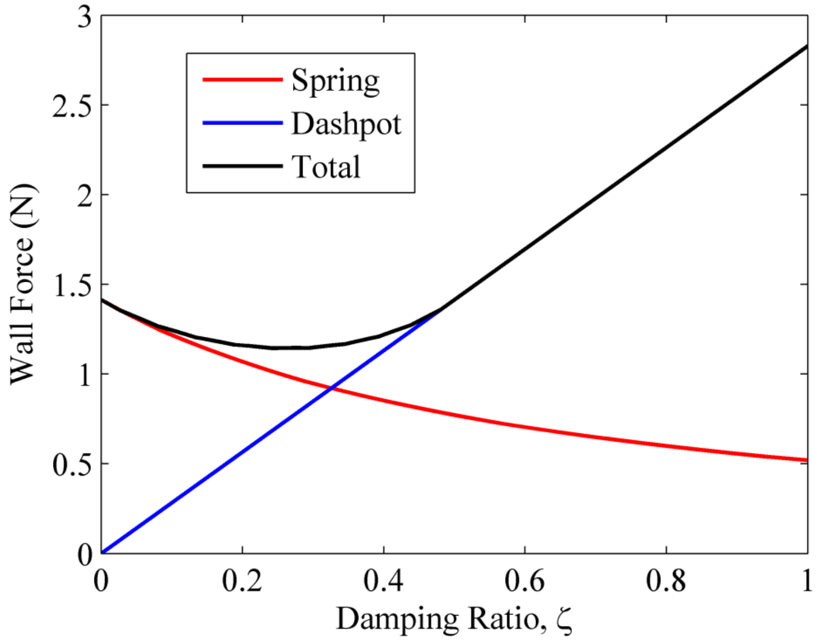

Figure 7.1: Single degree-of-freedom transmitted wall force versus the damping ratio, mass = 1 kg stiffness = 1 N/m.

The displacement begins at zero and reaches its first peak magnitude early in time and then decays with a rate that depends on the level of damping. For low levels of ζ, the total wall force is dominated by the spring, while for moderate levels of ζ the maximum wall force depends on a combination of the spring and damper forces. It can be shown that for $\zeta>0.5$, the maximum wall force is dominated by the damper force alone, which explains why the resultant force curve in Figure 7.1 (black line) grows linearly with ζ. This simplistic analysis helps to explain why high levels of damping are unfavorable for shock isolation; but, it also shows that small levels of damping may be beneficial. It is worth noting that achieving even modest levels of damping in an isolation mount is not always feasible, depending on the physical system involved.

The extension of the trends observed for the single degree-of-freedom system to multiple degree-of-freedom systems yields results that are less clear cut. This is due in part of the wide variety of damping models that can be considered. In the case where viscous dampers are placed in parallel with all springs, a proportional damping model is convenient since it results in uncoupled modal coordinates. Such a damping model can be given mathematically by $[C] = \beta[K]$. This is by far the simplest mathematical model, but it results in higher modes having more damping than lower modes. It is known that structural systems do not exhibit this trend, but the model is still used because of its mathematical simplicity, and the fact that it is easy to interpret the elements of the damping matrix in terms of physical elements.

Figure 7.2 shows the wall force versus the proportional damping factor β for a two degree-of-freedom system having the same overall mass and stiffness as that used for the single degree-of-freedom system above. It is seen that the wall force decreases until approximately $\beta = 0.5$ and then begins increasing. At the point of minimum wall force, the damping ratios of the two vibratory modes are approximately $\zeta_1 = 0.3$ and $\zeta_2 = 0.8$. The trend is similar to what is seen for longer-length chains; however the value of β corresponding to the minim wall force usually yields one or more vibratory modes that are overdamped ($\zeta > 1$).

The qualitative trends observed for proportional damping suggest that isolation in dynamic mounts follows a similar trend to single degree-of-freedom systems. However, the feasibility of creating dynamic mounts with exceptionally high levels of viscous damping is uncertain, and would make a good topic for further research.

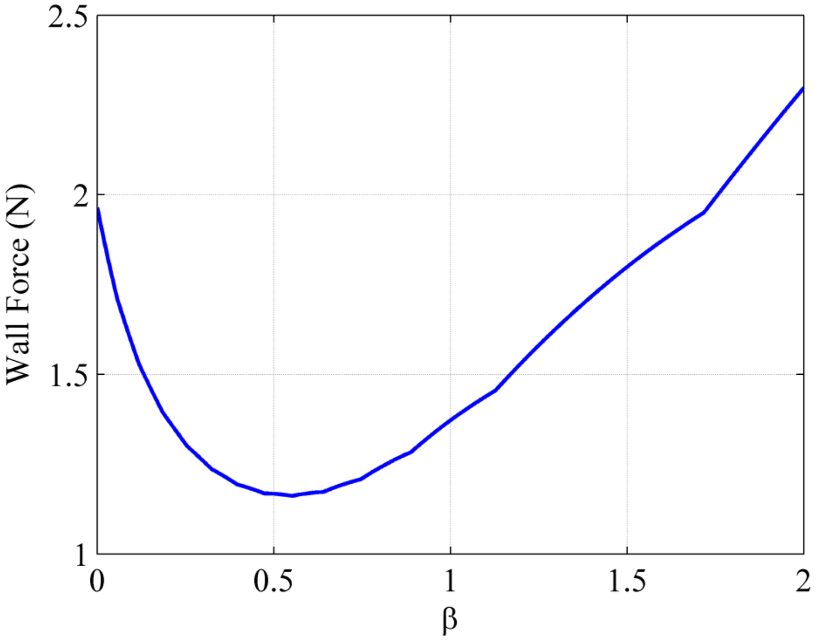

Figure 7.2: Wall force vs β for two degree-of-freedom system with proportional damping, total mass 1 kg and static stiffness of 1 N/m.

7.3 Influence of Damping on the Essentially Nonlinear Chain

The previous section suggests that some shock isolation systems may perform better as the passive damping levels increase. However, the principles on which effective isolation for the dimer chain systems studied in Chapter 2 depend on are very different. Recall that favorable isolation in the dimer chain systems corresponded to a resonance condition between the movement of the light and heavy masses. Damping is likely to disrupt this resonance condition, which could conceivably degrade the isolation performance. This question is addressed in this section.

One advantage of including a small amount of damping in the analysis of the isolation performance of essentially-nonlinear dimer chains was discussed previously in Chapter 2. Namely, modest levels of damping made it easier to determine the times at which maximum wall force and/or maximum first-mass displacement occurred. Figure 7.3 shows the wall force for a cubic chain of N=9 masses, mass ratio of ε =0.46, and a negligible amount of viscous damping. Note that the maximum wall force does not occur in the initial pulse, but much later in time. In contrast, Figure 7.4 shows the shock response of the same system, but for a higher level of intermass viscous damping. In this case, the largest peak in the wall force coincides with the first peak, and is 97% as large as the first peak wall force in the lower damping case. Thus, the presence of modest levels of damping does not change the quantitative level of the response very much, but makes the numerical determination of maxima much more manageable. The influence of damping on the aforementioned system is shown below in Figure 7.5. As the level of damping is increased, initially the force curve begins to smooth out. This is due to the damping reducing the amount of late event constructive interferences in the reflections of the shock propagation (see Figure 7.3 and Figure 7.4). However, as the damping grows, the curve continues to smooth and eventually loses the 1:1 resonant dip.

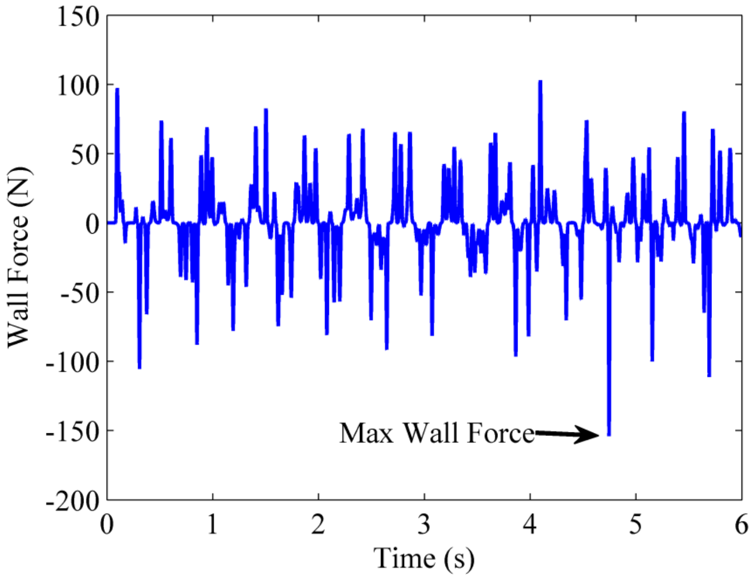

Figure 7.3: Wall force versus time for a mass ratio of 0.46, damping is c = 0 Ns/m.

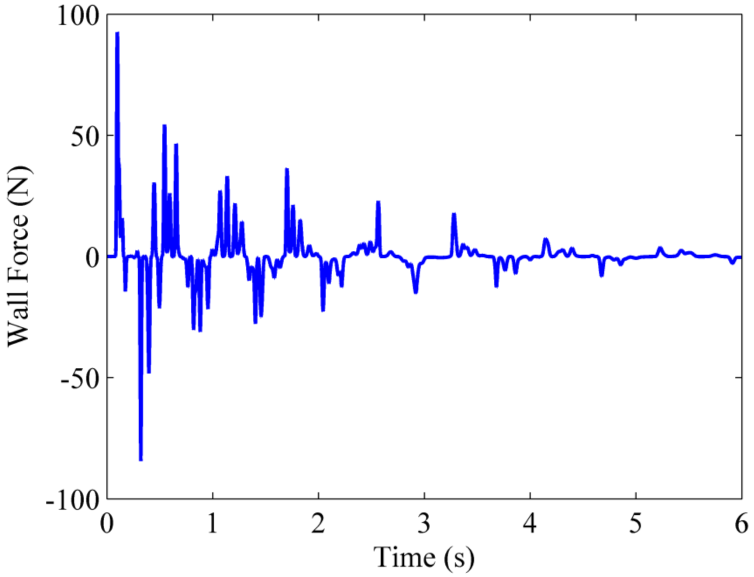

Figure 7.4: Wall force versus time for a mass ratio of 0.46, damping is c = 1 Ns/m

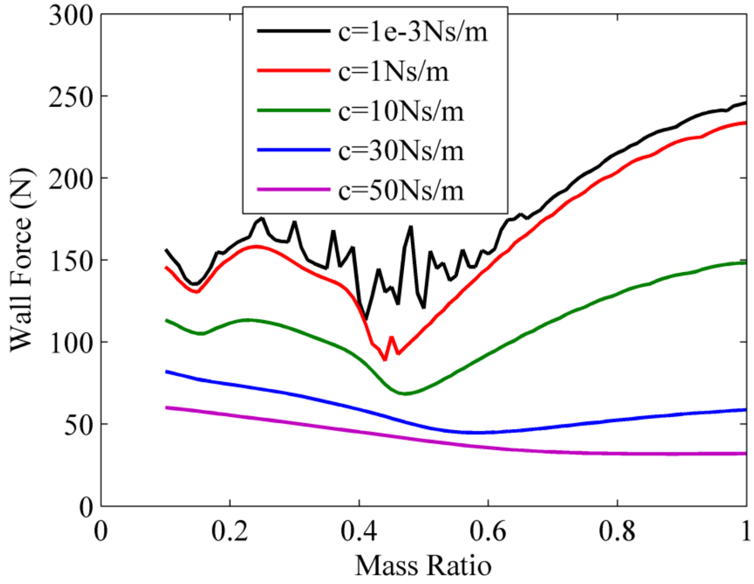

Figure 7.5: Wall force versus mass ratio for a nine mass system with various levels of damping.

7.4 Damping in Small Rotational Chains

Due to the linear nature of the problem, the results are similar to those described in Section 7.2. Shown below in Figure 7.6 and Figure 7.7 is the wall force and first mass displacement for a 2 mass 3DOF (m_1=0.25 kg, M_{tot}=1 kg, k_{eff}=200 N/m, E=0.8) small rotation chain with three different levels of proportional damping. As the maximum level of damping in the proportionally damped system increased from 0% to 10% (damping ratio of mode 3) the wall force and first mass displacement are shown to decrease. It is interesting to note that while the overall level of the wall force decreases, the qualitative feature of a dip or minimum in the force curve persists. Furthermore, the parameter values at which the dip in the wall force occurs seems to be relatively insensitive to the increased damping. Thus the addition of proportional damping in the small-rotation system seems to reduce the response severity, while preserving the interference of modes that yield beneficial isolation.

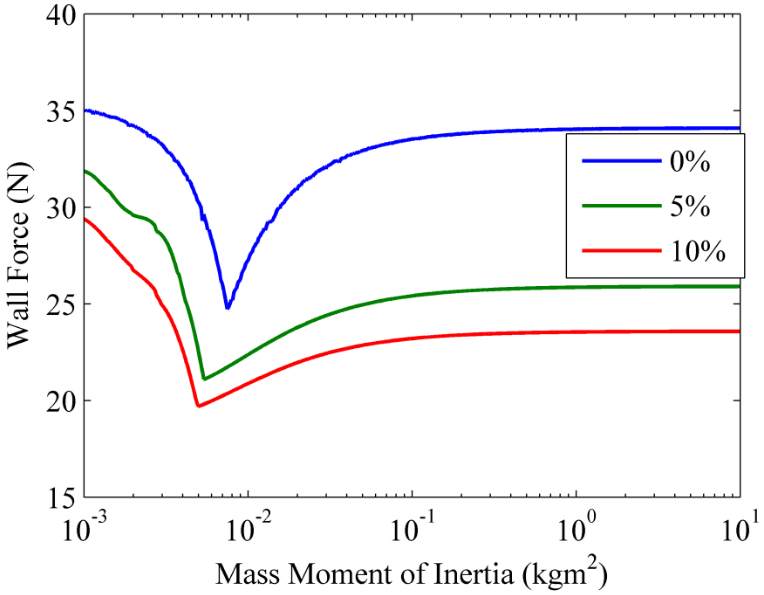

Figure 7.6: Comparison of wall force for three different proportional damping levels in the three degree-of-freedom two mass, small rotation chain.

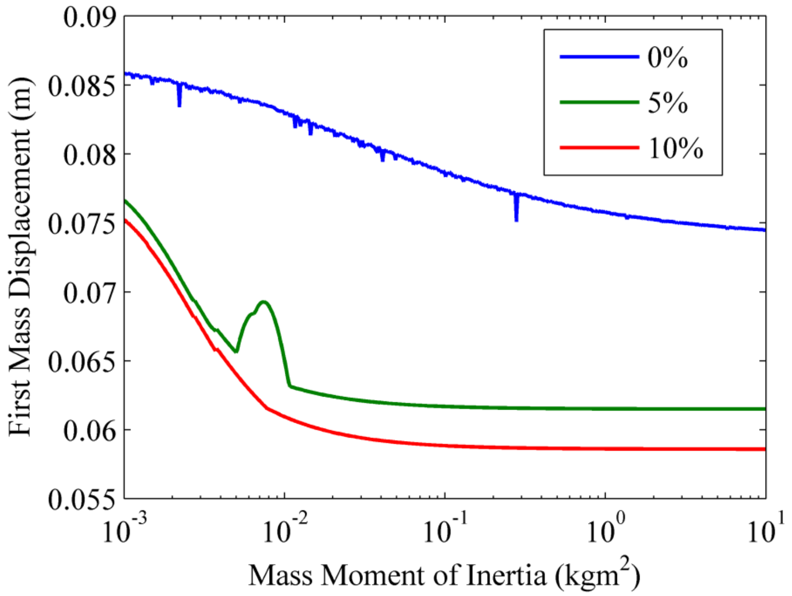

Figure 7.7: Comparison of the first mass displacement for three different levels of proportional damping in the three degree-of-freedom, two mass, small rotation chain.

7.5 Half Sine Inputs

In the work presented until this point in the thesis, only two types of input have been considered: an impulsive loading (instantaneous change in the first mass velocity) and harmonic excitation. However, as was discussed in Section 1.2, there exist numerous input types which are of interest in shock and vibration research and development. To expand the research, investigation into the half sine response of essentially nonlinear cubic systems is performed. The system under consideration consists of an essentially nonlinear cubic chain of N=9 masses with a total mass of 21 kg. The mass ratio is selected to be ε =0.46, the static stiffness is 200N/m, and the linear viscous damping coefficient is 1 Ns/m. Initially the system is investigated with an instantaneous change in the velocity of the first mass: $v_i = 1/m_1$. Using a Hilbert-Huang transform (HHT) [73], the general frequencies in the system can be determined. After, half sines inputs having integrated area 1 Ns are applied to the first mass of the system. The wall force as the mass ratio is varied is then investigated for the half sine inputs. One of the first tasks is to determine a reasonable range of pulse durations for the half sine inputs. It is well known that, as the duration of the half sine approaches zero while the area of the input is maintained equal to 1 Ns, the input will resemble a unit impulse to a greater and greater extent. As the duration of the half sine grows, the response of the system deviates from an impulse response. In the limit as the duration becomes very long relative to the time constants of the system, the response of the system can be approximated by its quasi-static response. Thus, the duration of the half sine inputs must be treated with some care.

An example velocity response of the 4th mass of a 9 mass chain due to the impulsive excitation is shown below in Figure 7.8; $\varepsilon = 0.1$. Due to the lack of damping in the system, constructive interference of reflections in the chain results in the increased response magnitude at later time intervals. The HHT can be applied to this time domain response to determine the general frequency content of the signal, Figure 7.9. As shown in the figure, there are two main frequency groupings. The lower frequency is around 150 rad/s while the higher is around 628 rad/s. The HHT analysis of the nonlinear system yields information similar to an eigenvalue spectrum in a linear system. It gives the approximate frequencies and time constants of the system response, which can be used to determine the characteristic durations of half sine inputs. Figure 7.10 and Figure 7.11 show the velocity response and the HHT, respectively, for the resonant condition, $\varepsilon = 0.46$.

Figure 7.12 shows the wall force versus mass ratio for four different half sine frequency inputs and the impulsive input. For frequencies higher than 130 rad/s (durations lower than 50 ms), the wall force curve is very close to that generated using a unit impulse loading, but the minimum magnitude of wall force is slightly higher. As the frequency of the half sine input increases (duration decreases), the force begins to approach the impulsive loading condition more and more closely. As the frequency of the half sine input decreases (duration increases), the force curve increases in magnitude relative to its value at the equal-mass case, $\varepsilon = 1$. Another important finding is that the characteristic dip in the force curve becomes less and less apparent, indicating that the resonance condition central to the interference between the light and heavy masses becomes less and less effective in disrupting the disturbance propagation. This result may suggest a possible reason for the difficulty encountered during the experimental verification of the shock response discussed in Chapter 3. Recall that it was difficult to replicate a true impulsive loading that produced much motion, so the impulsive loading was replaced with a short "push." It is possible that this push was similar to a half sine input, with time duration insufficiently short to be effective in demonstrating the resonant behavior. This explanation requires further examination, but seems like a plausible hypothesis of what occurred.

7.6 Conclusion

This chapter represents a preliminary study into two of the real-world issues that could impact the performance of dynamic shock mounts. The role of damping was initially investigated for the linear dimer-chain systems with equal masses. The main result was that damping is beneficial to the shock isolation performance of linear mounts as long as the damping did not become too large. This is similar in nature to the well-known result for vibration isolation mounts subjected to harmonic excitation. The

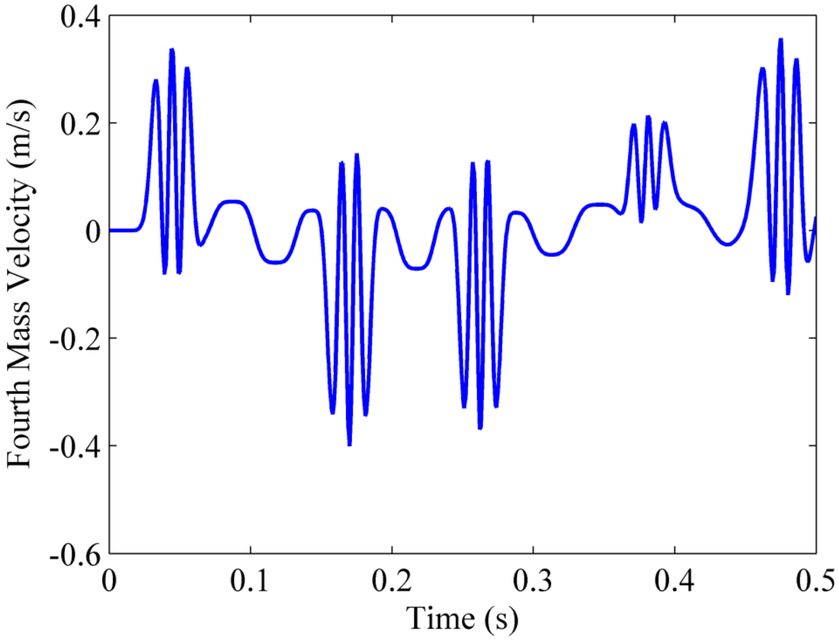

Figure 7.8: Velocity of the fourth mass due to an instantaneous change in velocity of the first mass.

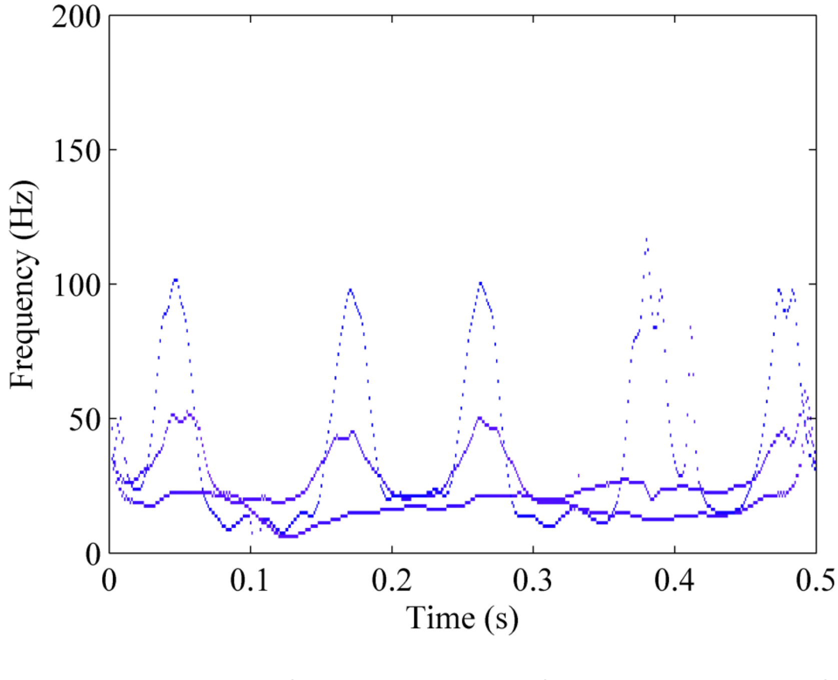

Figure 7.9: Hilbert-Huang transform applied to the fourth mass' velocity for a mass ratio of 0.1 to determine the frequency content.

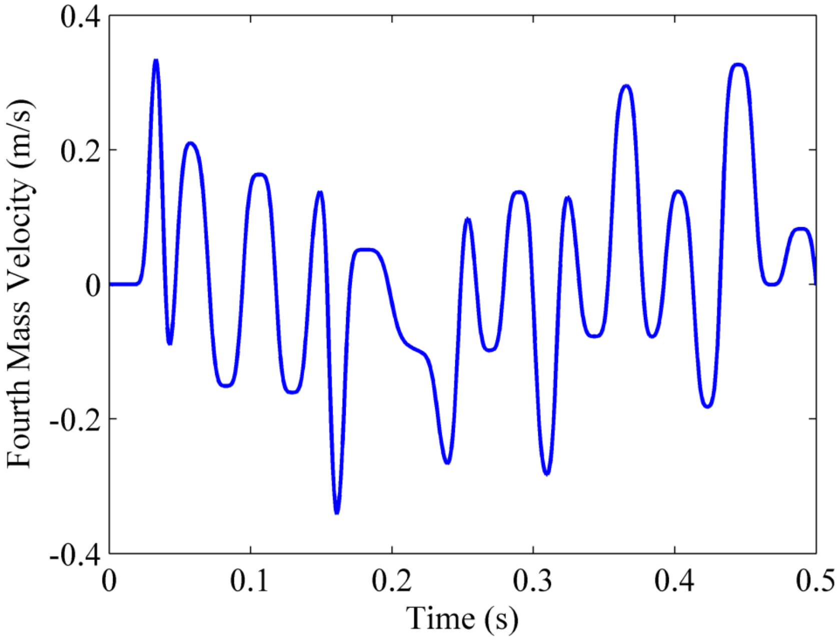

Figure 7.10: Velocity of the fourth mass due to an instantaneous change in the velocity of the first mass; ε = 0.46.

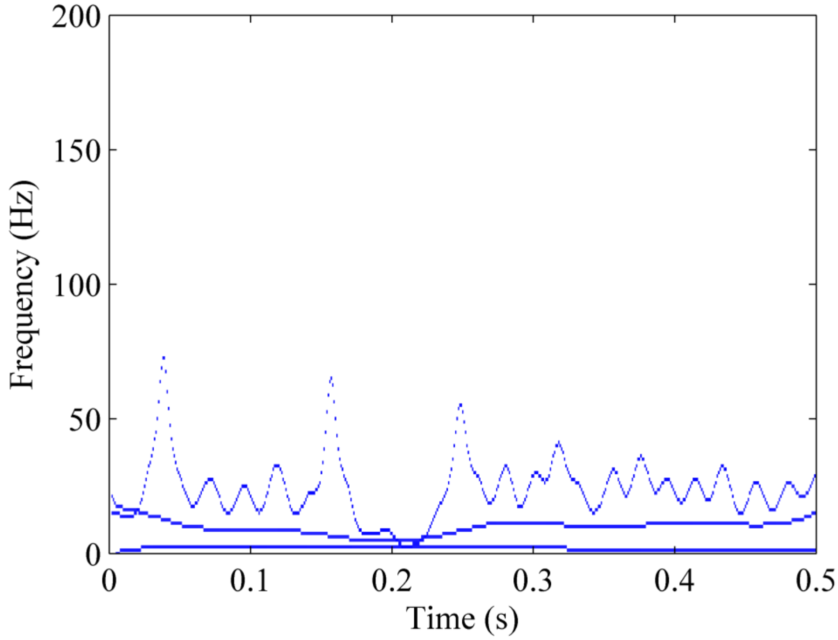

Figure 7.11: Hilbert-Huang transform applied to the fourth mass' velocity for a mass ratio of 0.46 to determine the frequency content.

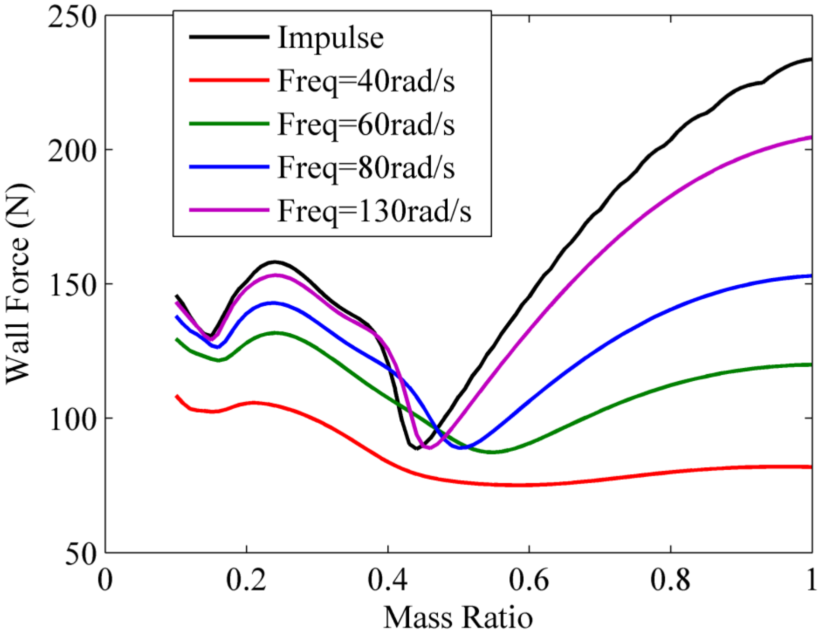

Figure 7.12: Comparison of wall force versus mass ratio for various half sine inputs.

improved performance of the dimer chain isolation may or may not be feasible in practice because it required the modes of the dynamic mount to be near the critical damping levels or even overdamped. Small levels of damping were also investigated for the isolation chains having small-rotational movement. It was reassuring to see that small levels of damping improved the isolation performance, but did not eliminate the modal interactions from occurring. Thus, these types of mounts could be designed using the undamped vibratory properties. The performance of the dynamic mount system should have the same or better performance in the presence of small levels of damping.

The chapter also contained a preliminary exploration of how the performance of dimer-chain systems changes when the impulsive loading is replaced with a more realistic half sine input force. It was interesting to see that the resonance condition that gives rise to the minimization of the wall force in chains with essential nonlinearities is not as effective when the system is excited by a half sine. This is a very significant result, which could help to explain the relatively poor performance observed in the experimental shock investigation discussed in Chapter 3.

Although much more work in this area remains, the two topics discussed in this chapter of the thesis share an important common point. That is, both viscous damping and half sine input tend to discourage the excitation and/or response of higher modes of vibration. Since the performance of dynamic mounts is based on the principles of internal resonance and interaction of modes, it is interesting to see what happens when high frequency modes are either not excited, or die out quickly.

CHAPTER 8.

CONCLUDING REMARKS

8.1 Overview

Shock and vibration isolation is a very challenging research area due to the complicated tradeoffs that are inherent to the problem. However, the problem is also one of the most practical in nature, with far-reaching applications. To improve on isolation performance, researchers have examined a number of different techniques ranging from passive, active and semi-active, and nonlinear mounts. Each type of mount tries in different ways to produce maximum isolation with minimal deformation. Different mount designs may be better for some types of systems and for certain inputs, while others may be better suited to different environmental conditions or applications. No one class of mounts has emerged as the best design for all situations.

This thesis examines the use of dynamic mounts as a way of providing isolation using a paradigm shift in the way that traditional mounts operate. Through the use of internal dynamics, the mounts developed and studied in this thesis attempt to disrupt the disturbance as it propagates along the mount. Through linear and nonlinear means, the mounts attempt to trap and manage the transmission of energy in various ways so that the disturbance that actually reaches the endpoint is lessened. The thesis examines several different ways of managing the disturbances using both linear and nonlinear phenomena. The focus has been on the fundamental ways that each class of dynamic mounts works and to exploit these fundamentals to improve isolation performance. The systems have been studied using theoretical, numerical, and experimental methods.

Purely translational mounts with essentially nonlinear compliance behavior showed that under certain resonant conditions, the transmitted force reaching the end of the mount could be minimized. This result had been discussed by different researchers as a potential mechanism on which practical mounts could be based. But results from other research groups were severely limited by the fact that they relied on Hertzian contact between chains of masses. Without preload, Hertzian chains exhibit essential nonlinear compliance, but they are impractical in that they can only act in compression and not tension. Another omission in previous research was that it considered only force reduction, and did not consider the equally important performance metric of mount deformation. Both shortcomings were addressed in Chapter 2 of this thesis. Physical mount designs were developed that exhibited cubic-spring nonlinear compliance in both tension and compression. The performance of the so-called cubic springs were compared against the performance of Hertzian chains and found to have similar performance. For finite-length chains, however, it was found that linear chains could often outperform the nonlinear chains. An upper bound on the linear system’s response was derived, which was shown to provide a reasonable fit to the behavior obtained through numerical simulation.

Creation of an essentially nonlinear spring was also discussed in Chapter 3. The springs were designed based on the use of membrane forces in thin members. The force-displacement behavior was investigated via a nonlinear finite element analysis and then through a static experimental test of actual physical springs fabricated out of aluminum. It was shown that the finite element and experimental analysis had strong agreement. The displacement force relationship was highly nonlinear; however, not essentially nonlinear.

Sinusoidal excitation of a two-degree-of-freedom system containing a linear component (shaker) and the nonlinear component (spring-mass) showed that a good qualitative understanding of the system could be obtained. Quantitatively, the natural frequency was slightly off, which could be attributed to the dynamic nature of the spring, as it had significant mass which was assumed distributed to other components. Other experimental factors such as the operation of the electromagnetic shaker also contributed to quantitative discrepancies between theory and experiment.

The nonlinear systems presented in Chapter 2 relied on fairly subtle interactions of alternating heavy and light masses along the chain. A fundamentally different approach to isolation mounts was presented in Chapter 4. This mount also contained internal dynamics, but utilized both translational and rotational motion of a chain of masses to control and to trap vibratory energy. The rotational motion was small, allowing small angle approximations to be used in generating linear vibratory models for the mount. By purposely keeping damping low, the study focused on how modes of the system could interact in different ways to mitigate the transmitted force and the overall deformation of the mount. The eigenstructure displayed by the proposed mounts could be used to help cancel out natural frequencies or create nodes in the structure at the excitation location or at the final location, thus reducing the transmitted wall force. The reduction in the wall force was not accompanied by a significant change in the first mass displacement. Consequently, this led to mount concepts that show great promise in the development of practical isolation mounts.

Internal rotations along a dynamic mount were further exploited in Chapter 5. In this case, large angles were considered for internally rotating masses, making the governing equations nonlinear. To better understand the complex behavior in chains of cart/mass subsystems, a single degree-of-freedom system housing was shaken harmonically while a rotating eccentric mass rotated inside. Depending on the initial conditions and parameters such as radius of the circular path, damping, and amplitude of excitation, a wealth of possible response types was obtained. Certain parameters resulted in continuous rotation of the internal masses; others resulted in convergences that would exhibit small oscillations about a particular rotation angle after a number of rotations. In some cases, the rotating eccentric mass would even come to rest. Consequently when these cart/mass subsystems were placed into multi-DOF chains, the resulting response, and hence the resulting isolation performance, was shown to display a wide range of results. It was shown that the mounts had the potential to significantly decrease force transmission in shock without experiencing significant increases in overall mount deformation. However, if the rotations were large, the systems response could become erratic. The inclusion of gravity helped alleviate some of this; however, in harmonic excitation the mounts did not perform as well as linear mounts and for large oscillation could result in unstable or chaotic response at resonance.

Optimizations of all three mount categories were investigated in Chapter 6 in order to obtain enhanced shock isolation performance. For purely translational systems, it was shown that while the resonant condition internal to the essentially nonlinear chain gave a reduction in wall force, the performance could be significantly improved by optimization of the mass structure. For finite-length chains, the system performance is dictated by impedance mismatching, which is different than the concept of internal resonance used to explain force transmission reduction in Hertzian dimer chains.

Optimization of the first mass displacement resulted in a mass ratio of 1, which is an anti-resonant condition.

Optimization of the small rotational chain systems of Chapter 5 showed that improvements in isolation performance could be realized by expanding the space of design parameters. However, as the number of design variables increased, the optimization process was computationally challenging. In the smaller mounts, it was shown that significant reduction in wall force could be accomplished while avoiding a significant change in the first mass displacement. This was accomplished via the optimization algorithm producing systems with an advantageous eigenstructure and commensurate natural frequencies. The improved shock isolation was also accompanied by a similar beneficial harmonic response. It was shown that without rotation and a cost function that focused on wall force, the optimization routine generated a mount design that attempted to combine the two-degree-of-freedom system into a one-degree-of-freedom. This was accomplished by placing a vastly stiffer spring between the masses, thus working on joining them into one mass, and a soft spring to the wall to satisfy the static stiffness constraint.

Optimization of the system with potentially large rotation showed the desire for the system to utilize high levels of damping to keep the internal masses moving with small amplitudes of oscillation.

Finally the role of damping was further investigated in Chapter 7. It was shown that, up to a point, increasing the level of damping improved the isolation performance of the mount with respect to shock loading. However, the feasibility of creating physically practical mounts with high or even moderate damping levels is questionable. Clearly, if acceptable isolation performance can be realized without the use of internal damping, that would be preferable due to its simplicity and reliability. Chapter 7 also contained a preliminary investigation of non-impulsive shock loading. Half sine force inputs were applied to the essentially nonlinear translational chains with surprising results. After determining the frequency content of the system response using a HHT analysis, a range of half sine inputs of different frequencies (durations) was applied to the system. The wall force resulting from relative slow half sine inputs did not display the characteristic dip for mass ratios near 0.5. Instead, as the duration of the half sine input increased, the performance for a mass ratio of 1.0 tended to be closer and closer to the best design point.

8.2 Research Contributions

The research in this thesis has produced a number of significant contributions. In particular, the research:

- Showed the importance of maintaining an overall mount mass and static stiffness when comparing isolators.
- Provided useful comparisons between linear and essentially nonlinear purely translational mounts.
- Started the design process for the creation of essentially nonlinear cubic springs and successfully produced an aluminum realization of that design.
- Performed and documented static and dynamic experiments on a highly nonlinear cubic spring.
- Expanded the design space of dynamic mounts by including rotational motion.

- Further showed the importance of including rotation in mount design to minimize transmitted wall force without a significant change in first mass displacement, thereby discovering a superior mount design.
- Explained that the reduction in transmitted wall force for systems with small rotation was induced by nodal points in the eigenstructure, which was achieved by tuning system parameters such as the mass moments of inertia.
- Showed that large oscillatory motion can be detrimental in systems with internal oscillators due to the complicated nature of the response and the associated reactions between the housings.
- Applied optimization to three mount designs and provided further insight into their benefits: e.g., essentially nonlinear systems can further benefit from impedance mismatching rather than a resonant condition.
- Studied the role of damping in shock isolation. It was found that linear viscous damping could be beneficial or detrimental to shock isolation performance.
- Explored the shock performance of nonlinear translational chains for the case of half sine force loading. It was seen that if the duration of the half sine input was sufficiently small relative to the time constants of the nonlinear response, the half sine inputs produced results that were qualitatively similar to perfect impulses. However, as the duration of the half sine excitation became slightly larger, the pronounced dip in the force transmission curve disappeared.

8.3 Recommendations for Future Work

Although the research presented within this document offers significant advancements in mount design, there are a number of exciting areas left for further exploration. The guidelines and tools presented here should provide future researchers with an excellent starting point as they continue to evolve the ideas in shock and vibration isolation.

A first generation nonlinear spring presented in Chapter 3 was investigated via static experimentation and finite element analysis. Future iterations of the spring design should help increase its ability to be used in practical mount design. It would also be interesting to see how varying degrees of the linear part of the spring function modifies the results for force transmission and first mass displacement. The continued evolution will then facilitate future static and dynamic testing. Furthermore, all other mounts discussed within this document are capable of being produced and investigated experimentally. Experimental investigations of these different mount concepts are invaluable in validating the behavior predicted through numerical simulations. Experimentation is also a necessary step in developing the next generation of practical, dynamic mounts.

This research has primarily focused on either sinusoidal force excitation or on impulsive forces applied to an attachment point. However, much more investigation is necessary to investigate other types of input. Chapter 7 contained a preliminary study of half sine inputs, but other types of transient disturbances are also of interest.

Also of interest is the extension of the analyses contained in this thesis to transmissibility problems in which the system is subjected to seismic or base excitation.

In this important class of problems, the mount is placed between the ground and some moveable object to determine the degree to which the prescribed base movement is imparted to the moveable object.

The optimization study in Chapter 6 showed promising performance improvements for the three different types of dynamic isolation systems examined in this thesis. However, much remains to be done. In particular, the studies of Chapter 6 fall into the realm of parametric design. Extending the optimization process to systems where the number of degrees of freedom is also varied would be useful, although quite challenging. For example the issue regarding the role of chain length in isolation performance is somewhat of an open question. The author has speculated that essentially nonlinear chains benefit from increased chain length, especially with regard to force transmission. However, linear systems tended to exhibit their best performance for relatively small length chains. Optimization of the systems would ultimately reveal the ideal length given a specific input.

The large rotational systems studied in Chapter 5 were passive in nature. But one could consider modifying the concept to include the case where the internal rotating masses are driven, for example with small motors. By driving these masses, reaction forces could be further tailored to control the transmission of shock to the wall location. A related idea would be to use the motors as a way of harvesting energy from the internal movement as a way of powering sensors and/or actuators as well as to supply additional energy removal.

Finally, Chapter 2 investigated systems with nonlinear compliance, which was a central feature of their behavior and performance. The use of nonlinear compliance in the small-rotation chains and in the cart/mass systems is an unexplored area for further research. It is possible that, through use of nonlinear connections, even better mechanisms may be revealed for trapping and managing vibratory energy within a dynamic mount.

APPENDIX

ALTERNATIVE FORM FOR THE EQUATIONS OF MOTION FOR SMALL ROTATION SYSTEMS

This Appendix contains an alternate formulation for the equations of motion of the dynamic mounts having both translation and small-rotations. The advantage of the formulation contained herein is that it contains all of the design variables in an easily-accessible form. Namely, all design variables occur as scalar parameters or as entries in diagonal matrices.

The equations of motion are derived by considering the tensile deformation of each spring. Figure A.0.1 shows the tensile forces in the “bottom” and “top” springs ($B_0,\ldots,B_N$) and ($T_1,\ldots,T_N$), respectively, acting on each mass due to the tensile deformations in the bottom ($b_0, \ldots, b_N$) and top ($t_1, \ldots, t_N$) springs.

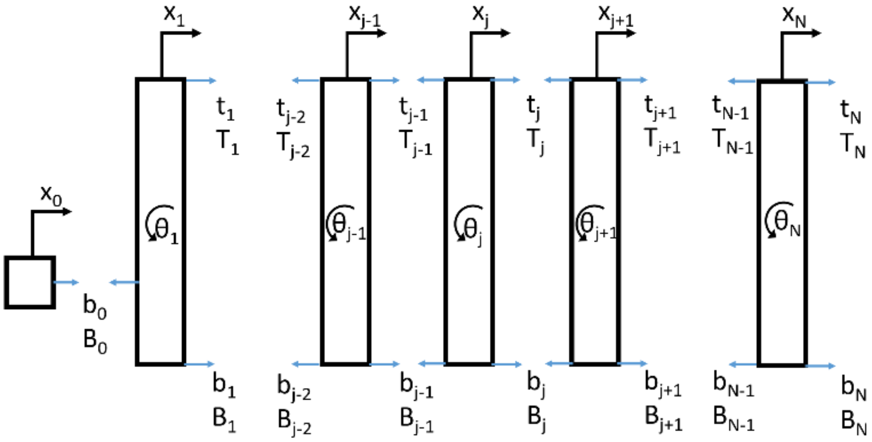

Figure A.0.1: Tensile deformations and forces along the chain.

Using the small angle assumption, deformations are described in terms of kinematic variables as follows:

$$b_0 = x_1 + \theta_1 d - x_0$$

$$b_j = -x_j + x_{j+1} - L\theta_j + L\theta_{j+1}$$

$$t_j = -x_j + x_{j+1} + L\theta_j - L\theta_{j+1}$$

$$b_N = -x_N - L\theta_N$$

$$t_N = -x_N + L\theta_N \tag{A.0.1}$$

In matrix form:

$$[W] = \begin{bmatrix} b_0 \\ t_1 \\ \vdots \\ t_N \\ b_1 \\ \vdots \\ b_N \end{bmatrix} = [G] \begin{bmatrix} x_0 \\ x_1 \\ \vdots \\ x_N \\ \theta_1 \\ \vdots \\ \theta_N \end{bmatrix} = [G]\{y\} \tag{A.0.2}$$

where [*G*] is a matrix of constants, which relates degrees of freedom to spring tensile deformations. For example, deformation in the j^th^ top spring is calculated using the j^th^ row of [*G*].

$$t_j = \left[0 \; \overbrace{0 \; \cdots \; 0 \; \underbrace{-1}_{j+1} \; \underbrace{1}_{j+2} \; 0 \; \cdots \; 0}^{N} \overbrace{0 \; \cdots \; 0 \; \underbrace{L}_{N+1+j} \; \underbrace{-L}_{N+2+j} \; 0 \; \cdots \; 0}^{N} \right] \begin{bmatrix} x_0 \\ x_1 \\ \vdots \\ x_N \\ \theta_1 \\ \vdots \\ \theta_N \end{bmatrix} \tag{A.0.3}$$

Balancing forces and moments at each link yields linear, second order differential equations that describe the motion of the masses. The first mass is only translational, so the equation of motion can be written as:

$$m_0 \ddot{x}_0 = B_0 + F(t) \tag{A.0.4}$$

The next *N* masses have translational and rotational degrees of freedom:

$$m_1\ddot{x}_1 = T_1 + B_1 - B_0$$

$$J_1\ddot{\theta}_1 = -B_0 d - T_1 L + B_1 L$$

$$m_j\ddot{x}_j = -T_{j-1} - B_{j-1} + T_j + B_j$$

$$J_j\ddot{\theta}_j = T_{j-1}L - B_{j-1}L - T_j L + B_j L \tag{A.0.5}$$

Combining results from all masses yields:

$$[M]\{\ddot{y}\} = [H]\begin{bmatrix} B_0 \\ T_1 \\ \vdots \\ T_N \\ B_1 \\ \vdots \\ B_N \end{bmatrix} + \{e_1\}F(t) = [H][K1][G]\{y\} + \{\mathrm{e}_1\}F(t) \tag{A.0.6}$$

where:

$$[M] = diag[m_0\, m_1 \ldots m_N\, J_1 \ldots J_N]$$

$$[K1] = diag[k_0\, s_1 \ldots s_N\, k_1 \ldots k_N] \tag{A.0.7}$$

And $\{e_1\}$ is the first Cartesian basis vector. $[H]$ is a $2N+1$ by $2N+1$matrix of constants relating the total forces and moments on each mass to the forces at the spring attachment points. For example, total force on the jth rotating mass is calculated using the j+1th row of [H]:

$$m_j\ddot{x}_j = \begin{bmatrix} 0 & \overbrace{0 \;\cdots\; \underbrace{-1}_{j-1} \;\; \underbrace{1}_{j} \;\; 0 \;\cdots\; 0}^{N} & \overbrace{0 \;\cdots\; \underbrace{-1}_{N+j-1} \;\; \underbrace{1}_{N+j} \;\; 0 \;\cdots\; 0}^{N} \end{bmatrix} \begin{bmatrix} B_0 \\ T_1 \\ \vdots \\ T_N \\ B_1 \\ \vdots \\ B_N \end{bmatrix} \tag{A.0.8}$$

The total moment on the jth rotating mass is calculated using the N+j+1th row of $[H]$:

$$J_j\ddot{\theta}_J = \begin{bmatrix} 0 & \overbrace{0 \; \cdots \; \underbrace{L}_{j-1} \; \underbrace{-L}_{j} \; 0 \; \cdots \; 0}^{N} & \overbrace{0 \; \cdots \; \underbrace{-L}_{N+j-1} \; \underbrace{L}_{N+j} \; 0 \; \cdots \; 0}^{N} \end{bmatrix} \begin{bmatrix} B_0 \\ T_1 \\ \vdots \\ T_N \\ B_1 \\ \vdots \\ B_N \end{bmatrix} \qquad \text{(A.0.9)}$$

Relations such as equations (A.0.8) and (A.0.9) populate the rows of $[H]$.

Constant modal damping is also included in the isolator model. Modal damping is utilized for its ability to prescribe the level of damping in each mode, which is set equal and low to prevent performance reduction in the frequency region of isolation. With the damping included, the equations of motion become:

$$[M]\{\ddot{y}\} + [C]\{\dot{y}\} + [K]\{y\} = \{e_1\}F(t) \qquad \text{(A.0.10)}$$

where:

$$[C] = [M][\Phi][2\zeta\omega_n][\Phi]^T[M] \qquad \text{(A.0.11)}$$

and:

$$[K] = -[H][K1][G] \qquad \text{(A.0.12)}$$

$[\Phi]$ are the undamped mass-normalized modes and $[2\zeta\omega_n]$ is a diagonal matrix involving the natural frequencies and the critical damping ratio, ζ.

REFERENCES

[1] Winthrop, M. F. and Cobb, R. G., 2003, "Survey of State-of-the-Art Vibration Isolation Research and Technology from Space Applications," Proceedings of SPIE, Vol. 5052, pp. 13-26.

[2] Harris, C. M., Ed., 1988, Shock and Vibration Handbook, 3rd Edition, McGraw-Hill, New York, NY.

[3] Kelley, S. G., 2000, Fundamentals of Mechanical Vibrations, 2nd Edition, McGraw-Hill

[4] Karnopp, D., 1995, "Active and Semi-Active Vibration Isolation," ASME *Journal of Vibration and Acoustics,* Vol. 117B, pp. 117-128.

[5] Balandin, D. V., Bolotnik, N. N., and Pilkey, W. D., 1998, "Review: Optimal Shock and Vibration Isolation," *Shock and Vibration,* Vol. 5, No. 2, pp. 73-87.

[6] Ibrahim, R. A., 2008, "Recent Advances in Nonlinear Passive Vibration Isolators," *Journal of Sound and Vibration*, Vol. 314, No. 3, pp. 371-452.

[7] Shahid, E., and Ferri, A. A., 2012, "Passive, Transitioning Mounts for Simultaneous Shock and Vibration Isolation," Proceedings, ASME 2012 IDETC, Chicago, IL, Aug. 12-15, 2012.

[8] Kim, K. R., You, Y. H., and Ahn, H. J., 2013, "Optimal Design of a QZS Isolator Using Flexures for a Wide Range of Payload," *International Journal of Precision Engineering and Manufacturing*, Vol. 14, No. 6, pp. 911-917

[9] Ahn, H. J., 2010, "A Unified model for quasi-zero-stiffness passive vibration isolators with symmetric nonlinearity," Proceedings, ASME 2010, IDETC, Montreal, Quebec, Canada, Aug. 15-18, 2010.

[10] Tang, Bin and Brenna, M. J., 2014, "On the shock performance of a nonlinear vibration isolator with high-static-low-dynamic-stiffness," *International Jounral of Mechanical Sciences*, Vol. 81, pp. 207-214.

[11] Shin, Young, S., 2004, "Ship Shock Modeling and Simulation for Far-Field Underwater Explosion," *Computers and Structures*, Vol. 82, pp. 2211-2219.

[12] Meirovitch, Leonard, 1997, Principles and Techniques of Vibrations, Prentice Hall, Upper Saddle River, NJ.

[13] Du, Y., Burdisso, R. A., Nikolaidis, E., and Tiwari, D., 2003, "Effects of Isolators Internal Resonances on Force Transmissibility and Radiated Noise," *Journal of Sound and Vibration*, Vol. 268, pp. 751-778

[14] Dylejko, P. G. and MacGillivray, I. R., 2014, "On the Concept of a Transmission Absorber to Suppress Internal Resonance," *Journal of Sound and Vibration*, Vol. 333, pp. 2719-2734.

[15] Yilmaz, C. and Kikuchi, N., 2006, "Analysis and Design of Passive Low-Pass Filter-Type Vibration Isolators Considering Stiffness and Mass Limitations," *Journal of Sound and Vibration*, Vol. 293, pp. 171-195.

[16] Baravelli, E. and Ruzzene, M., 2013, "Internally Resonating Lattices for Bandgap Generation and Low-Frequency Vibration Control," *Journal of Sound and Vibration*, Vol. 332, pp. 6562-6579.

[17] Igusa, T. and Xu, K., 1994, "Vibration Control Using Multiple Tuned Mass Dampers," *Journal of Sound and Vibration*, Vol. 175, No. 4, pp. 491-503.

[18] Zuo, L. and Nayfeh, S.A., 2005, "Optimization of the Individual Stiffness and Damping Parameters in Multiple-Tuned-Mass-Damper Systems," *Journal of Vibration and Acoustics*, Vol. 127, No. 1, pp. 77-83.

[19] Vakakis, 2003, "Shock Isolation Through the Use of Nonlinear Energy Sinks," *Journal of Vibration and Control*, Vol. 9, No. 1, pp. 79-93.

[20] Yilmaz, C. and Kikuchi, N., 2006, "Analysis and Design of Passive Band-Stop Filter-Type Vibration Isolators for Low-Frequency Applications," *Journal of Sound and Vibration*, Vol. 291, pp. 1004-1028.

[21] Xiuchang, H., Aihua, J., Zhiyi, Z., and Hongxing, H., 2011, "Design and Optimization of Periodic Structure Mechanical Filter in Suppression of Foundation Resonances," *Journal of Sound and Vibration*, Vol. 330, pp. 4689-4712.

[22] Jensen, J.S., 2003, “Phononic Band Gaps and Vibrations in One- and Two-Dimensional Mass-Spring Structures,” *Journal of Sound and Vibration*, 266, pp. 1053-1078.

[23] Hussein, M.I. Hulbert, G.M., and Scott, R.A., 2006, "Dispersive Elastodynamics of 1D Banded Materials and Structures: Analysis," *Journal of Sound and Vibration*, Vol. 289, pp. 779–806.

[24] Spadoni, A. and Daraio, C., 2009, "Vibration Isolation via Linear and Nonlinear Periodic Devices," Proceedings of the 2009 ASME IDETC, San Diego, CA, August 30- September 2, 2009.

[25] Daraio, C., Nesterenko, V.F., Herbold, E.B., and Jin, S., 2006, “Energy Trapping and Shock Disintegration in a Composite Granular Medium,” *Physical Review Letters*, Vol. 96, pp. 058002-1 – 0058002-4.

[26] Jayaprakash, K.R., Starosvetsky, Y., Vakakis, A.F., and Gendelman, O.V., 2013, “Nonlinear Resonances Leading to Strong Pulse Attenutation in Granular Dimer Chains,” *Journal of Nonlinear Science,* Vol. 23, No. 3, pp. 363-392.

[27] Potekin, R., Jayaprakash, K.R., McFarland, D.M., Remick, R., Bergman, L.A., and Vakakis, A.F., 2013, “Experimental Study of Strongly Nonlinear Resonances and Anti-Resonances in Granular Dimer Chains,” *Experimental Mechanics*, Vol. 53, No. 5, p 861-870.

[28] Smith, E. and Ferri, A. A., 2013, “Shock Isolation In Finite-Length Dimer Chains With Linear, Cubic and Hertzian Spring Interactions,” Proceedings, ASME 2013 IDETC Conference, Portland, OR, Aug. 4-7.

[29] Smith, E. and Ferri, A. A., 2015, “Shock Isolation In Finite-Length Dimer Chains With Linear, Cubic and Hertzian Spring Interactions,” *Journal of Vibration and Acoustics*, Vol. 138 (1), pp. 011012-011012-8.

[30] Murnal, P. and Sinha, R., 2004, “Aseismic Design of Structure-Equipment Systems Using Variable Frequency Pendulum Isolator,” *Nuclear Engineering and Design,* Vol. 231(2), pp. 129-139.

[31] Tsai, C. S., Chen, W. S., Chiang, T. C., and Chen, B. J., 2006, “Component and Shaking Table Rests for Full-Scale Multiple Friction Pendulum Systems,” *Earthquake Engineering and Structural Dynamics*, Vol. 35(13), pp. 1653-1675.

[32] Patil, S. J. and Reddy, G. R., 2012, "State of Art Review – Base Isolation Systems for Structures," *International Journal of Emerging Technology and Advanced Engineering,* Vol. 2(7), pp. 438-453.

[33] Lee, C. T. and Shaw, S. W., 1997, "The Non-Linear Dynamic Response of Paired Centrifugal Pendulum Vibration Absorbers," *Journal of Sound and Vibration,* Vol. 203(5), pp. 731-743.

[34] Gendelman, O., Manevitch, L., Vakakis, A., and M'Closkey, R., 2001, "Energy Pumping in Nonlinear Mechanical Oscillators: Part I – Dynamics of the Underlying Hamiltonian System," *Journal of Applied Mechanics,* Vol. 68, pp. 34-41.

[35] Vakakis, A., Gendelman, O., 2001, "Energy Pumping in Nonlinear Mechanical Oscillators: Part II – Resonance Capture," *Journal of Applied Mechanics,* Vol. 68, pp. 42-48.

[36] Vakakis, A., Manevitch, L., Musienko, A., Kerschen, G., and Bergman, L., 2005, "Transient Dynamics of a Dispersive Elastic Wave Guide Weakly Coupled to an Essentiall Nonlinear End Attachment," *Wave Motion,* Vol. 41, pp. 109-132.

[37] Bellet, R., Cochelin, B., Herzog, P., and Mattei, P. O., 2010, "Experimental Study of Targeted Energy Transfer from an Acoustics System to a Nonlinear Membrane Absorber," *Journal of Soun and Vibration,* Vol. 329(14), pp. 2768-2791.

[38] Huang, W. Y., Chao, C. P., Kang, J. R., and Sung, C. K., 2002, "The Application of Ball-Type Balancers for Radial Vibration Reduction of High-Speed Optic Disk Drives," *Journal of Sound and Vibration,* Vol. 250(3), pp. 415-430.

[39] Ginsberg, Jerry H., 2001, Mechanical and Structural Vibrations: Theory and Applications, John Wiley and Sons, New York, NY.

[40] Nayfeh, A. H., Nayfeh, J. F., and Mook, D. T., 1992, "On Methods for Continuous Systems with Quadratic and Cubic Nonlinearities," *Nonlinear Dynamics,* Vol. 3(2), pp. 145-162.

[41] Manktelow, K. L., Leamy, M. J., and Ruzzene, M., 2011, "Multiple Scales Analysis of Wave-Wave Interactions in a Cubically Nonlinear Monoatomic Chain," *Nonlinear Dynamics,* Vol. 63, pp. 193-203.

[42] El-Bassiouny, A. F., 1999, “Response of a Three-Degree-of-Freedom System with Cubic Non-linearities to Harmonic Excitation,” *Applied Mathematics and Computation*, Vol. 104, pp. 65-84.

[43] Nayfeh, A. H. and Mook, D. T.,1995, Nonlinear Oscillations, John Wiley and Sons, Hoboken, NJ.

[44] Lee, Y. S., Vakakis, A. F., Berman, L. A., McFarland, D. M., Kerschen, G., Nucera, F., Tsakirtzis, S., and Panagopoulos, P. N., 2008, “Passive Non-linear Targeted Energy Transfer and its Applications to Vibration Absorption: A Review,” *Proceedings of IMechE*, Vol. 222 Part K, pp. 77-130.

[45] Jiang, X., McFarland, D. M., Bergman, L. A., and Vakakis, A. F., 2003, “Steady Static Passive Nonlinear Energy Pumping in Coupled Oscillators: Theoretical and Experimental Results,” *Nonlinear Dynamics*, Vol. 33, pp. 87-102.

[46] Jutte, C. V., 2008, Generalized Synthesis Methodology of Nonlinear Springs for Prescribed Load-Displacement Functions, Dissertation, The University of Michigan, Ann Arbor.

[47] Singh, G. S., Sharma, A. K., and Rao, G. V., 1990, “Large-Amplitude Free Vibrations of Beams – A Discussion on Various Formulations and Assumptions,” *Journal of Sound and Vibration*, Vol. 142(1), pp. 77-85.

[48] Lang, G. F. and Snyder, D., 2001, “Understanding the Physics of Electrodynamic Shaker Performance,” *Sound and Vibration*, Vol. 35(10), pp. 24-33.

[49] Ferri, A. A. and Leamy, M. J., 2009, “Error Estimates for Harmonic-Balance Solutions of Nonlinear Dynamical Systems,” *Proceedings of AIAA Structures, Structural Dynamics, and Materials Conference,* Palm Springs, California, May 4th-7th, 2009.

[50] Smith, E. and Ferri, A. A., 2015, “Shock Isolation Through Translational-to-Rotational Energy Transference,” Proceedings, ASME 2015 IDETC Conference, Boton, MA, Aug. 2-5.

[51] Mottershead, J. E. and Ram, Y. M., 2006, “Inverse Eigenvalue Problems in Vibration Absorption: Passive Modification and Active Control,” *Mechanicsl Systesms and Signal Processing*, Vol. 20, pp. 5-44.

[52] Ouyang, H., Richiedei, D., Trevasani, A., and Zanardo, G., 2012, "Eingenstructure assignment in Undamped Vibrating Systems: A Convex-Constrained Modification Method Based on Receptances," *Mechanical Systems and Signal Processing*, Vol. 27 pp. 397-409

[53] Ouyang, H. and Zhang, J., 2015, "Passive Modifications for Partial Assignment of Natural Frequencies of Mass-Spring Systems," *Mechanical Systems and Signal Processing*, Vol. 50-51, pp. 214-226.

[54] Classen, R. W. and Thorne, C. J., 1962, "Vibrations of a Rectangular Cantilever Plate," *Journal of Aerospace Science*, Vol. 29, pp. 1300-1305.

[55] Webster, J. J., 1968, "Free Vibrations of Rectangular Curved Panels," *International Journal of Mechanical Science*, Vol. 10, pp. 571-582.

[56] Bonisoli, E., Deprete, C., and Esposito, M., "Structural Dynamics with Coincident Eigenvalues: Modeling and Testing," Proceedings of the Society for Experimental Mechanics Series 2011, Modal Analysis Topics, Vol. 3, pp. 325-337.

[57] Leissa, A. W., 1974, "On a Curve Veering Aberration," *Journal of Applied Mathematics and Physics*, Vol. 25, pp. 99-111.

[58] Liu, X. L., 2002, "Behaviour of Derivatives of Eigenvalues and Eigenvectors in Curve Veering and Mode Localisation and Their Relation to Close Eigenvalues," *Journal of Sound and Vibration*, Vol. 256(3) pp. 551-564.

[59] Perkins, N. C. and Mote, C. D. Jr, 1986, "Comments on Curve Veering in Eigenvalue Problems," *Journal of Sound and Vibration*, Vol. 106(3), pp. 451-463.

[60] du Bois, J. L., Adhikari, S., and Lieven, N. A. J., 2011, "On the Quantification of Eigenvalue Curve Veering: A Veering Index," *Journal of Applied Mechanics*, Vol. 78, pp. 041007-1 – 041007-8.

[61] Smith, E. and Ferri, A. A., 2015, "Shock and Vibration Isolation Using Internally Rotating Masses," Proceedings, ASME 2015 IDETC Conference, Boston, MA, Aug. 2-5.

[62] Smith, E. and Ferri, A. A., 2015, "Vibration Isolation From Harmonic Disturbances Through Use of Internally Rotating Masses," Proceedings, ASME, 2015 IMECE Conference, Houston, TX, Nov. 13-19.

[63] Sigalov, G., Gendelman, O. V., Al-Shudeifat, M. A., Manevitch, L. I., Vakakis, A. F., and Bergman, L. A., 2012, "Resonance Captures and Targeted Energy Transfers in an Inertially-Coupled Rotational Nonlinear Energy Sink," *Nonlinear Dynamics,* Vol. 69, pp. 1693-1704.

[64] Menvich, A. and Sayko, M., 2013, "Synchronic Regimes in Oscillator-Rotator System (Rotation in Vertical Plane)," *Proceedings of the 4th International Conference on Nonlinear Dynamics*, Sevastpol, Ukraine, June 19-22, 2013.

[65] Guckenheimer, John and Holmes, P., 2002, Nonlinear Oscillations, Dynamical Systems, and Bifurcations of Vector Fields (Applied Mathematical Sciences), Springer, Verlag, NY.

[66] Kirpatrick S., Gelatt, C., and Vecchi, M., 1983, "Optimization by Simulated Annealing," *Science*, Vol. 220 (4598), pp. 671-680.

[67] Laarhoven, P. J. M. and Aarts, E. H. L., 1987, Simulated Annealing: Theory and Applications, Springer.

[68] Michaux, M. A., Ferri, A. A., and Cunefare, K. A., 2008, "Effect of Waveform on the Effectiveness of Tangential Dither Forces to Cancel Friction-Induced Oscillations," *Journal of Sound and Vibration*, Vol. 311, pp 802-823.

[69] Smith, E. Ferri, A. A., and Schmitt, G., 2016, "Optimization of Vibration Isolation Mounts with Internal Rotation in Response to Shock Type Inputs," Proceedings, ASME 2016 IDETC Conference, Charlotte, NC, Aug. 21-24.

[70] Ferri, A. A.1995, "Friction Damping and Isolation Systems," *Journal of Mechanical Design*, Vol. 117, pp. 196-206.

[71] Buckle, I. G. and Mayes, R. L., 1990, "Seismic Isolation History, Application, and Performance – World View," *Earthquake Spectra*, Vol. 6(2), pp. 161-201.

[72] Mokha, A., Constantinou, M. C., Reinhorn, A. M., and Zayas, V., 1991, "Experimental Study of Friction Pendulum Isolation System," *Journal of Structural Engineering*, Vol. 117(4), pp. 1201-1217.

[73] Huang, N. E., Shen, Z., Long, S. R., Wu, M. L., Shih, H. H., Zheng, Q., Yen, N. C., Tung, C. C., and Liu, H. H., 1998, "The Empirical Mode Decomposition and Hilbert Spectrum for Nonlinear and Nonstationary Time Series Analysis," *Proc. Royal Society of London* A, Vol. 454, pp. 903-995.